2020

# Relationship of mitochondrial architecture and bioenergetics: implications in cellular metabolism

BOSTON UNIVERSITY

SCHOOL OF MEDICINE

Dissertation

# RELATIONSHIP OF MITOCHONDRIAL ARCHITECTURE AND BIOENERGETICS: IMPLICATIONS IN CELLULAR METABOLISM

by

**DANE MICHAEL WOLF**

B.S., Boston University, 2013

Submitted in partial fulfillment of the

requirements for the degree of

Doctor of Philosophy

2020

Approved by

First Reader

Orian S. Shirihai, M.D., Ph.D.
Professor of Medicine

Second Reader

Jude T. Deeney, Ph.D.
Assistant Professor of Medicine

Third Reader

Michael T. Kirber, Ph.D.
Associate Professor of Medicine

“In what distant deeps or skies
Burnt the fire of thine eyes?
On what wings dare he aspire?
What the hand, dare seize the fire?”

– William Blake, *The Tyger*

**DEDICATION**

私はこの作品を、私の昇る太陽、真由子に捧げます。

## ACKNOWLEDGMENTS

I want to thank my Ph.D. advisor, Orian Shirihai, for being a dedicated mentor – and for giving me an extraordinary degree of freedom to explore. I want to thank the members of my Ph.D. committee, Valentina Perissi, Jude Deeney, Michael Kirber, and Alexander van der Bliek for generously giving me their time and attention, helping me to examine problems from many different perspectives. I am grateful, as well, to Susan Fried and Lynn Moore, who were not only my program directors, but who also taught a number of my courses, and from whom I learned invaluable lessons. I also want to thank David Shackelford, Mingqi Han, and Chiara Montemurro, as well as Zhenqi Zhou and Nan Hultgren, for many fruitful discussions and ongoing collaborations. I appreciate, as well, the opportunity to have been able to work together with Andreas Reichert, Arun Kondadi, and Ruchika Anand. I am also grateful to have been able to collaborate with Thomas Schwarz and Gulcin Pekkurnaz. Lastly, I want to thank my family, who have supported me in innumerable ways, over the years.

It is important to note that the circumstances in which my doctoral research took place were relatively unique. Shortly after I joined Orian Shirihai's group at Boston University, in 2015, the lab was recruited to the University of California, Los Angeles (UCLA). While I maintained my status as a Ph.D. student at Boston University, most of my research was, in fact, conducted at UCLA. With this being said, I would like to extend my gratitude to Boston University, which permitted me to continue my research into mitochondrial biology, though I was far away from my home campus; and I would

also like to thank UCLA, which accommodated me for many years – not unlike a cell hosting a mitochondrion.

**RELATIONSHIP OF MITOCHONDRIAL ARCHITECTURE AND BIOENERGETICS: IMPLICATIONS IN CELLULAR METABOLISM**

**DANE MICHAEL WOLF**

Boston University School of Medicine, 2020

Major Professor: Orian S. Shirihai, M.D., Ph.D., Professor of Medicine

ABSTRACT

Cells require adenosine triphosphate (ATP) to drive the myriad processes associated with growth, replication, and homeostasis. Eukaryotic cells rely on mitochondria to produce the vast majority of their ATP. Mitochondria consist of a relatively smooth outer mitochondrial membrane (OMM) and a highly complex inner mitochondrial membrane (IMM), containing numerous invaginations, called cristae, which house the molecular machinery of oxidative phosphorylation (OXPHOS). Although mitochondrial form and function are intimately connected, limitations in the resolution of live-cell imaging have hindered the ability to directly visualize the relationship between the architecture of the IMM and its associated bioenergetic properties. Using advanced imaging technologies, including Airyscan, stimulated emission depletion (STED), and structured illumination microscopy (SIM), we developed an approach to image the IMM in living cells. Staining mitochondria with various $\Delta\Psi_m$-dependent dyes, we found that the fluorescence pattern along the IMM was heterogeneous, with cristae possessing a significantly greater fluorescence intensity than the contiguous inner boundary membrane (IBM). Applying the Nernst equation, we determined that the $\Delta\Psi_m$ of cristae is approximately 12 mV stronger than that of IBM,

indicating that the electrochemical gradient that drives ATP synthesis is compartmentalized in cristae membranes. Notably, deletion of key components of the mitochondrial contact site and cristae organizing system (MICOS), as well as OPA1, which regulate crista junctions (CJs), decreased $\Delta\Psi_m$ heterogeneity. Complementing our super-resolution imaging of cristae in living cells, we also developed a machine-learning protocol to quantify IMM architecture. Tracking real-time changes in cristae density, size, and shape, we determined that cristae dynamically remodel on a scale of seconds. Furthermore, we found that cristae move away from sites of mitochondrial fission, and, prior to mitochondrial fusion, the IMM forms finger-like protrusions bridging the membranes of the fusing organelles. Lastly, we investigated the role of the motor adaptor protein, Milton1/TRAK1, in mitochondrial dynamics. Patient-derived Milton1-null fibroblasts not only had impaired mitochondrial motility but exhibited fragmentation corresponding to a roughly 40% decrease in mitochondrial aspect ratio and a 17% increase in circularity, associated with increased DRP1 activity. Conversely, we found that overexpression of Milton1 led to mitochondrial hyperfusion, decreased DRP1 activity, and aberrant clustering of mtDNA. Overall, our studies directly demonstrate that maintaining mitochondrial architecture is essential for preserving the functionality of mitochondria, the hubs of eukaryotic metabolism.

## TABLE OF CONTENTS

## LIST OF FIGURES

## LIST OF ABBREVIATIONS

ADP ..... adenosine diphosphate

AR ..... aspect ratio

ATP ..... adenosine triphosphate

CJ ..... crista junction

CR ..... caloric restriction

DRP1 ..... Dynamin-related Protein 1

EM ..... electron microscopy

ET ..... electron tomography

ETC ..... electron transport chain

$FADH_2$ ..... flavin adenine dinucleotide

FCCP ..... Trifluoromethoxy carbonylcyanide phenylhydrazone

FI ..... fluorescence intensity

IBM ..... inner boundary membrane

IMM ..... inner mitochondrial membrane

IMS ..... intermembrane space

LSM ..... laser-scanning microscope

LUT ..... LookUp Table

MFN1 ..... Mitofusin 1

MFN2 ..... Mitofusin 2

Mic10 ..... Micos10

Mic13 ..... Micos13

Mic60 ..... Micos60

MICOS.....mitochondrial contact site and cristae organizing system

Miro..... Mitochondrial Rho GTPase

mtDNA.....mitochondrial deoxyribonucleic acid

MTG.....MitoTracker Green

NADH.....Nicotinamide adenine dinucleotide

NAO..... 10-*N*-nonyl acridine orange

OMM .....outer mitochondrial membrane

OPA1 ..... Optic Atrophy 1

OXPHOS .....oxidative phosphorylation

PE..... phosphatidylethanolamine

PI.....phosphatidylinositol

PTPMT1.....Protein Tyrosine Phosphatase localized to the Mitochondrion 1

Rho123..... rhodamine 123

ROI..... region of interest

ROS.....reactive oxygen species

SIM ..... structured illumination microscopy

STED.....stimulated emission depletion

TMRE .....tetramethylrhodamine, ethyl ester

TMRM .....tetramethylrhodamine, methyl ester

TRAK1..... Trafficking Kinesin Protein 1

TWS .....Trainable Weka Segmentation

WT ..... wild-type

# CHAPTER ONE

## General Introduction

### Is the mitochondrion more like an electrical cable or an array of batteries?

Life on Earth requires a constant supply of adenosine triphosphate (ATP) to drive the molecular machinery that maintains cellular function. For eukaryotes, mitochondria are the principal providers of ATP. Mitochondria are dynamic organelles originating from a species of α-proteobacteria that began a symbiotic relationship with an archaeal host more than a billion years ago (Imachi *et al*., 2020), propelling the evolution of multicellular organisms.

Mitochondria have two membranes: an outer mitochondrial membrane (OMM), which is relatively smooth and porous, and an inner mitochondrial membrane (IMM), which consists of a highly complex array of invaginations known as cristae (Palade, 1953). Cristae membranes play a key role in the generation of ATP, because they harbor the protein complexes of the electron transport chain (ETC) as well as ATP Synthase. Following the oxidation of intermediates of the citric acid cycle, NADH and $FADH_2$ donate electrons to respiratory complexes I and II, respectively. Moving down the ETC, ultimately being accepted by oxygen, electrons drive conformational changes in complexes I, III, and IV, promoting the pumping of protons from the mitochondrial matrix to the intermembrane space (IMS). The resulting electrochemical gradient, called the proton motive force ($\Delta p$), subsequently drives the rotational movement of ATP synthase, as hydrogen ions ($H^+$) pass through it to reenter the matrix. As ATP Synthase

rotates, it forces together adenosine diphosphate (ADP) and inorganic phosphate ($P_i$), making ATP (Abrahams *et al*., 1994; Melese and Boyer, 1985; Noji *et al*., 1997).

The $\Delta p$ consists of electrical ($\Delta\Psi_m$) and chemical ($\Delta$pH) potential energy (Mitchell, 1961). While these two components of the $\Delta p$ contribute to the synthesis of ATP, the $\Delta\Psi_m$ is the dominant force driving protons back into the matrix (Mitchell P and J, 1969). Although the $\Delta\Psi_m$ is the main driver of ATP production in mitochondria, direct examination of its nature has been challenging, due to limitations in the resolution of live-cell imaging technologies. Following the development of $\Delta\Psi_m$-dependent dyes, such as rhodamine 123 (Rho123) and tetramethylrhodamine, ethyl ester (TMRE), it has been possible to study changes in $\Delta\Psi_m$ as a result of various perturbations, such as treatment with oligomycin and FCCP, which result in hyper- vs. de-polarization, respectively. However, the Abbe diffraction limit (~200 nm) has imposed a significant barrier to studying the relationship between the structures of the IMM and $\Delta\Psi_m$, because the distance between cristae tend to be nearer to 50-100 nm – well below the resolving capacity of conventional confocal microscopes. As a result, conventional confocal micrographs of mitochondria stained with $\Delta\Psi_m$ dyes give the appearance of the dyes being uniformly distributed across the length of the organelle. Analysis of such images led to the conclusion that the $\Delta\Psi_m$ was an iso- or equipotential – *i.e.*, that the difference in charge across the IMM was uniform, analogous to an electrical wire (Amchenkova, 1988).

In his pioneering work characterizing the intricate architecture of the IMM using electron microscopy (EM), Palade noted that "[a]ccording to certain biochemists, for instance, these organelles behave like highly integrated enzymatic systems, in which the composing enzymes are arranged in a 'definite spatial relationship'. However, no trace of this assumed organization is visible in the light microscope, in which, as already mentioned, mitochondria appear as homogeneous, structureless bodies. Naturally this homogeneity does not preclude the existence of a mitochondrial structure with details smaller than the limit of resolution of the light microscope" (Palade, 1953). In spite of this admonition, numerous studies using confocal microscopes with limited spatial resolution nevertheless concluded that the $\Delta\Psi_m$ was homogeneous, representing an equipotential.

In the last two decades, in particular, this idea had become increasingly questionable. EM and biochemical approaches were reporting that the respiratory machinery tends to be localized to the lateral sides of the cristae and that dimers of ATP Synthase are organized in rows along the cristae rims. Furthermore, various studies found that the narrow necks of cristae, called crista junctions (CJs), are regulated by the Mitochondrial Contact Site and Cristae Organizing System (MICOS), as well as OPA1. Given that the proton pumps, as well as the ATP synthesizing turbines, were found to be predominantly concentrated in cristae membranes, and the CJs appeared to represent diffusion barriers to local factors, such as cytochrome c (Frezza *et al*., 2006), it appeared increasingly likely that the charges associated with the $\Delta p$ were likewise subject to some level of

compartmentalization.

Until recently, however, it was unfeasible to test the hypothesis that the electrochemical gradient associated with oxidative phosphorylation (OXPHOS) could be compartmentalized at cristae membranes, because the only available microscopes that could resolve cristae were EMs, which require freezing or fixation of samples, and so preclude the simultaneous visualization of $\Delta\Psi_m$ and IMM architecture. However, with the advent of live-cell, high- and super-resolution imaging technologies, in the last decade or so, it became feasible to directly address the question as to whether the $\Delta\Psi_m$ across the IMM is more like an electrical cable or more closely resembles an array of batteries, where cristae are relatively insulated from each other and exhibit a measure of bioenergetic independence.

Using a combination of Airyscan and stimulated emission depletion (STED), which extend beyond or fully break the Abbe diffraction limit, respectively, we developed an approach to simultaneously image the IMM in living cells and visualize the distribution of $\Delta\Psi_m$-dependent dyes along it (Wolf *et al*., 2019; Wolf *et al*., 2020). The resolution of Airyscan is 1.7x higher than conventional LSM systems, which are limited by their physical pinhole and single detector. Airyscan overcomes this constraint in conventional assembly by using a 32-channel gallium arsenide phosphide photomultiplier tube area detector, in which each of the 32 detector elements functions as an individual pinhole. Possessing exact information about the beam path as well as the position of each detector

element then enables deconvolution techniques to provide improved spatial resolution and signal-to-noise ratio (Huff, 2015). In comparison, STED not only extends beyond the diffraction limit of conventional confocal microscopy but indeed fundamentally breaks it, using a donut-shaped depletion laser beam to quench the emissions of fluorophores at the rim of the focal spot. Following deconvolution, current STED nanoscopy systems can achieve a resolution of 40-50 nm in both the lateral and axial dimensions (Klar *et al*., 2000). Using these novel imaging methods in our study, we observed that there are indeed significant differences in $\Delta\Psi_m$ between cristae membranes and the contiguous membrane running parallel to the long axis of the mitochondrion, called the inner boundary membrane (IBM). Furthermore, we determined that different cristae within the same mitochondrion can possess significantly different membrane potentials from each other. Together, these observations suggested a new paradigm of the $\Delta p$, where, instead of there being a single electrochemical gradient for each mitochondrion, there are multiple electrochemical gradients per organelle, in which individual cristae represent unique bioenergetic entities, capable of maintaining function in spite of depolarization of neighboring cristae along the same IMM (Wolf *et al*., 2019).

**Machine learning as a novel approach for quantifying live-cell images of cristae**

Our development of a novel approach to image cristae in living cells presented us with an unprecedented challenge – the need to accurately and efficiently quantify the hundreds, sometimes thousands, of cristae within a single cell. Our initial attempts to segment cristae using conventional thresholding techniques were hampered by limitations in the

ability to distinguish signal from noise based solely on variations in pixel intensities. A typical reason for this was that, since we had observed differences in the fluorescence intensities (FIs) of cristae stained with $\Delta\Psi_m$-dependent dyes, some cristae would be associated with greater FIs than others, so setting a lower-FI crista below the threshold would tend to result in the merging of higher-FI cristae into single regions of interest (ROIs). To circumvent these segmentation artifacts, we turned to an open-source, machine-learning plugin, available on ImageJ (Schneider *et al*., 2012), called Trainable Weka Segmentation (TWS).

The TWS approach offered substantial benefits for accurately identifying cristae, because it is not limited to segmenting cristae based merely on pixel intensities but employs various algorithms that promote segmentation of objects by analyzing structural details in the image, such as the "Sobel filter" and the "Membrane projection" training feature, which promote edge detection and enhance membranous structures, respectively. Using these filters, we trained the software to not only distinguish cristae from adjoining IBM but also to segment even closely apposed cristae from each other, which was unfeasible with various conventional thresholding techniques (Segawa *et al*., 2020).

Employing this novel, machine-learning approach for segmenting cristae from live-cell Airyscan and structured illumination microscopy (SIM) images, we were able to efficiently quantify basic parameters, such as cristae density as well as aspect ratio (AR) and circularity. Notably, SIM provided a highly effective means for visualizing cristae in

real time, beyond those of Airyscan, by offering a resolution of ~100 nm. This method uses structured excitation light in the form of a grating pattern to excite fluorescent molecules in the sample. Superposition of the two fine patterns – i.e., from the structured excitation light and from the light emitted by the sample – generates moiré fringes. Since the illumination pattern is known, the moiré fringes hold information relating to the unknown patterns in the sample being imaged, capable of revealing high-resolution information that is inaccessible with conventional confocal microscopy (Gustafsson, 2000). In this study, we furthermore used a cardiolipin-deficient cell-culture model, through which we validated that our TWS protocol is effective at differentiating between normal and pathological cristae architecture. Given the burgeoning interest in simultaneously visualizing cristae structure and function, our novel TWS protocol represents a useful approach for accurately measuring the complex structures of the IMM in a relatively unbiased and efficient way.

**Motility protein as novel regulator of mitochondrial membranes**

Around half a century before it was recognized that mitochondria were the so-called "power plants" of the cell, it was known that they readily changed their shapes from being filamentous to punctate and vice versa. Indeed, the most popular name of the organelle, which came into common usage, commemorated this peculiar trait – from Greek, *mitos* means "thread" and *khondrion* "granule." It was not until almost a century after Benda coined the term "mitochondrion", however, that the molecular machines that control their fusion and fission began to come into focus.

Mitofusins 1 and 2 (MFN1/2) (Hales and Fuller, 1997), together with Optic Atrophy 1 (OPA1) (Olichon *et al*., 2003), were found to mediate fusion of the OMM and IMM, respectively; whereas, Dynamin-related Protein 1 (DRP1) was determined to effectuate mitochondrial fission (Smirnova *et al*., 2001). While these four members of the Dynamin Related Protein (DRP) family are the principal mediators of changes in mitochondrial morphology, a growing list of other proteins have been shown to also influence the dynamics of mitochondrial membranes (Giacomello *et al*., 2020).

To the extent that membrane fusion and fission fundamentally entail movement of the organelle, it appeared likely that factors having been largely associated with mitochondrial motility, or trafficking, could also play a role in influencing mitochondrial shape. Milton1/TRAK1, a motor-adaptor protein, critical for transporting neuronal mitochondria from the perinuclear region to axon terminals, appeared to be a viable candidate for influencing mitochondrial architecture, because it played a central role in linking mitochondria to the cytoskeleton by acting as a bridge between Mitochondrial Rho GTPase (Miro) and the motors, Kinesis and Dynein.

Intriguingly, overexpression of Milton1 elongated mitochondria in cell-culture models (Koutsopoulos *et al*., 2010). This suggested that Milton1 could be communicating with the major fusion/fission machinery. While overexpression can provide important clues as to the functions of proteins, it has nevertheless been associated with artifacts, because it can, for example, result in aberrant protein localization or aggregation, which may not

represent the normal attributes of the protein when expressed at endogenous levels.

We, therefore, examined the potential role of Milton1 in patient-derived Milton1-null fibroblasts as well as in INS1 cells, in which we deleted Milton1 via Crispr/Cas9. We observed that the loss of Milton1 expression results in mitochondrial fragmentation in both human fibroblasts as well as INS1 cells; and, notably, reintroduction of Milton1 at endogenous levels rescues the fragmented mitochondrial morphology in Milton1-null fibroblasts. Intriguingly, we found that, in INS1 cells, the activity of DRP1 depended on expression levels of Milton1, where loss of Milton1 resulted in higher DRP1 activity and mitochondrial fragmentation, and overexpression of Milton1 led to less DRP1 activity and mitochondrial hyper-elongation. Together, these data shed light on the role of motility proteins in the basic regulation of mitochondrial membrane architecture.

**Mitochondrial form at the foundations of human health**

Gaining a deeper and deeper understanding of the factors that influence the structure of mitochondrial membranes is of critical importance for human health, because a range of common, as well as rare, diseases and disorders are associated with aberrant mitochondrial architecture, such as, diabetes (Sivitz and Yorek, 2010), liver steatosis (Mamikutty *et al*., 2015), ischaemia-reperfusion injury (Birk *et al*., 2013), and even aging (Daum *et al*., 2013). Mitochondria exposed to various detrimental stressors, such as toxins, excess nutrient (Molina *et al*., 2009), or reactive oxygen species (ROS), tend to depolarize and undergo fragmentation. Such alterations typically result in impaired ATP

production, and therefore tend to create a bioenergetic crisis in the cell. Conversely, mitochondria exposed to different hormetic challenges, such as caloric restriction (CR), tend to elongate (Gomes *et al*., 2011) and increase the density of cristae (Wang C *et al*., 2019) – modifications associated with more efficient respiratory capacity (Cerqueira *et al*., 2016).

Overall, the studies outlined here provide new insights into the pivotal interplay between structure and function in biological systems. In coming years, by further elucidating how changes in mitochondrial membranes affect their basic bioenergetic properties, we will improve our ability to prevent, and even cure, the many pathologies that stem from perturbing our ancient endosymbionts – the mitochondria.

# CHAPTER TWO

## Individual cristae within the same mitochondrion display different membrane potentials and are functionally independent

Dane M. Wolf[1,3,*], Mayuko Segawa[1,*], Arun Kumar Kondadi[7,9], Ruchika Anand[7,9], Sean T. Bailey[2,6], Andreas S. Reichert[7], Alexander M. van der Bliek[4,5], David B. Shackelford[2], Marc Liesa[1,4,8,#], Orian S. Shirihai[1,3,8,#]

1. Department of Medicine, and Department of Molecular and Medical Pharmacology, David Geffen School of Medicine, University of California Los Angeles, CA 90095, USA.

2. Department of Pulmonary and Critical Care Medicine, David Geffen School of Medicine, University of California, Los Angeles, CA 90095, USA; Jonsson Comprehensive Cancer Center, David Geffen School of Medicine, University of California, Los Angeles, CA 90095, USA.

3. Graduate Program in Nutrition and Metabolism, Graduate Medical Sciences, Boston University School of Medicine, Boston, MA 02118, USA.

4. Molecular Biology Institute at UCLA, Los Angeles, CA 90095, USA.

5. Department of Biological Chemistry, David Geffen School of Medicine at UCLA, Los Angeles, CA 90095, USA.

6. University of North Carolina at Chapel Hill, Lineberger Comprehensive Cancer Center, Chapel Hill, NC 27599, USA.

7. Institute of Biochemistry and Molecular Biology I, Medical Faculty, Heinrich Heine University Düsseldorf, 40225, Düsseldorf, Germany.

8. Corresponding authors: Department of Molecular and Medical Pharmacology, David Geffen School of Medicine, University of California, 650 Charles East Young Drive South, 27-200, Los Angeles, California 90095, USA. Tel: +1-617-230-8570; e-mail: mliesa@mednet.ucla.edu; OShirihai@mednet.ucla.edu

* These first authors contributed equally to this study.

[9] These second authors contributed equally to this study.

[#] These corresponding authors contributed equally to this study.

**Running title:** Peaks of membrane potential at cristae

**Keywords:** Cristae, membrane potential, crista junction, MICOS complex, Opa1

## Abstract

The mitochondrial membrane potential ($\Delta\Psi_m$) is the main driver of OXPHOS. The inner mitochondrial membrane (IMM), consisting of cristae and inner boundary membranes (IBM), is considered to carry a uniform $\Delta\Psi_m$. However, sequestration of OXPHOS components in cristae membranes necessitates a re-examination of the equipotential representation of the IMM. We developed an approach to monitor $\Delta\Psi_m$ at the resolution of individual cristae. We found that the IMM was divided into segments with distinct

$\Delta\Psi_m$, corresponding to cristae and IBM. $\Delta\Psi_m$ was greater at cristae compared to IBM. Treatment with oligomycin increased, whereas FCCP decreased, $\Delta\Psi_m$ heterogeneity along the IMM. Impairment of cristae structure through deletion of MICOS-complex components or Opa1 diminished this intramitochondrial heterogeneity of $\Delta\Psi_m$. Lastly, we determined that different cristae within the individual mitochondrion can have disparate membrane potentials and that interventions causing acute depolarization may affect some cristae while sparing others. Altogether, our data support a new model in which cristae within the same mitochondrion behave as independent bioenergetic units, preventing the failure of specific cristae from spreading dysfunction to the rest.

**Introduction**

Mitochondria utilize nutrients and molecular oxygen to generate a membrane potential ($\Delta\Psi_m$) across the inner mitochondrial membrane (IMM). The energy available for ATP synthesis is directly derived from $\Delta\Psi_m$ (Mitchell, 1961; Mitchell and Moyle, 1969); therefore, depolarization directly translates to decreased energy availability for ATP synthesis.

Classical studies suggested that the $\Delta\Psi_m$ was homogeneous along the IMM. Data supporting the equipotential model are 1) mitochondria labeled with $\Delta\Psi_m$-dependent dyes show a homogeneous signal along a single mitochondrion visualized under a low resolution microscope, indicating that the $\Delta\Psi_m$ is likewise homogeneous all along the organelle (Amchenkova, 1988; Skulachev, 2001); and 2) an elongated mitochondrion

stained with a $\Delta\Psi_m$-dependent dye appears to instantaneously lose its $\Delta\Psi_m$ following laser-induced damage to a small ($\leq$0.5 $\mu m^2$) region, suggesting that a mitochondrial filament is analogous to a power cable, where, if one part is compromised, the voltage will simultaneously collapse across its entire length (Amchenkova, 1988; Glancy *et al*., 2015; Skulachev, 2001). These conclusions were drawn after imaging mitochondria with $\Delta\Psi_m$-dependent dyes performed with light microscopes lacking sufficient spatial resolution to visualize the ultrastructure of the IMM. Furthermore, previous studies lacked the temporal resolution to determine whether laser-induced depolarization leads to an instantaneous collapse of $\Delta\Psi_m$ across the whole organelle.

The IMM consists of subcompartments called cristae and inner boundary membrane (IBM) (Palade, 1953). Cristae are invaginations protruding into the mitochondrial matrix, whereas the IBM runs parallel to the outer mitochondrial membrane. Cristae and IBM are connected via narrow tubular or slit-like structures, known as crista junctions (CJs). In recent years, studies show that components of the electron transport chain (ETC) are confined to the lateral surfaces of the cristae rather than equally distributed along the IMM (Vogel *et al*., 2006; Wilkens *et al*., 2013). Moreover, dimers of $F_1F_o$ ATP Synthase assemble in rows along the edges of the cristae (Davies *et al*., 2011; Dudkina *et al*., 2005; Strauss *et al*., 2008). The CJs are thought to be kept in a closed state by oligomers of the inner-membrane dynamin-like GTPase, OPA1 (Frezza *et al*., 2006; Pham *et al*., 2016), in addition to various components of the Mitochondrial Contact Site and Cristae Organizing System (MICOS complex) (Barrera *et al*., 2016; Glytsou *et*

*al*., 2016; John *et al*., 2005; Rabl *et al*., 2009).

These findings provide a conceptual framework, where protons pumped by the ETC across the cristae membrane become concentrated in the cristae lumen rather than the IMS, at large (Busch *et al*., 2013; Pham *et al*., 2016; Rieger *et al*., 2014). Intriguingly, a recent study showed that proton gradients can exist even within the cristae lumen – with a lower pH near complex IV compared to the region around $F_1F_o$ ATP Synthase, which acts as a proton sink (Rieger *et al*., 2014). Furthermore, based on this model, proton pumping through the ETC would increase the local electronegativity on the matrix side of the cristae membrane, attracting protons, in turn, to the lumen side of the cristae membrane. This hypothesis implies that differences in $\Delta\Psi_m$ would exist between the cristae membrane and the IBM.

To establish whether the distribution and structural properties of OXPHOS complexes are functionally significant, it would be critical to directly visualize and quantify the $\Delta\Psi_m$ in relation to the IMM in living cells. If the $\Delta\Psi_m$ is uniform from one end of a mitochondrion to another, the $\Delta\Psi_m$ would be equal at any point along the IMM, supporting the equipotential model. If, however, the $\Delta\Psi_m$ stems from cristae functioning as independent and heterogeneous compartments, the $\Delta\Psi_m$ would vary substantially along the IMM – between cristae and IBM, as well as between different cristae. Testing such hypotheses, nonetheless, has remained virtually unfeasible, because the only way to resolve the IMM has been with the electron microscope, which requires freezing or

fixation of mitochondria and therefore precludes any direct measurement of structure and $\Delta\Psi_m$.

To overcome this limitation, we developed a novel approach for imaging the IMM at high spatiotemporal resolution in living cells, using the LSM880 with Airyscan as well as STED microscopy. Staining active mitochondria with various dyes, we verified that we can resolve cristae from IBM. We then used various $\Delta\Psi_m$-dependent dyes to explore how the intricate architecture of the IMM relates to the most basic mitochondrial function – the $\Delta\Psi_m$ generated by the electrochemical gradient of protons.

**Methods**

**Cell culture.** H1975 (sh-Scramble and sh-PTPMT1) cells were grown in RPMI-1640 (31800-022), supplemented with sodium bicarbonate, Pen/Strep, sodium pyruvate, HEPES, and 10% FBS and cultured in 5% $CO_2$. Patient-derived fibroblasts were grown in DMEM (12100-046), supplemented with sodium bicarbonate, Pen/Strep, sodium pyruvate, HEPES, and 10% FBS and cultured in 5% $CO_2$. L6, MEF, and HeLa cells were cultured in DMEM (12100-046) supplemented with sodium bicarbonate, Pen/Strep, sodium pyruvate, HEPES, and 10% FBS and cultured in 5% $CO_2$. Hap1 cells were cultured in Iscove's Modified Dulbecco's Medium (IMDM) (I3390-500 mL), supplemented with 20% FBS, Pen/Strep, and 2 mM Glutamax. Primary cultures were isolated from unmodified C57BL6/J males and females, 12-28 weeks old, procured from Jackson laboratories and bred in our facility. Mice were provided with water and food ad

libitum, housed 2-5 mice per cage, 12-hr light:dark cycle and at a room temperature of 22–24ºC.

**KD and KO models.** Human H1975 cells expressing shRNA targeting human PTPMT1 were generated using a pLKO.1 vector harboring shRNA (PTPMT1) Clone ID XM_374879.1-547s1c1 (Sigma-Aldrich). Lipofectamine 2000 (ThermoFisher) with PLKO.1 shRNA (PTPMT1) plasmid, lentiviral packaging plasmids pMDLg/pRRE, pRSV-Rev, and enveloping plasmid pMD2.G (Addgene #12251, 12253, 12259) were used to transfect 293T cells to generate lentiviral particles. 48 hrs post transfection, viral media was removed from 293T cells and centrifuged for 5 min at 2,000 rpm. Viral supernatant was then passed through 0.45 μM filter. Target cells were plated at 60% confluency and infected with 1X polybrene and viral supernatant. Viral media was removed and substituted for fresh culture media after 24 hrs, incubated for an additional 24 hrs, followed by puromycin selection. Mic13 KO model was generated through Crispr/Cas9 genome editing (Preprint: Kondadi *et al*., 2019), according to previously-described methods (Anand *et al*., 2016). Mic10 and Mic60 KO cells were made by Horizon (UK) (Preprint: Kondadi *et al*., 2019). Opa1 and Opa1/DRP1 were also generated through Crispr/Cas9 genome editing.

**Live-cell imaging.** Cells were plated in CELLview 4-compartment glass-bottom tissue culture dishes (Greiner Bio-One, 627870), PS, 35/10 mm. Dyes (100 nM 10-*N*-nonyl acridine orange, 15 nM TMRE, 5 μM Rho123, and/or 200 nM MitoTracker Green;

Invitrogen) were added to cell culture media and incubated 1-3 hour prior to live-cell imaging with the alpha Plan-Apochromat 100X/1.46 Oil DIC M27 objective on the Zeiss LSM 880 with Airyscan. Prior to image analysis, raw .czi files were automatically processed into deconvoluted Airyscan images using the Zen software. HeLa cells imaged with STED were stained with 50 nM TMRM (Invitrogen) for 30 min before imaging. Leica SP8 LSM, fitted with STED module, was used to perform live-cell superresolution imaging.

**Image analysis.** Processed Airyscan images were analyzed using ImageJ (Fiji) software (Schneider et al., 2012). Briefly, prior to cell cropping and quantification, background was subtracted from all images using a rolling ball filter = 50. After developing analysis protocols, we designed macros for high-throughput image quantification and analysis. For representative images in figures, we applied the Window/Level function when demonstrating relevant changes in pixel intensities; when specifically comparing cellular structures, we adjusted pixel intensities to optimally demonstrate relevant changes in structure. Images acquired with STED microscopy were deconvolved using Huygens deconvolution software. Note regarding mitochondrial membrane potential and the use of the symbol, $\Delta\Psi_m$: The mitochondrial membrane potential is generally regarded as a negative value, because the matrix side of the IMM is more negatively charged than the IMS side of the IMM. In this study, we examined the heterogeneity in TMRE FI intensity along the IMM and we generally reported these differences as positive. For example, in cases where there was a greater difference in TMRE FI (*i.e.*, $\Delta\Psi_m$) along the

IMM, we reported the changes as positive values to merely express the magnitude of the difference. It is important to note that more polarized regions along the IMM will, in fact, represent more negatively charged microdomains. This trend results from the fact that TMRE is a positively charge dye, and its partitioning to mitochondria is driven by negative charges in the mitochondrial matrix. Increased concentrations of negatively charged ions along the matrix face of the IMM, therefore, will attract a greater amount of TMRE molecules. Previous models of the mitochondrial membrane potential postulated that the electrochemical gradient along the IMM was uniform; therefore, the observed lack of uniformity of the distribution of TMRE prompted us to apply the Nernst equation to different areas of the IMM, where according to classical models there should be no differences. In general, it is also important to note that regions along the IMM that have a stronger TMRE FI represent areas with a greater number of negative charges, corresponding to greater polarization.

**Immunoblotting.** SDS-PAGE assays were conducted by separating 20-30 μg of protein on precast polyacrylamide NuPAGE gels (ThermoFisher) and transferred to nitrocellulose membranes in transfer buffer containing 10% methanol. Proteins were probed with the following primary and secondary antibodies: Opa1 1:1,000 (BD Biosciences, 612606); HSP60 1:10,000 (Abcam, ab46798); Drp1/DLP1 1:1,000 (BD Biosciences, 611112); PTPMT1 1:1,000 (Sigma-Aldrich, HPA043932); β-Actin 1:10,000 (Cell Signaling Technology, BH10D10); TOM20 1:2,000 (Abcam, ab78547); Mic10/C1orf151 1:1,000 (MA5-26031); Mic13/C19orf70 1:1,000 (ProteinTech 25514-1-

AP); Mic60/Mitofilin 1:1,000 (ProteinTech 10179-1-AP); Anti-mouse IgG, HRP-linked Antibody (Cell Signaling Technology, 7076S); Anti-rabbit IgG, HRP-linked Antibody (Cell Signaling Technology, 7074S). Proteins were detected and imaged using SuperSignal West Femto Maximum Sensitivity Substrate (ThermoFisher) and ChemiDoc MP Imaging System (BioRad), respectively. Densitometry was performed using ImageJ (Fiji) (Schneider et al., 2012).

**Statistical Analysis.** All statistical analysis was performed on GraphPad Prism and Microsoft Excel. Data sets were subjected to D'Agostino-Pearson omnibus and/or Shapiro-Wilk normality tests to assess whether data was normally distributed. Data were subjected to 2-tailed Student's *t*-tests, and p values $< 0.5$ were considered statistically significant. Error bars represent SEM, unless otherwise indicated. N = the number of independent experiments. On average, ~20 cells were analyzed per independent experiment per condition. Statistical analysis was performed on the averages from independent experiments.

## Results

### Development of an Airyscan-based approach to resolve cristae and IBM in living cells

Previous studies show that components of OXPHOS are unevenly distributed between the cristae and IBM (Vogel *et al*., 2006; Wilkens *et al*., 2013), suggesting the possibility of $\Delta\Psi_m$ heterogeneity along the IMM within a single mitochondrion. To develop an

approach for the imaging of $\Delta\Psi_m$ associated with cristae and IBM, we first sought to determine whether we could resolve the compartmentalization of the IMM in living cells. To address this question, we incubated various cell types with 10-*N*-nonyl acridine orange (NAO), a fluorescent probe that preferentially binds cardiolipin but also shows some affinity for other phospholipids found in mitochondria, such as phosphatidylethanolamine (PE) and phosphatidylinositol (PI) (Leung *et al*., 2014). Imaging mitochondria from living HeLa, L6, and H1975 cells with the LSM880 equipped with Airyscan technology, we resolved intramitochondrial structures, typically perpendicular to the long axis of the mitochondrion, resembling cristae, as observed in electron micrographs (Fig. 2.1A). Accordingly, the high resolution of the Airyscan-based microscopy allowed separation of cristae structures, IBM, as well as dimmer regions, appearing to be matrix (Fig. 2.1B). To verify that they were matrix, we used matrix-targeted DsRed to label the matrix in H1975 cells and stained their IMM with NAO (Fig. 2.1C). Airyscan imaging confirmed that the dimmer regions of NAO fluorescence within the mitochondria showed the strongest matrix-DsRed signal and vice-versa (arrowheads). To confirm that we correctly identified the cristae structures in cells stained with NAO, we tested whether the pattern of NAO labeling was changed in cells with disrupted cristae structure. As a model, we used HeLa cells with Crispr/Cas9-mediated KO of Mic13 (Fig. EV 2.1A), which destabilizes CJs and disrupts cristae structure (Fig. 2.1D) (Anand *et al*., 2016; Guarani *et al*., 2015). Compared to control HeLa (Fig. 2.1A, B), Mic13-KO mitochondria showed a substantial decrease in the number of perpendicular structures, supporting their identification as cristae. As a second model of cristae

perturbation, we examined H1975 cells with stable KD of PTPMT1 through lentiviral transduction encoding shRNA (Fig. EV 2.1B). PTPMT1 is a mitochondrial phosphatase, essential for biosynthesis of phosphatidylglycerol, a precursor of cardiolipin. Deletion of PTPMT1 has been shown to result in severe derangement of the IMM (Zhang *et al*., 2011). Our Airyscan imaging of sh-Scramble (sh-Scr) control mitochondria shows structures closely resembling normal cristae (Fig. 2.1E), whereas sh-PTPMT1 mitochondria display a variety of deformed structures (Fig. 2.1F) analogous to cristae perturbations that were previously observed in electron micrographs of PTPMT1-deficient models (Zhang *et al*., 2011). Overall, these data demonstrate that Airyscan technology can resolve mitochondrial ultrastructure in living cells. We subsequently used this approach to measure $\Delta\Psi_m$ at the different compartments along the IMM and determine the level of heterogeneity in $\Delta\Psi_m$ within the individual mitochondrion.

**$\Delta\Psi_m$-dependent dyes colocalize most strongly with cristae**

The power-cable model of the $\Delta\Psi_m$ assumes an electrical continuity along the IMM without any electrical resistance (Skulachev, 2001). However, the possibility of heterogeneity in $\Delta\Psi_m$ along the IMM could not be investigated until now. To image $\Delta\Psi_m$ along the IMM, we stained HeLa cells with NAO and TMRE (Farkas *et al*., 1989; Loew *et al*., 1993). Remarkably, TMRE appeared to align with the IMM in a non-homogeneous manner, where the most intense TMRE signal colocalized with NAO at cristae (Fig. 2.2A). To substantiate this observation, we looked at L6 (rat myoblast) cells, which presented the same heterogeneous pattern as HeLa cells (Fig. 2.2B).

When excited by a 488-nm laser, NAO has an emission spectrum that is limited to green wavelengths. However, in these experiments, we needed to excite NAO with the 488-nm laser while simultaneously exciting TMRE with the 561-nm laser, resulting in NAO being exposed to both 488- and 561-nm lasers. The observed alignment of TMRE signal with the membrane staining by NAO raised the possibility that exciting NAO with the 561-nm laser could result in red light emission and thus be wrongly detected as TMRE. To address this possibility, we imaged cells stained with NAO alone and excited simultaneously with 488- ($NAO_{EX}$) and 561-nm ($TMRE_{EX}$) lasers (Fig. 2.2C, top row). We found that emission of NAO after excitation with the 561-nm laser ($TMRE_{EX}$) was undetectable. After adding TMRE to the cells, initially stained with NAO alone, and then exciting with the 561-nm laser using the same power, we observed the appearance of strong signal in the red channel, with most intense pixels colocalizing with NAO at cristae (Fig. 2.2C, bottom row).

To further validate our findings with TMRE and NAO, we used two additional dyes, MitoTracker Green (MTG) and Rhodamine123 (Rho123). MTG covalently binds to various proteins embedded in the cristae membrane and, as such, is considered a $\Delta\Psi_m$-independent dye; although, its initial sequestration in mitochondria depends on $\Delta\Psi_m$ (Presley *et al*., 2003). Rho123 is a $\Delta\Psi_m$ probe, which partitions to mitochondria in a transient way, indicating changes to $\Delta\Psi_m$ (Duchen, 2004; Ward *et al*., 2000). We found that MTG colocalized with TMRE, showing a similar heterogeneous pattern (Fig. EV

2.2A). Then, we examined the partitioning of Rho123 and found that it shows the most intense signal associated with cristae (Fig. EV 2.2B).

To further verify that the staining patterns of TMRE depend on $\Delta\Psi_m$, we used a previously described method to influence $\Delta\Psi_m$: continuous exposure of TMRE-stained mitochondria to the 488-nm laser results in robust and rapid depolarization and repolarization, a phenomenon known as flickering (Duchen *et al*., 1998). We reasoned that the smaller portion of TMRE bound to the membrane in a $\Delta\Psi_m$-independent manner would remain during the flickering event and reveal the level of noise. Moreover, if the differences in TMRE fluorescence intensity (FI) between cristae and IBM depend on $\Delta\Psi_m$, we would expect that the differences between the brightest and dimmest pixels would markedly decrease during depolarization. Conversely, following repolarization, we would expect these differences in pixel intensities to return. Fig. 2.3A shows an example of a mitochondrion from a HeLa cell stained with MTG and TMRE (arrowheads), where we initially observed the heterogeneous patterns of TMRE; however, at ~9 sec, the mitochondrion depolarized, and the heterogeneous staining pattern of TMRE was lost. Notably, at ~16 sec, this mitochondrion repolarized and exhibited nearly the same TMRE heterogeneity as before the depolarization. Quantification of the changes in $\Delta\Psi_m$ during the flickering phenomenon demonstrate that ~85% of TMRE signal was lost during depolarization (Fig. 2.3B). Moreover, the differences between the brightest and dimmest areas (cristae and matrix, respectively) are attenuated during transient depolarization but are reestablished following restoration of

$\Delta\Psi_m$. These data support that the heterogeneous staining patterns of the TMRE are due to differences in $\Delta\Psi_m$.

**Quantification of $\Delta\Psi_m$ differences between cristae and IBM**

The Nernst equation can be used to quantify $\Delta\Psi_m$ by acquiring the FI of $\Delta\Psi_m$-sensitive probes (*e.g.*, TMRE). The FIs of the probes at different subcellular compartments can be used to extrapolate the differences in concentrations of the probe, which are needed to calculate the difference in $\Delta\Psi_m$ between compartments (Ehrenberg *et al*., 1988; Farkas *et al*., 1989; Loew *et al*., 1993; Twig *et al*., 2008; Wikstrom *et al*., 2007). We used the average TMRE FI of the mitochondria as a reference point to calculate the $\Delta\Psi_m$ of the different compartments, an approach similar to that employed in multi-electrode ECG. We found the voltage at cristae to be significantly greater than at IBM (Fig. 2.4A, C). These data indicate that the hetero-potential along the IMM consists of at least 2 basic segments – the cristae and the IBM. Representing pixel intensities in pseudo-color as a LookUp Table (LUT), where white and blue correspond to the strongest and weakest $\Delta\Psi_m$, respectively, it is apparent that the voltage associated with cristae (arrowheads) is generally greater than IBM, emphasizing the electrochemical discontinuity between these contiguous regions of the IMM (Fig. 2.4B).

We next explored whether the $\Delta\Psi_m$ of primary cells would follow the same pattern. We stained mitochondria in primary hepatocytes with TMRE and found $\Delta\Psi_m$ heterogeneity similar to that in HeLa cells, indicating that discrete electrochemical domains also exist

along the IMM of differentiated cells with strong mitochondrial oxidative function (Fig. 2.4D-F).

To further confirm the $\Delta\Psi_m$ differences between cristae and IBM observed using Airyscan imaging, we determined whether the $\Delta\Psi_m$ would display the same heterogeneity by superresolution microscopy (*e.g.*, STED). Using living HeLa cells stained with TMRM, we found a nearly identical pattern in the heterogeneity of $\Delta\Psi_m$, where, notably, cristae $\Delta\Psi_m$ significantly exceeds that of IBM (Fig. 2.4G-I). Altogether, these data demonstrate that the voltage associated with cristae is significantly greater than that of IBM, which is consistent with the higher concentration of ETC components associated with cristae membranes.

**$\Delta\Psi_m$ differences between cristae and IBM ($\Delta\Psi_{Cr\text{-}IBM}$) are sensitive to inhibition of *$F_1F_o$* ATP Synthase and to uncoupling.**

*$F_1F_o$* ATP Synthase is primarily localized to the rims of cristae (Davies *et al*., 2011; Dudkina *et al*., 2005; Strauss *et al*., 2008). If cristae maintain $\Delta\Psi_m$ that is distinct from the IBM, then inhibiting the consumption of the proton gradient by *$F_1F_o$* ATP Synthase would further increase the difference between IBM and cristae. To assess this hypothesis, we inhibited *$F_1F_o$* ATP Synthase with oligomycin and measured the difference in the $\Delta\Psi_m$ between the cristae and IBM ($\Delta\Psi_{Cr\text{-}IBM}$). We found that, not only did oligomycin increase the total $\Delta\Psi_m$ (Fig. 2.5A, C), as expected (Farkas *et al*., 1989), but it also increased the $\Delta\Psi_{Cr\text{-}IBM}$, hyperpolarizing the cristae (Fig. 2.5B, C). Conversely,

we tested whether treatment with FCCP, a protonophore that shuttles protons across the IMM, would diminish the $\Delta\Psi_{Cr\text{-}IBM}$. Consistent with previous studies (Farkas *et al*., 1989; Loew *et al*., 1993), we determined that FCCP decreased the total $\Delta\Psi_m$ (Fig. 2.5A, C) and resulted in mitochondrial fragmentation (Duvezin-Caubet *et al*., 2006; Griparic *et al*., 2007; Ishihara *et al*., 2006) (Fig. EV 2.3A, B). Furthermore, we observed that treatment with FCCP decreased the $\Delta\Psi_{Cr\text{-}IBM}$ (Fig. 2.5B-D).

**The crista-junction (CJ) modulators, MICOS complex and Opa1, regulate $\Delta\Psi_{Cr\text{-}IBM}$**

To determine the role of CJs and cristae architecture in the generation of $\Delta\Psi_{Cr\text{-}IBM}$, we used cellular models in which proteins controlling the formation of cristae and CJs are perturbed. To date, the most notable of these are the family of MICOS-complex proteins (Barbot *et al*., 2015; Barrera *et al*., 2016; Friedman *et al*., 2015; Guarani *et al*., 2015; Harner *et al*., 2011; Hessenberger *et al*., 2017; Hoppins *et al*., 2011; Rabl *et al*., 2009; Rampelt *et al*., 2017; von der Malsburg *et al*., 2011; Wollweber *et al*., 2017; Zerbes *et al*., 2012) and the GTPase, Opa1 (Cogliati *et al*., 2016; Frezza *et al*., 2006). To determine whether the MICOS complex and/or Opa1 are required to preserve the $\Delta\Psi_{Cr\text{-}IBM}$, we examined $\Delta\Psi_{Cr\text{-}IBM}$ in cells with either Opa1 or MICOS-complex subunits deleted.

Firstly, we examined the effect of deleting Mic13 on $\Delta\Psi_{Cr\text{-}IBM}$ in HeLa cells. While Mic13-KO cells showed a marked decrease in the number of cristae, we identified some regions of IMM that maintained cristae structures (Fig. 2.6A; arrowheads). Mic13-KO mitochondria showed decreased heterogeneity of TMRE staining along the IMM and

$\Delta\Psi_{Cr\text{-}IBM}$ was significantly diminished, compared to control HeLa cells (Fig. 2.6A, B). To further address the role of the MICOS complex in regulating the mitochondrial hetero-potential, we examined cells in which Mic60 or Mic10 were deleted (Fig. EV 2.1C). In these cells, we observed a significant diminishment of heterogeneity of TMRE FI along the IMM (Fig. 2.6C), as well as a drop in $\Delta\Psi_{Cr\text{-}IBM}$ (Fig. 2.6D, E).

We next studied the effects of Opa1 deletion on $\Delta\Psi_{Cr\text{-}IBM}$. Various studies have demonstrated that not only does Opa1 associate with components of the MICOS complex (Barrera *et al*., 2016; Glytsou *et al*., 2016), but it appears to have an independent function as a molecular staple, holding the cristae in a closed configuration (Frezza *et al*., 2006). We hypothesized, therefore, that deletion of Opa1 (Fig. EV 2.1D), like deletion of components of the MICOS complex, would disrupt the electrochemical boundaries between the cristae and the IBM, thereby equilibrating the potential along the IMM. Our data indicate that deletion of Opa1 indeed results in a significant loss in $\Delta\Psi_{Cr\text{-}IBM}$ (Fig. 2.7A, B). Altogether, these data indicate that cristae architecture and CJs are essential for the formation of the electrochemical boundaries that allow for $\Delta\Psi_m$ of cristae to remain different from that of IBM.

**The largest differences in $\Delta\Psi_{Cr\text{-}IBM}$ arise in cristae vesicles, generated by deleting CJ regulators.**

Intriguingly, in ~25% of Mic10 KO cells, we observed structures that appeared to have detached from the IBM and become hyperpolarized (Fig. 2.6C, lowest row, arrow). To

test whether these hyperpolarized structures in Mic10 KO cells had no membrane continuity with the IMM, we performed laser-induced depolarization of mitochondria that included such vesicles. If these hyperpolarized vesicles were unanchored from the IMM, we would expect that they would remain polarized despite the collapse of $\Delta\Psi_m$ elsewhere in the mitochondrion. Fig. 2.8A shows that such a hyperpolarized structure (arrowhead) maintained its $\Delta\Psi_{vesicle}$ for at least 15 sec after the rest of the mitochondrion had depolarized. We determined that the $\Delta\Psi_{vesicle\text{-}IBM}$ of such vesicles was significantly greater than cristae that maintained attachment to the IBM ($\Delta\Psi_{Cr\text{-}IBM}$ for Control cristae = 10.11 mV vs. $\Delta\Psi_{vesicle\text{-}IBM}$ for Mic10 KO vesicles = 25.85 mV; $p = 0.0005$; $N = 3$ independent experiments).

We further hypothesized that deletion of both Opa1 and Drp1 (Fig. EV 2.1D) would result in an extreme case of electrochemical discontinuity of the IMM. Indeed, our imaging of Opa1&Drp1 DKO MEFs demonstrates the formation of strongly hyperpolarized vesicles moving haphazardly within the matrix (Fig. 2.8B; Movie EV 1 shows time series of hyperpolarized vesicles). Compared to control MEFs that had a $\Delta\Psi_{Cr\text{-}IBM}$ of 10.67 mV, the hyperpolarized vesicles in the Opa1&Drp1 DKO MEFs showed a $\Delta\Psi_{vesicle\text{-}IBM}$ of 39.55 mV ($p = 0.0014$; $N = 3$ independent experiments).

Hyperpolarized vesicles were quite rare in control cells, suggesting that they are formed in response to bioenergetic dysfunction and/or impaired cristae formation.

**Different cristae within a mitochondrion can have different $\Delta\Psi_m$, indicating that cristae function as independent bioenergetic units**

Previous studies suggest that a single mitochondrion constitutes a single bioenergetic unit (Amchenkova, 1988; Glancy *et al*., 2015; Skulachev, 2001). A typical experiment would involve laser-induced depolarization at one tip of a mitochondrion, which would appear to instantaneously result in a complete collapse of the $\Delta\Psi_m$, leading to the conclusion that the entire organelle functions as one electrochemical unit. These time-lapse experiments determined $\Delta\Psi_m$ at intervals of 5 sec or longer after laser-induced depolarization and were employing microscopes that allowed for single-mitochondrion, rather single-crista, resolution (Amchenkova, 1988; Skulachev, 2001). A 5-sec interval, however, is enough time to generate and propagate a soluble signaling molecule and/or changes in membrane architecture that could induce depolarization of independent cristae structures in an entire mitochondrion. Thus, to test whether laser-induced depolarization reflected 1) an instantaneous collapse in voltage due to the mitochondrion functioning as an uninterrupted electrochemical conduit; or 2) a gradual loss of voltage due to a chemical signal and/or structural changes propagating through the organelle, we re-ran the same experiments as previously described but acquired images ~20X more rapidly. Visualizing mitochondria from rat myoblasts (L6) using Rho123 (Fig. 2.9A; Movie EV 2 shows time series), we exposed a small mitochondrial region (~0.5-1 $\mu m^2$) to a rapid, high-power pulse of the 2-photon (2-P) laser (arrow, white box). We then observed mitochondria depolarizing in a wavelike (*i.e.*, gradual) manner: the $\Delta\Psi_m$-dependent dye dispersed more rapidly near the original site of laser stress, prior to dispersing along areas

farther away (arrowheads follow the loss of $\Delta\Psi_m$ over time). The Rho123 signal is displayed as a multicolored LUT, where pixel intensity is color-coded on a scale where the most-intense pixels appear white (highest $\Delta\Psi_m$) and the least-intense pixels appear blue (lowest $\Delta\Psi_m$). Examining the images immediately following laser-induced depolarization (~0.30 sec, ~0.45 sec, and ~0.60 sec), we found that the mitochondrion loses $\Delta\Psi_m$ first in proximity to the site of laser stress, because the pixels become more green and blue, whereas the distal site remains polarized, as indicated by the white and red pixels. In Fig. 2.9B, we plotted the pixel intensity of the mitochondrion in 9A as a function of distance from the top to the bottom at different time points. In the image immediately preceding laser-induced depolarization (red line), the peaks and valleys occupy a similar range of intensities from one end of the mitochondrion to the other. Following depolarization induced by the 2-P laser pulse, Rho123 intensity proximal to the site of laser stress drops substantially, while the signal intensity at the distal end remains almost unchanged (green line). These asymmetrical changes in FI are visible at later time points (blue and purple lines), until ~2.1 sec, when the mitochondrion has lost virtually all of its $\Delta\Psi_m$ (dark purple line).

In previous studies, laser-induced depolarization experiments were often performed on mitochondria in fibroblasts, which tend to be remarkably elongated. Therefore, fibroblasts represent an optimal system to test the model of the mitochondrion as an "electrical wire" or "power cable", where loss of $\Delta\Psi_m$ in one place would lead to simultaneous depolarization across the whole organelle (Amchenkova, 1988; Skulachev,

2001). Staining mitochondria in human fibroblasts with MTG and TMRE, we performed laser-induced depolarization experiments (Fig. 2.9C). Loading of MTG depends on $\Delta\Psi_m$, but it is retained in mitochondria even after depolarization, because, once inside the organelle, it binds covalently to thiol moieties of various proteins (Presley *et al*., 2003). Partitioning of TMRE to mitochondria, on the other hand, depends entirely on $\Delta\Psi_m$. Following 2-P-laser pulsation (arrow, white box), there is greater and greater loss of TMRE over time, while the signal from MTG remains. Fig. 2.9D, which shows the TMRE channel alone, demonstrates that, even though the mitochondrion begins to depolarize proximal to the site of the initial laser stress, it maintains its $\Delta\Psi_m$, distally, for a period of time. To quantify this asymmetry in $\Delta\Psi_m$, we measured TMRE FI immediately after 2-P laser pulsation at sites distal to the initial perturbation ($\geq$10 μm from white box) vs. proximal ($\leq$1 μm from white box) (Fig. 2.9E).

Quantification shows that in the seconds following laser-induced depolarization, mitochondria tend to remain significantly more polarized at sites distant from targeted laser stress, compared to sites close to it. The time gap of seconds for the propagation of the depolarization wave does not support the notion that the IMM functions as a single electrochemical conduit. We next determined the frequency that mitochondria appeared to depolarize in a wavelike vs. instantaneous manner. Time-lapse imaging at approximately 300 msec/frame, we were significantly more likely to observe wavelike instead of instantaneous depolarization (Fig. 2.9F).

Together, using different cell lines and mitochondrial dyes, our data suggest that the $\Delta\Psi_m$ is organized into multiple, disparate electrochemical domains along the length of the IMM. It further suggests that the laser-induced depolarization phenomenon propagates within the mitochondrion through the diffusion of a signal and/or structural changes rather than by the membrane acting as a continuous electrochemical element.

If cristae possess a measure of functional autonomy, then it is possible that different cristae within a single mitochondrion could maintain significantly different membrane potentials ($\Delta\Psi_{Cr}$) from each other. To determine whether one crista within a single mitochondrion has greater $\Delta\Psi_{Cr}$ compared to a neighboring crista, we first defined the level of stability of $\Delta\Psi_{Cr}$ of individual cristae and then asked if the difference between two cristae is larger than the $\Delta\Psi_{Cr}$ fluctuation observed over time in a single crista. To explore this possibility, we performed time-lapse imaging of mitochondria stained with MTG and TMRE, and we examined the stability of $\Delta\Psi_{Cr}$ generated by different cristae over time. The membrane potential of each crista was calculated by referencing it to the IBM to produce a value of $\Delta\Psi_{Cr\text{-}IBM}$. Fig. 2.10A shows an example of 4 different cristae – "A-D" (arrowheads) – that we followed for a period of ~10 sec. Fig. 2.10B shows that the average $\Delta\Psi_{Cr\text{-}IBM}$ over time of Cristae C and D is more than double that of Cristae A and B, indicating that cristae maintain different membrane potentials. To further examine their relative functional stability over time, we quantified the standard deviation of $\Delta\Psi_{Cr\text{-}IBM}$ within each crista over time and compared it to the standard deviation of $\Delta\Psi_{Cr\text{-}IBM}$ between cristae over time. Our data indicate that, over a period of ~10 sec, there are

significantly larger differences between cristae within a single mitochondrion than the variability recorded from any individual crista over time (Fig. 2.10C). To further investigate the extent to which cristae could exhibit functional autonomy, we studied time-lapse images of mitochondria stained with MTG and TMRE and discovered instances where mitochondria would undergo partial depolarization (Fig. 2.10D-F; arrowhead, arrows; Movies EV 3, 4, and 5 show time series of partial depolarization from E, F). Remarkably, instances of partial depolarization of a single mitochondrion revealed cristae that remained polarized despite the depolarization of adjacent cristae. Analyzing the specific frames showing partial depolarization, we quantified the $\Delta\Psi_{Cr\text{-}IBM}$ of the polarized cristae vs. depolarized cristae and determined that the polarized cristae maintained a greater $\Delta\Psi_{Cr\text{-}IBM}$ than neighboring cristae that appeared to have depolarized (Fig. 2.10G). Altogether, our data demonstrate that cristae display a degree of functional autonomy, highlighting a new role of these critical structures as independent bioenergetic units.

**Discussion**

$\Delta\Psi_m$ is the main driving force for proton re-entry through $F_1F_o$ ATP Synthase into the mitochondrial matrix (Mitchell, 1961; Mitchell and Moyle, 1969). In this study, we provide evidence, for the first time, that cristae maintain greater $\Delta\Psi_m$ than IBM and that each individual crista within the same mitochondrion can maintain $\Delta\Psi_m$ distinct from neighboring cristae. Using the LSM880 with Airyscan and STED microscopy, we directly visualized the relationship of the $\Delta\Psi_m$ to the IMM, in respiring mitochondria.

Our observation that cristae and IBM have heterogeneous $\Delta\Psi_m$ is based on differential partitioning of $\Delta\Psi_m$-dependent probes to the different segments of the IMM. We provide several lines of evidence to support that this differential partitioning of the $\Delta\Psi_m$-dependent probes is reflecting $\Delta\Psi_m$ and not an artifact of dye binding to the cristae: 1) We repeated the observation with the unique $\Delta\Psi_m$-dependent probes, TMRE, TMRM, and Rho123 (Duchen, 2004; Farkas *et al*., 1989; Loew *et al*., 1993). If partitioning to cristae were based on non-Nerstian binding, it is unlikely to occur with different dyes. 2) $\Delta\Psi_{Cr\text{-}IBM}$ increased in response to oligomycin and decreased in response to FCCP. 3) Partitioning to the cristae was decreased in models lacking MICOS-complex subunits or Opa1. 4) Analyzing flickering events, heterogeneity of TMRE FI along the mitochondrion was markedly decreased during instances of depolarization and reestablished following restoration of $\Delta\Psi_m$. This confirms that TMRE signal stemming from $\Delta\Psi_m$-independent binding of TMRE to the cristae in our experimental system was negligible. 5) The data relating to $\Delta\Psi_{Cr\text{-}IBM}$ obtained by Airyscan technology was confirmed by STED microscopy. The imaging was performed in different laboratories with different batches of HeLa cells. 6) We provided data to confirm the same observations in MEFs, HeLa cells, Hap1 cells, L6 myoblasts, H1975 cells, primary mouse hepatocytes, and human fibroblasts. Altogether, this evidence strongly supports the conclusion that cristae and IBM are sufficiently separated, thus being electrochemically insulated from each other, to allow for different membrane potentials to co-exist along the IMM. A limitation of this methodology is the lack of dyes that are completely independent of $\Delta\Psi_m$ or cardiolipin content. As a result, the NAO and MTG

staining of IBM appeared weaker than that of cristae, precluding ratiometric imaging. This limitation only pertains to the differences in $\Delta\Psi_m$ of cristae vs. IBM but would not affect conclusions related to the $\Delta\Psi_m$ differences between different cristae within the same mitochondrion. Moreover, the 6 points listed above support that the TMRE FI differences we observed between cristae and IBM indeed reflect $\Delta\Psi_m$ differences.

After confirming that the heterogeneous partitioning of $\Delta\Psi_m$-dependent probes was in fact due to differences in $\Delta\Psi_m$, we examined the possibility that different cristae within the same mitochondrion could function as unique electrochemical domains and thus as independent bioenergetic units. We observed that, when imaging at high temporal resolution, laser-induced depolarization of elongated mitochondria did not tend to result in a simultaneous collapse of $\Delta\Psi_m$ across the entire organelle but rather in a rapid, wavelike depolarization. This discrepancy from earlier studies can be attributed to the fact that previous assays involving laser-induced damage did not image the mitochondria rapidly enough after perturbing a small region of the organelle – *e.g.*, acquisition of a single frame expended 5 to 10 sec (Amchenkova, 1988; Skulachev, 2001). Critical delays, either in the time it takes to acquire a single frame of a time series (Amchenkova, 1988) or in the duration of the perturbation itself (Glancy *et al*., 2015), will increase the likelihood of missing possible spatial differences in depolarization (originating close to the site of laser-induced damage). Our study suggests that, unless imaging at $\geq 1$ frame(s) per sec, observing partial depolarization events is improbable. The tendency for one mitochondrion to exhibit localized depolarization indicates that a single organelle

does not resemble an electrical wire (Fig. 2.11A, B) but rather appears to function more like a configuration of interconnected batteries (Fig. 2.11C, D).

Our high- or super-resolution imaging of the IMM stained with $\Delta\Psi_m$-dependent dyes is consistent with a model of cristae as individual, interconnected batteries. The $\Delta\Psi_m$ is not homogeneous along the IMM but shows significant differences between the cristae and IBM, demonstrating electrochemical discontinuity between the otherwise physically connected membranes. Following deletions of various proteins involved in regulating cristae architecture, including CJ formation, we observed a decrease in the difference between the $\Delta\Psi_m$ at the cristae membranes relative to the IBM. These data suggest that opening of CJs tends to equalize the $\Delta\Psi_m$ between cristae and IBM by a mechanism that requires further study. The generation of hyperpolarized vesicles, following different genetic perturbations that eliminate CJs, reinforces our general observation that increasing compartmentalization of the IMM, in turn, intensifies the electrochemical gradient. Lastly, our time-lapse imaging experiments show that the $\Delta\Psi_{Cr\text{-}IBM}$ of an individual crista is less variable over time compared to the $\Delta\Psi_{Cr\text{-}IBM}$ amongst different cristae within the same mitochondrion. Furthermore, we observe that, during transient depolarization, some cristae can maintain polarity despite the collapse in $\Delta\Psi_m$ of adjacent cristae. In summary, our data support a new paradigm where each crista maintains its own $\Delta\Psi_m$ that is different from both the IBM and from neighboring cristae.

This study raises interesting questions as to why mitochondria organize the $\Delta\Psi_m$ in this

way. One advantage, for example, could be related to the fact that $\Delta\Psi_m$ constitutes the main energy available to drive protons through $F_1F_o$ ATP Synthase to produce ATP. As such, the localization of $F_1F_o$ ATP Synthase at the cristae rims appears to be advantageous in terms of proximity to the batteries. Another possible advantage could be: compartmentalization of $\Delta\Psi_m$ in each crista may serve as a safeguard mechanism restricting the impact of localized damage. In the case of the equipotential model, where the inner membrane of the entire mitochondrion represents a single capacitor, a breach in membrane integrity in one crista would cause a collapse in voltage in all cristae and compromise the function of the whole organelle. If, on the other hand, the IMM could maintain numerous, discrete electrochemical gradients, like a group of batteries, then failure of one or more would not invariably jeopardize the entire mitochondrion. This may be of particular relevance in cells harboring a highly interconnected mitochondrial network as opposed to cells with less elongated and/or branched mitochondria. Furthermore, the hetero-potential model suggests that cristae with greater $\Delta\Psi_{Cr\text{-}IBM}$ could compensate for cristae with impaired function.

Hyperpolarized and depolarized IMM potentials are associated with different states of respiration. While both uncoupling and an increased rate of ATP synthesis dissipate $\Delta\Psi_m$, a decrease in ATP synthesis may result in hyperpolarization and increased ROS production. The hetero-potential model of the mitochondrion allows for different cristae to serve different functions. In this model, some cristae could be more dedicated to ATP synthesis, whereas neighboring cristae could play a role in ROS signaling. The hetero-

potential model further allows for the consideration that different cristae may engage in primarily complex II vs. complex I respiration, which are associated with different membrane potentials and could be driven by different fuels.

In conclusion, our study identifies a new parameter of mitochondrial function: a mitochondrial hetero-potential arising from the compartmentalization of the $\Delta\Psi_m$ along the IMM. These findings have wide-ranging implications for human health, because many diseases and medical complications – *e.g.*, dominant optic atrophy (Amati-Bonneau *et al*., 2008; Zanna *et al*., 2008), ischemia reperfusion injury (Birk *et al*., 2013), and even aging (Daum *et al*., 2013) – are associated with severe perturbations in cristae structure. Pathogenic changes to cristae architecture may undermine the autonomy of cristae bioenergetics, leading to the conversion of the IMM into an equipotential membrane. Consequently, damage inflicted to any isolated region may impact the bioenergetics of the entire mitochondrion, rendering the cell more vulnerable to mitochondrial toxicants and metabolic stress. Restoring the architecture of the IMM, therefore, could represent a viable approach to reestablishing the disparate electrochemical gradients that are the basis for normal mitochondrial function. This study emphasizes the need to directly explore the relationship between cristae structure and function to further elucidate the etiology of such diseases and, in turn, foster more effective therapies for treating them.

**Acknowledgements**

We would like to thank the referees and editor, who gave us outstanding advice and helped us build the concepts presented in this work. We thank Drs. Barbara Corkey, Martin Picard, Gilad Twig, Gulcin Pekkurnaz, Ophry Pines, Victor Darley-Usmar, Fernando Abdulkader, György Hajnóczky, and Daniel Dagan for insightful feedback. We thank Samuel Itskanov for generating the Opa1 and Opa1&Drp1 DKO MEF cell lines and Dr. Yair Anikster for providing human fibroblasts. We also thank Drs. Mingqi Han and Alejandro Martorell Riera for help with reagents and cell lines. We thank the Centre for Advanced Imaging (CAi) at HHU, Düsseldorf, for providing facilities for STED imaging. ASR was supported by the Deutsche Forschungsgemeinschaft (DFG) grant RE 1575/2-1 and SFB 974 Project B09; AKK and RA/ASR were supported by the Medical faculty, Heinrich Heine University Düsseldorf FoKo-37/2015 and Foko-02/2015, respectively. OSS is funded by NIH-NIDDK 5-RO1DK099618-02. ML and MS are funded by UCLA Department of Medicine Chair commitment and UCSD/UCLA Diabetes Research Center grant, NIH P30 DK063491. DBS is funded by an NIH/NCI R01 CA208642-01. STB was supported by an NIH T32 training grant HL072752.

**Author contributions**

MS and DMW conceived the study, designed and executed the experiments, analyzed the data, produced the figures, and wrote the manuscript. OSS contributed to study design and helped write the manuscript. STB generated the sh-Scramble and sh-PTPMT1 cell lines. AKK performed the STED imaging. RA created the Mic13 KO cell line. ASR,

AMvdB, DBS provided valuable recommendations, contributing to the study design and reagents. ML and OSS provided resources and supervised the study.

**Conflict of interest**

The authors declare that they have no conflicts of interest.

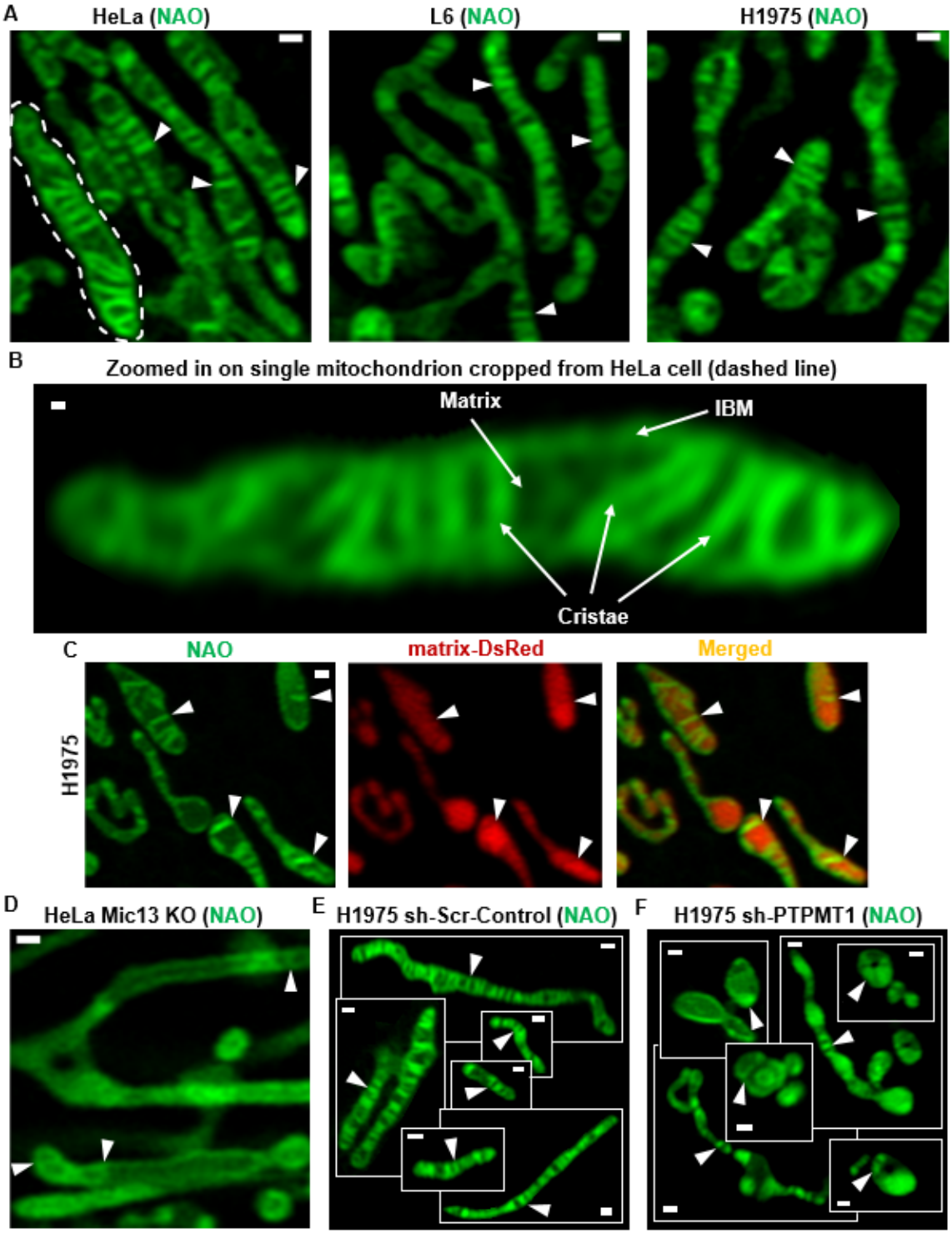


**Figure 2.1. High-resolution fluorescence imaging using Airyscan resolves the inner mitochondrial membrane (IMM) structure in live cells.**

A-F. High-resolution imaging of mitochondria in live cells using the Airyscan module of Zeiss LSM880 confocal microscope.

A. Images of IMM in living HeLa, L6, and H1975 cells, stained with 10-*N*-nonyl acridine orange (NAO). NAO preferentially binds phospholipids in the IMM, such as cardiolipin. Arrowheads indicate cristae in the IMM. Scale bar = 500 nm. $N \geq 3$ independent experiments for each cell type.

B. Mitochondrion cropped from HeLa cell shown in A (dashed line) and zoomed in to show cristae, inner boundary membrane (IBM), and matrix (arrows). Scale bar = 100 nm.

C. H1975 cells transduced with matrix-targeted-DsRed and stained with NAO. Matrix-targeted Ds-Red differentiates matrix from cristae stained with NAO. Arrowheads point to cristae. Scale bar = 500 nm. N = 1 independent experiment.

D. The structure of the IMM in Mic13-KO cells (HeLa), stained with NAO. The number of cristae is decreased in Mic13-KO compared to control cells shown in panel A, labeled with arrowheads. Scale bar = 500 nm. N = 3 independent experiments.

E-F. Live-cell imaging of the IMM in control and PTPMT1 KD H1975 cells, a model of cardiolipin deficiency.

E. A gallery of mitochondria from various control H1975 cells expressing scrambled shRNA and stained with NAO, showing cristae (arrowheads). Scale bars = 500 nm. N = 3 independent experiments.

F. A gallery of mitochondria from various H1975 cells expressing PTPMT1 shRNA and stained with NAO. Note the derangement of the ultrastructure (arrowheads). Scale bars = 500 nm. N = 3 independent experiments.

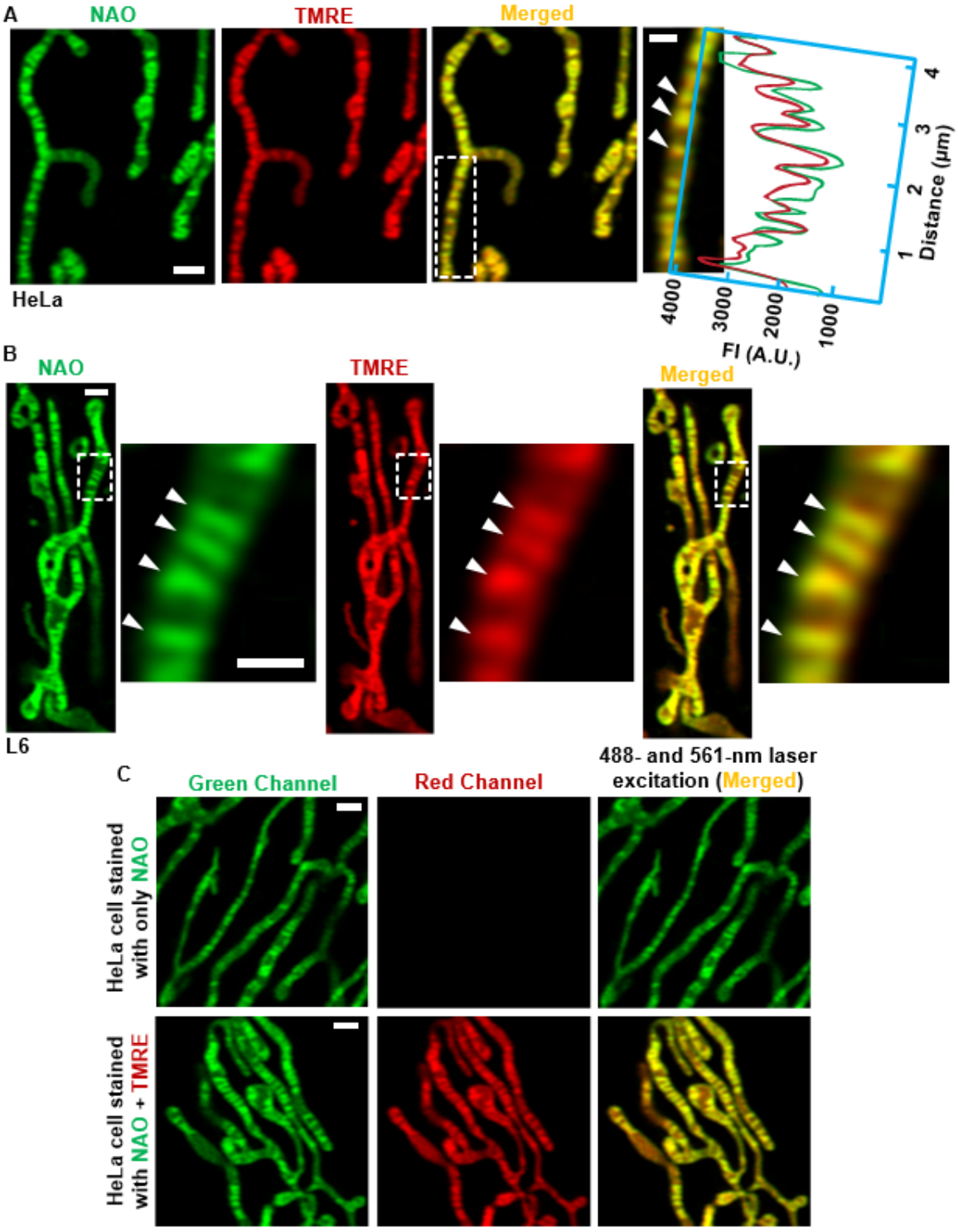


**Figure 2.2. The $\Delta\Psi_m$-potential-sensitive dye, TMRE, partitions to cristae stained with NAO.**

A-C. High-resolution imaging of mitochondria in live cells using the Airyscan module of Zeiss LSM880 confocal microscope.

A. Mitochondria from HeLa cell, co-stained with NAO and TMRE. Area from dashed white box, zoomed to right, shows the red and green intensities of TMRE and NAO colocalized. Scale bars = 500 nm. N = 3 independent experiments.

B. Mitochondria in L6 myoblast, co-stained with NAO and TMRE. Area from dashed white box, zoomed to right, shows colocalizing NAO and TMRE at the cristae membrane (arrowheads). Scale bars = 500 nm. N = 3 independent experiments.

C. Mitochondria in HeLa cells, stained with NAO alone (top row) vs. NAO + TMRE (bottom row), and simultaneously excited with 488- and 561-nm lasers. Note that mitochondria stained with NAO alone do not emit noticeable fluorescence in the red channel; only after adding TMRE does strong signal appear in the red channel, showing negligible bleed-through. Scale bars = 500 nm. N = 2 independent experiments.

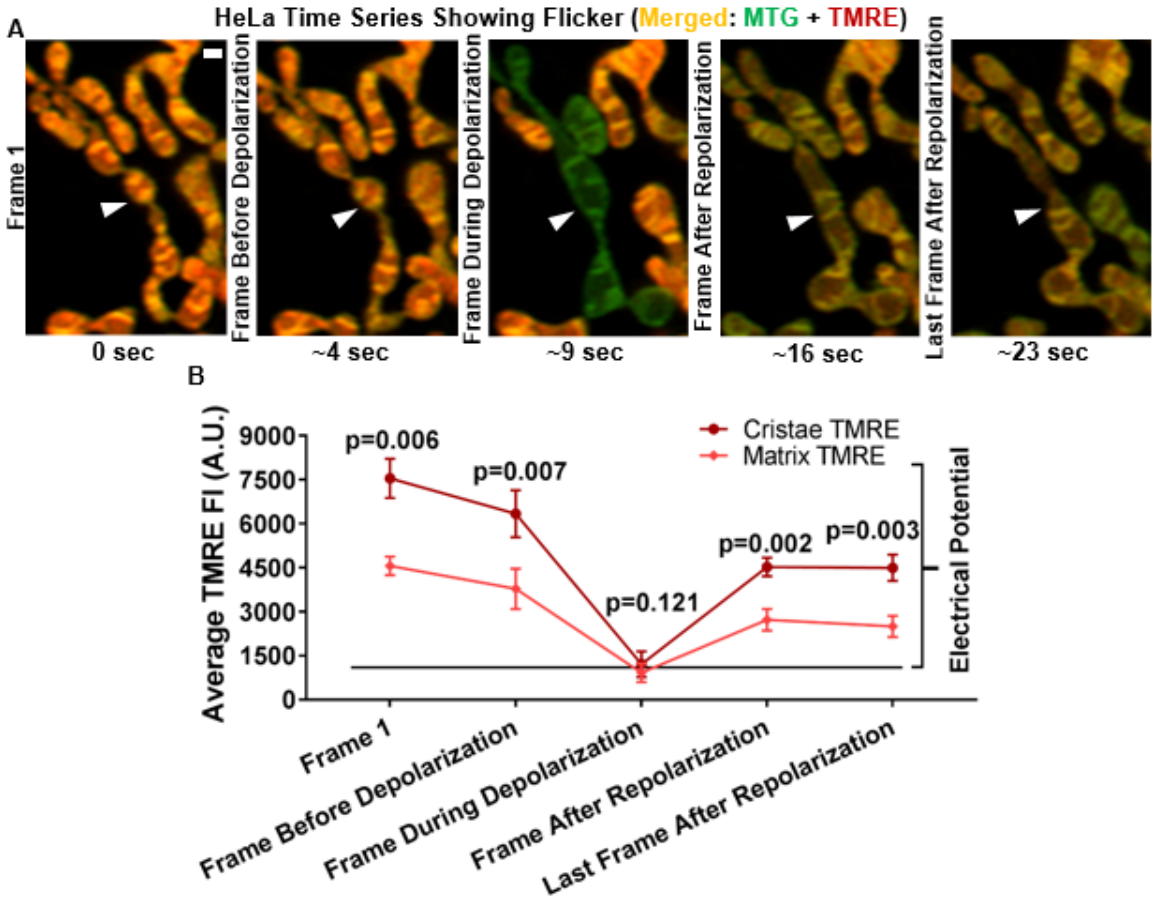


**Figure 2.3. Validation that TMRE partitioning to cristae is $\Delta\Psi_m$-dependent.**

A. Time-lapse Airyscan imaging of $\Delta\Psi_m$ in living HeLa cell, co-stained with MTG ($\Delta\Psi_m$-insensitive after loading) and TMRE ($\Delta\Psi_m$ sensitive). Arrowhead points to a flickering event where a mitochondrion depolarizes (~9 sec) and repolarizes (~16 sec), showing that heterogeneous signal from TMRE (but not MTG) disappears and reappears. Scale bar = 500 nm. N = 4 independent experiments.

B. Quantification of A. Plot shows average TMRE fluorescence intensity (FI) of cristae (dark red line) vs. matrix (light red line) during the time series. The drop in TMRE FI during the depolarization phase of the flickering is the $\Delta\Psi_m$-sensitive component of the

TMRE signal. The remaining TMRE FI during depolarization can be considered as the $\Delta\Psi_m$-insensitive portion of TMRE signal. Note that the remaining TMRE FI after depolarization at the cristae and matrix are approximately identical, indicating that differences in TMRE FI between the cristae and matrix prior to depolarization are derived from differences in $\Delta\Psi_m$. N = 4 independent experiments.

Data information: Data sets were subjected to D'Agostino-Pearson omnibus and/or Shapiro-Wilk normality tests to assess whether data was normally distributed. Data were analyzed with 2-tailed Student's *t*-tests, and p values < 0.5 were considered statistically significant. Specific p values are indicated in the figure. Error bars indicate SEM.

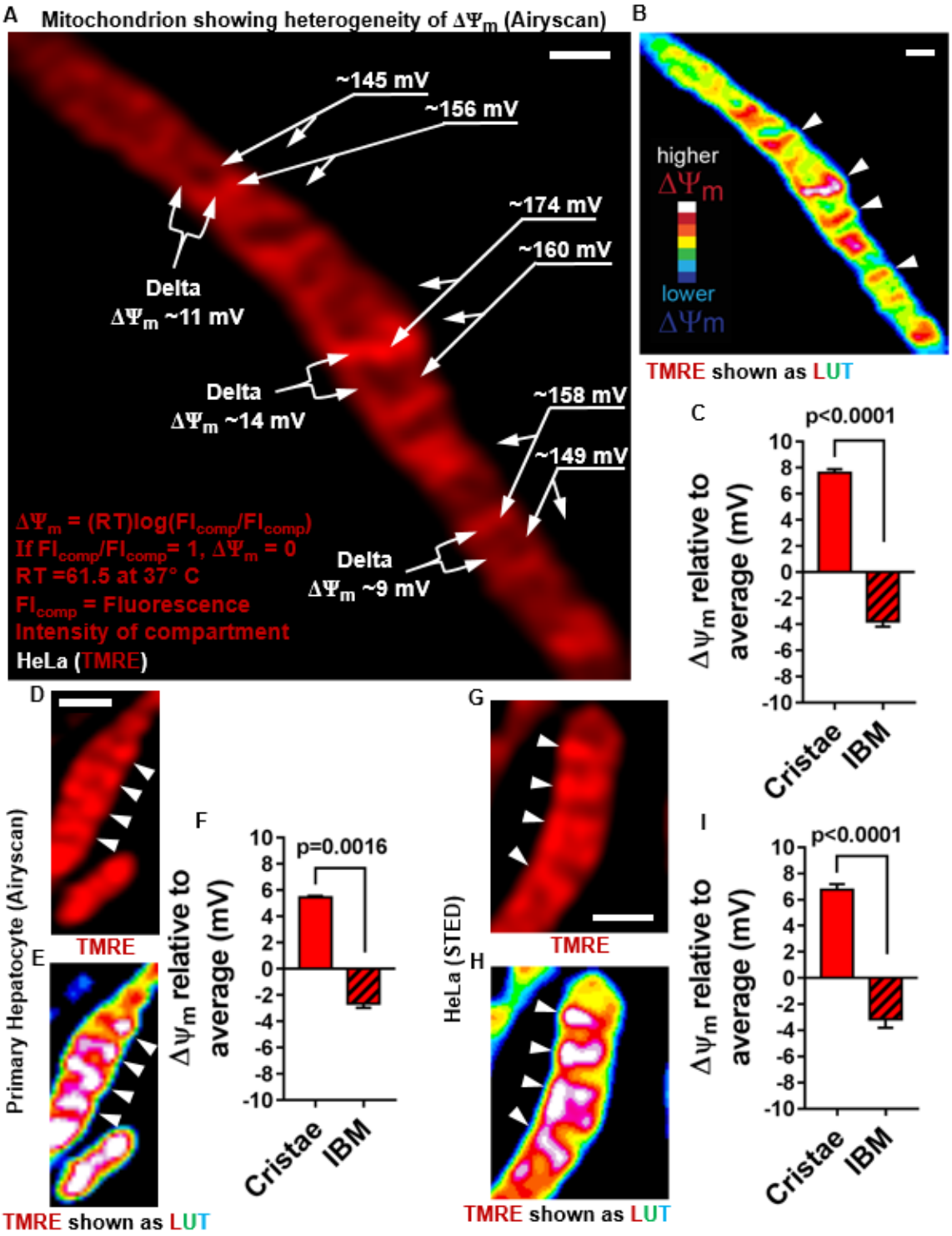


**Figure 2.4. Cristae and IBM have different $\Delta\Psi_m$.**

A. Live-cell Airyscan image of mitochondrion in HeLa cell, showing different membrane potentials in different mitochondrial regions. Membrane potentials were calculated based on TMRE FI differences between compartments ($FI_{comp}$). Regions of interest from cristae and IBM used for $\Delta\Psi_m$ calculations are labeled with arrows on the right-hand side of the mitochondrion, using the cytosol as the reference compartment. Labeled with forks on the left-hand side of the mitochondrion are the calculations of $\Delta\Psi_m$ between individual cristae and their neighboring IBM. Nernst equation used to calculate different voltages. Scale bar = 500 nm.

B. LUT of mitochondrion in HeLa cell shown in A, color-coding TMRE FIs on scale of white (most intense) to blue (least intense): LUT scale shown in lower left-hand corner. Arrowheads indicate cristae. Scale bar = 500 nm. Note that most-intense pixels (white) only associate with cristae.

C. Quantification of $\Delta\Psi_m$ (mV) at cristae and IBM relative to the average $\Delta\Psi_m$ of the whole mitochondrion, calculated as in A. Note: $\Delta\Psi_m$ at cristae is significantly greater than $\Delta\Psi_m$ at IBM, indicating electrochemical boundaries separate these two regions of the IMM. N = 3 independent experiments.

D-F. Live-cell Airyscan imaging of mitochondria in cultured primary mouse hepatocytes stained with TMRE. Arrowheads denote cristae. D. Image showing TMRE-labeled mitochondria. E. LUT color-coding of TMRE FI. F. Quantification of $\Delta\Psi_m$ differences using Nernst equation as shown in A. Scale bar = 500 nm. N = 2 independent experiments.

G-I. Live-cell STED imaging of mitochondria in HeLa cell stained with TMRM. Arrowheads show cristae. Scale bar = 500 nm. G. Image showing TMRM-labeled mitochondrion. H. LUT color-coding of TMRM FI. I. Quantification of $\Delta\Psi_m$ differences using Nernst equation as shown in A. Scale bar = 500 nm. N = 4 independent experiments. Note that calculation of $\Delta\Psi_m$ differences between the compartments based on images captured by STED and by Airyscan were very similar.

Data information: D'Agostino-Pearson omnibus and/or Shapiro-Wilk normality tests were used to assess whether data was normally distributed. Data were analyzed with 2-tailed Student's *t*-tests, and p values < 0.5 were considered statistically significant. Specific p values are indicated in the figure. Error bars indicate SEM.

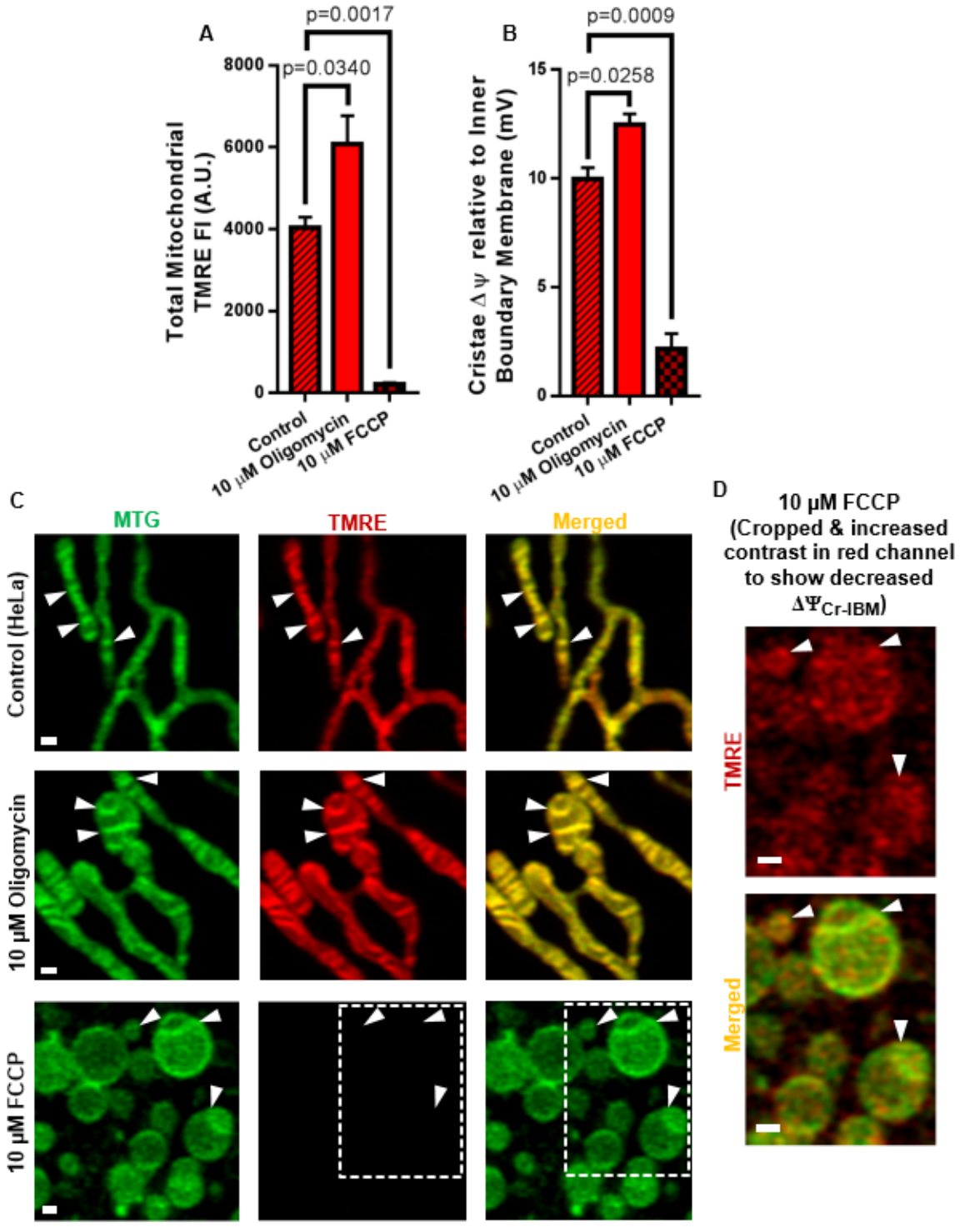


**Figure 2.5. $\Delta\Psi_m$ differences between cristae and IBM are sensitive to $F_1F_o$ ATP Synthase inhibition and uncoupling.**

Response of $\Delta\Psi_m$ to the $F_1F_o$ ATP Synthase inhibitor, oligomycin (10 μM), compared to the uncoupler, FCCP (10 μM), determined using live-cell Airyscan imaging of HeLa cells co-stained with MTG and TMRE.

A. Quantification of total mitochondrial TMRE FI. N = 3 independent experiments.

B. Quantification of cristae $\Delta\Psi_m$ relative to IBM ($\Delta\Psi_{Cr\text{-}IBM}$) in response to oligomycin compared to FCCP. $F_1F_o$ ATP Synthase is exclusively localized to the cristae and significant increase in $\Delta\Psi_{Cr\text{-}IBM}$ in response to blocking of $F_1F_o$ ATP Synthase with oligomycin indicates that differences in TMRE FI between cristae and IBM are driven by oxidative phosphorylation. N = 3 independent experiments.

C. Representative Airyscan images showing mitochondria from living HeLa cells stained with MTG and TMRE. Cells were first stained for one hour and only then treated with oligomycin or FCCP. Images show hyperpolarization of cristae under oligomycin (middle row; arrowheads) and depolarization of cristae under FCCP (bottom row; arrowheads) compared to control (top row; arrowheads). Scale bar = 500 nm. N = 3 independent experiments. Note that the $\Delta\Psi_m$-independent fraction of TMRE staining is less than 5% of the signal in control conditions.

D. Zoomed-in region of FCCP-treated mitochondria in C. Increased contrast was used to visualize TMRE to compensate for TMRE loss induced by FCCP. These images show diminished heterogeneity of $\Delta\Psi_{Cr\text{-}IBM}$ values.

Data information: D'Agostino-Pearson omnibus and/or Shapiro-Wilk normality tests were used to assess whether data was normally distributed. Data were analyzed with 2-

tailed Student's *t*-tests, and p values < 0.5 were considered statistically significant. Specific p values are indicated in the figure. Error bars indicate SEM.

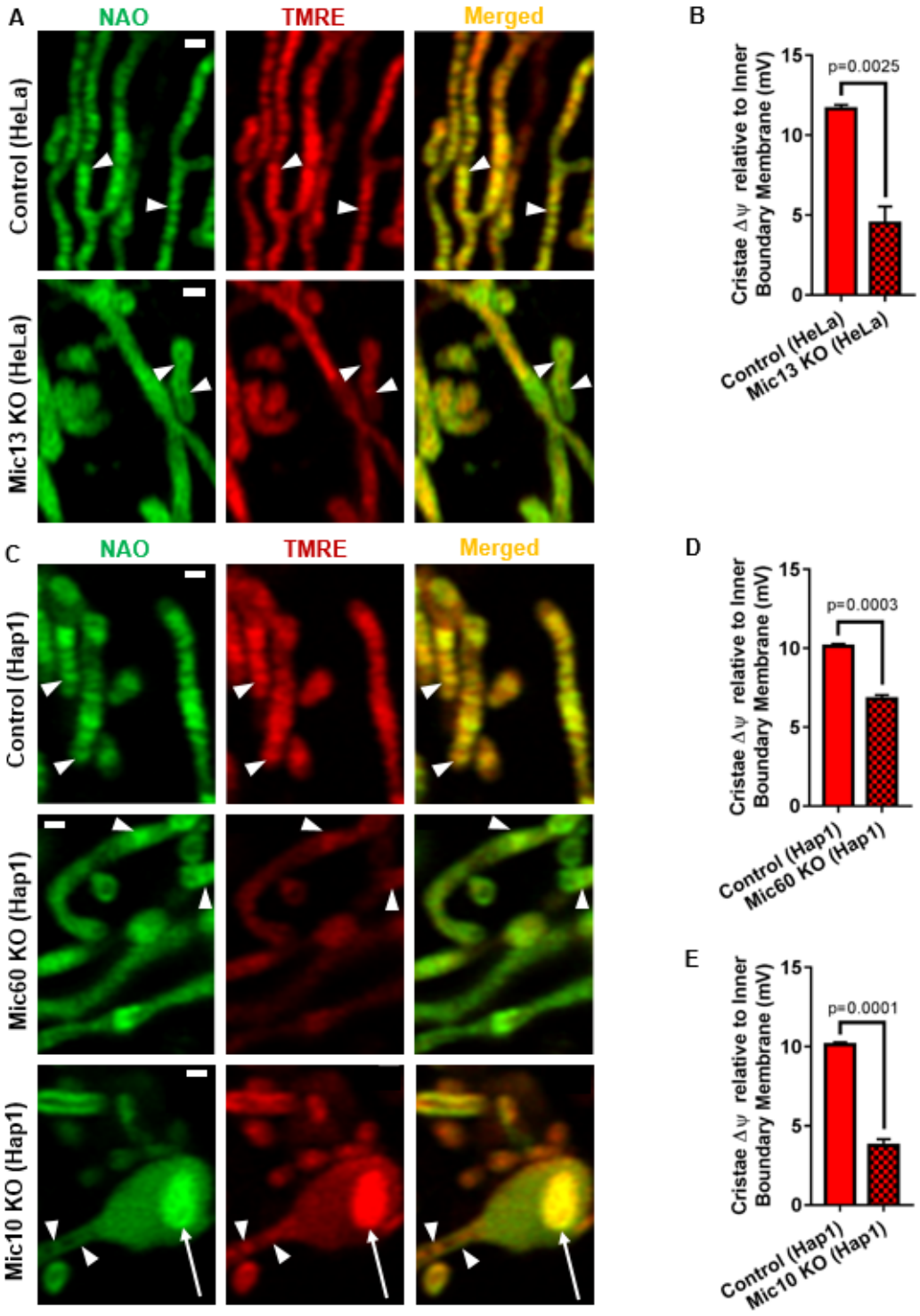


**Figure 2.6. Crista junctions (CJ) regulate the difference in $\Delta\Psi_m$ between cristae and IBM.**

The role of cristae structure as well as CJ formation and sealing on the generation of the difference in $\Delta\Psi_m$ between cristae and IBM were studied by disrupting cristae using Mic10-, Mic13- and Mic60-deficient cells. Mic13 and Mic60 support cristae formation. Mic10 is essential for CJ formation, and, in its absence, cristae tend to remain as vesicles detached from IBM. Live-cell Airyscan imaging of TMRE was used in all figure panels and models.

A. Representative images of mitochondria in control (top row) vs. Mic13-KO (bottom row) HeLa cells. Note that TMRE FI in Mic13-KO mitochondria is distributed more evenly along the IMM, so that $\Delta\Psi_{Cr\text{-}IBM}$ is decreased. Scale bar = 500 nm. N = 3 independent experiments.

B. Quantification of A, showing deletion of Mic13 in HeLa cells results in significant decrease in $\Delta\Psi_{Cr\text{-}IBM}$. While Mic13-KO cells show a substantial decrease in cristae number, the loss of cristae does not appear absolute, making it feasible to compare TMRE FI at cristae relative to IBM. N = 3 independent experiments.

C. Representative images of Hap1 control (top row) vs. Mic60 KO (middle row) and Mic10 KO (bottom row); Mic60-KO mitochondria show very few cristae structures. TMRE staining along the IMM is relatively homogeneous, indicating decreased $\Delta\Psi_{Cr\text{-}IBM}$. In general, Mic10 KO in Hap1 cells results in decreased TMRE signal intensity at cristae relative to IBM (arrowheads) as compared to control cells. Deletion of Mic10 induces detachment of cristae from IBM (see Figure 2.8). Except for the detached cristae vesicles, the TMRE staining is homogeneously distributed in Mic10-KO cells, indicating decreased $\Delta\Psi_{Cr\text{-}IBM}$. Scale bar = 500 nm. N = 3 independent experiments.

D. Quantification of C, showing Mic60 KO in Hap1 cells results in significant decrease in $\Delta\Psi_{Cr\text{-}IBM}$. While Mic60-KO cells show a marked loss of normal cristae structures, depletion of cristae does not appear absolute, making it possible to compare TMRE FI at cristae relative to IBM. N = 3 independent experiments.

E. Quantification of C, showing Mic10 KO in Hap1 cells results in a significant decrease in $\Delta\Psi_{Cr\text{-}IBM}$. Note: quantification of $\Delta\Psi_m$ at cristae relative to IBM was performed only on cristae structures that appeared to maintain attachment to IBM. N = 3 independent experiments.

Data information: D'Agostino-Pearson omnibus and/or Shapiro-Wilk normality tests were used to assess whether data was normally distributed. Data were analyzed with 2-tailed Student's *t*-tests, and p values < 0.5 were considered statistically significant. Specific p values are indicated in the figure. Error bars indicate SEM.

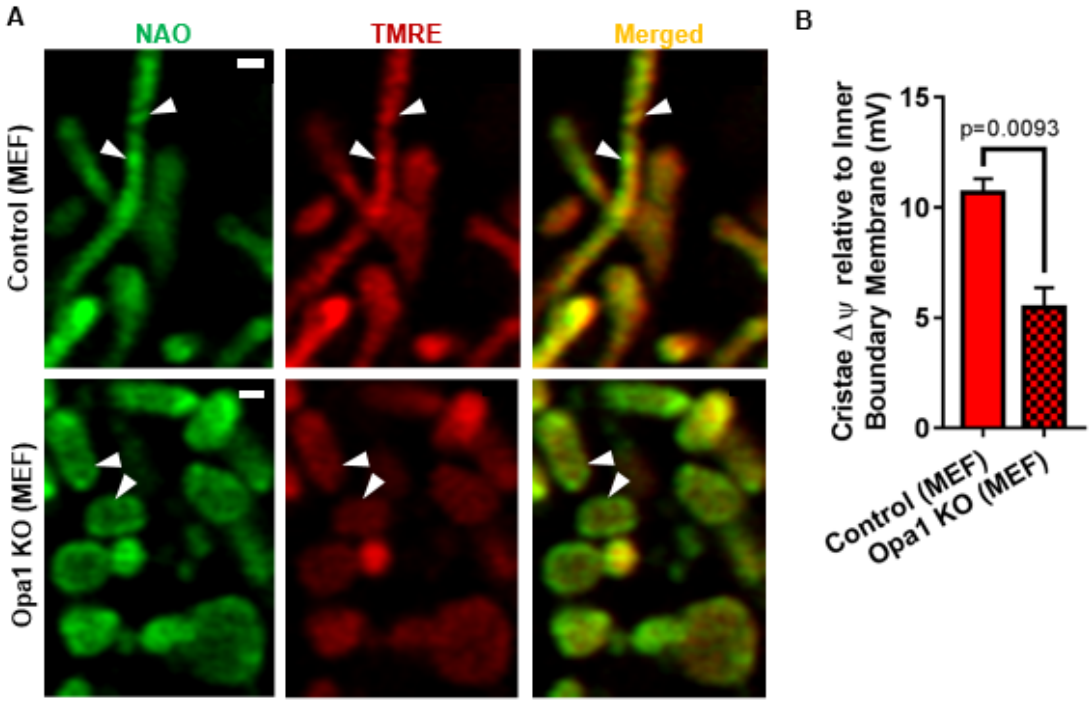


**Figure 2.7. Opa1 regulates the difference in $\Delta\Psi_m$ between cristae and IBM.**

Studies show that Opa1 interacts with MICOS complex, promoting closure of CJs. Thus, we tested whether Opa1 was required to maintain the difference in $\Delta\Psi_m$ between cristae and IBM.

A. Live-cell Airyscan images of MEF control (top row) vs. Opa1 KO (bottom row), co-stained with NAO and TMRE. Arrowheads indicate decreased intensity of TMRE FI at cristae compared to IBM. Note the more even distribution of TMRE staining, indicating the cristae and IBM are relatively equipotential. Scale bar = 500 nm.

B. Quantification of G, showing Opa1-KO MEFs have significantly decreased $\Delta\Psi_{Cr\text{-}IBM}$. N = 3 independent experiments.

Data information: D'Agostino-Pearson omnibus and/or Shapiro-Wilk normality tests were used to assess whether data was normally distributed. Data were analyzed with 2-tailed Student's *t*-tests, and p values $< 0.5$ were considered statistically significant. Specific p values are indicated in the figure. Error bars indicate SEM.

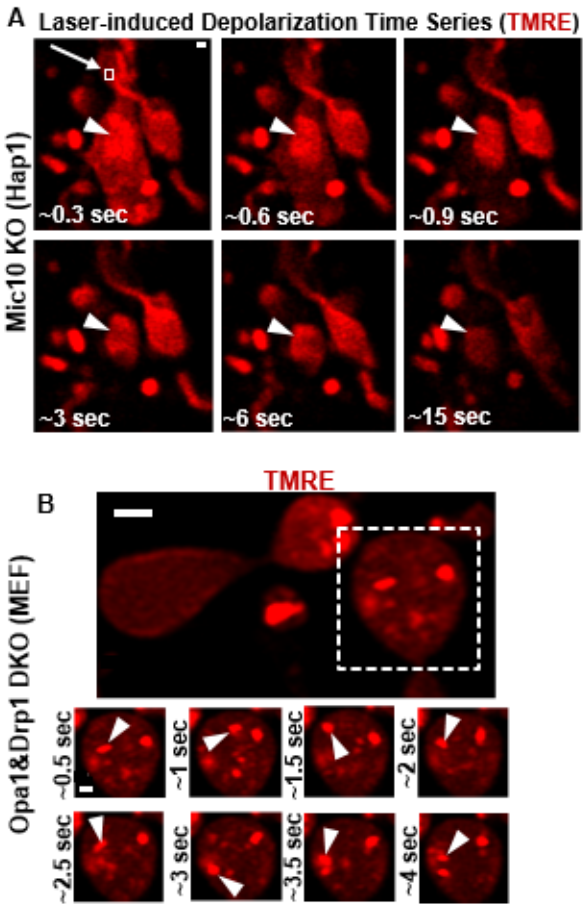


**Figure 2.8. The largest differences in $\Delta\Psi_{Cr\text{-}IBM}$ arise in cristae vesicles generated by deleting CJ regulators.**

A. Live-cell Airyscan images of laser-induced depolarization time series of Mic10 KO Hap1 cell stained with TMRE. Mitochondrion exposed to rapid, high 2-photon laser power in region of white box, arrow (~0.3 sec); large, hyperpolarized vesicle (arrowhead) remains polarized after the rest of the mitochondrion loses $\Delta\Psi_m$, indicating electrochemical discontinuity between hyperpolarized vesicles and the rest of the mitochondrion, including the IBM. Scale bar = 500 nm. N = 2 independent experiments.

B. Live-cell Airyscan image of time series showing hyperpolarized vesicles (arrowheads; region cropped from dashed white box) inside mitochondria lacking both Opa1 and Drp1. Scale bar = 500 nm. N = 2 independent experiments. Free movement of hyperpolarized vesicles within the matrix indicate their detachment from the IBM, representing an extreme case of cristae independency within one mitochondrion (see Movie EV 1 for time series).

Data information: D'Agostino-Pearson omnibus and/or Shapiro-Wilk normality tests were used to assess whether data was normally distributed. Data were analyzed with 2-tailed Student's *t*-tests, and p values < 0.5 were considered statistically significant. Specific p values are indicated in the text.

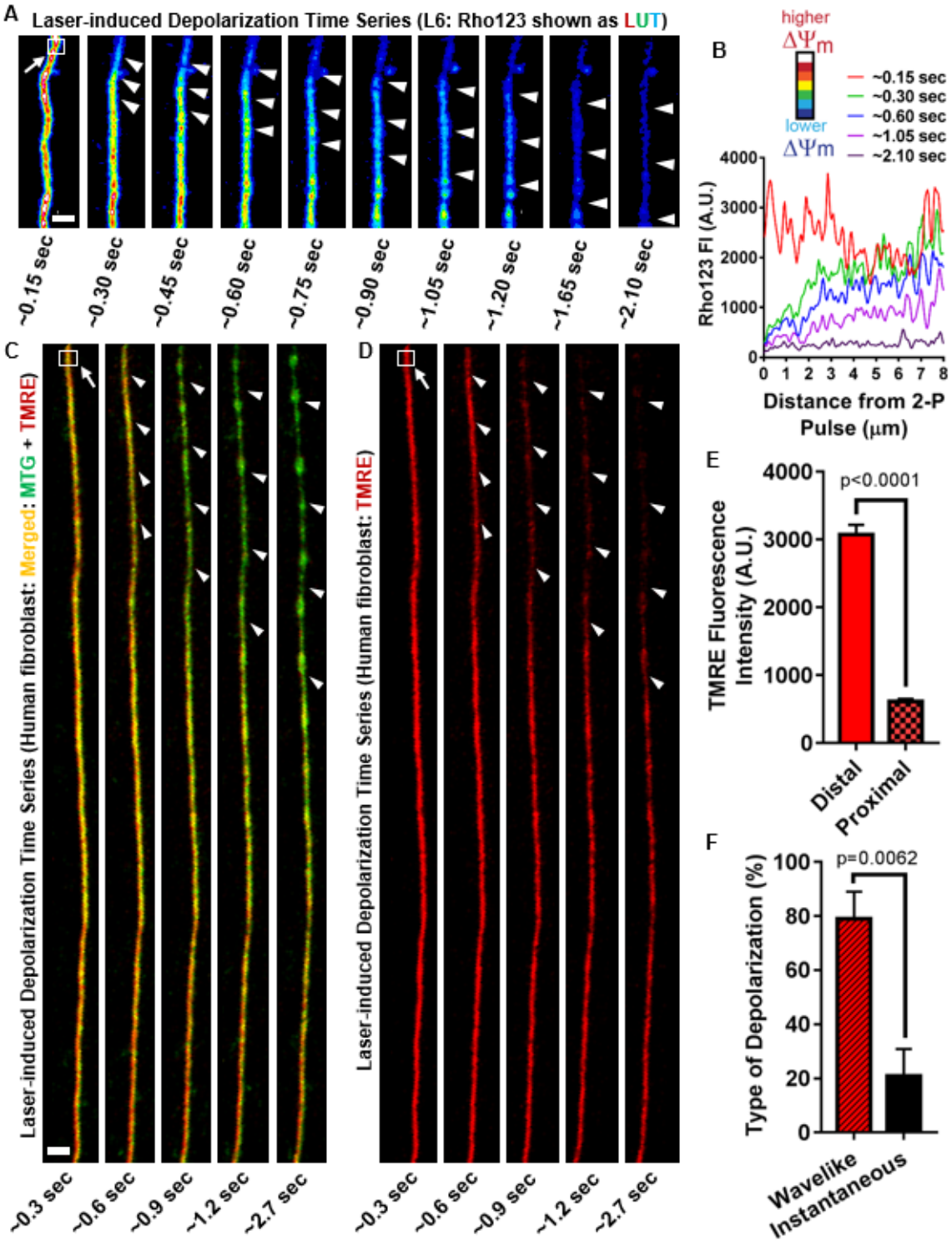


**Figure 2.9. Laser-induced depolarization results in non-instantaneous loss of $\Delta\Psi_m$ along the single mitochondrion.**

A-B. Laser-induced mitochondrial membrane depolarization in L6 myoblasts shows gradual depolarization of elements along the IMM, visualized using live-cell Airyscan microscopy.

A. Representative images of laser-induced depolarization time series from L6 myoblast, stained with $\Delta\Psi_m$-dependent dye, Rho123. Images show LUT color-coded for Rho123 FI. White and blue pixels represent most and least intense $\Delta\Psi_m$, respectively. See legend of LUT colors on the right. Note that at the first time point (~0.15 sec) white arrow points to box marking area of mitochondrion exposed to phototoxic pulse of 2-photon laser (≤5 msec), inducing depolarization. Ensuing frames show wavelike depolarization away from site of perturbation (arrowheads). Scale bar = 500 nm. N = 3 independent experiments. (See Movie EV 2 for time series.)

B. Profile plot showing Rho123 pixel intensity as function of distance along mitochondrion in A. Note that zero value in the X axis corresponds to top area of the mitochondrion shown in A, near site of 2-photon laser exposure (box). Red line corresponds to frame immediately before depolarization (~0.15 sec); green, blue, purple, and dark purple lines correspond to ~0.30, ~0.60, ~1.05, and ~2.10 sec, respectively, after initial depolarization, showing wavelike dissipation of $\Delta\Psi_m$ over time.

C-F. Laser-induced mitochondrial membrane depolarization in living human skin fibroblasts co-stained with TMRE and MTG and imaged with Airyscan, showing gradual depolarization of elements along the IMM.

C. Time-lapse images of merged green (MTG) and red (TMRE) channels following laser-induced mitochondrial membrane depolarization. Note that, at the first time point

(0.3 sec), white arrow points to box marking area of mitochondrion exposed to phototoxic pulse of 2-photon laser (≤5 msec), inducing depolarization. Depolarization is marked by the dissipation of the $\Delta\Psi_m$-dependent dye (TMRE) while the green (MTG) signal persists. Scale bar = 1 μm. N = 4 independent experiments.

D. TMRE channel from C, showing gradual of the loss of TMRE along the IMM. Note that although depolarization has largely completed at the area near the phototoxic stimulus already at 0.9 sec, some specific regions at the very top maintain $\Delta\Psi_m$ while others depolarize.

E. Quantification of $\Delta\Psi_m$ using TMRE FI from C-D. Measurement of TMRE pixel intensities immediately after laser-induced depolarization at site distal (≥ 10 μm) vs. proximal (≤ 1 μm) to box. N = 4 independent experiments; see specific p values in panel.

F. Quantification of C-D. Percentage of mitochondria that depolarize in a wavelike (*i.e.*, gradual) vs. instantaneous manner after laser-induced depolarization. Note: imaging at high temporal resolution (~100-500 msec/frame) reveals wavelike depolarizations predominate, suggesting the $\Delta\Psi_m$ is composed of multiple, disparate electrochemical domains along the IMM. The time scale of propagation of depolarization is slower than the propagation of electrical phenomena. N = 4 independent experiments.

Data information: D'Agostino-Pearson omnibus and/or Shapiro-Wilk normality tests were used to assess whether data was normally distributed. Data were analyzed with 2-tailed Student's *t*-tests, and p values < 0.5 were considered statistically significant. Specific p values are indicated in the figure. Error bars indicate SEM.

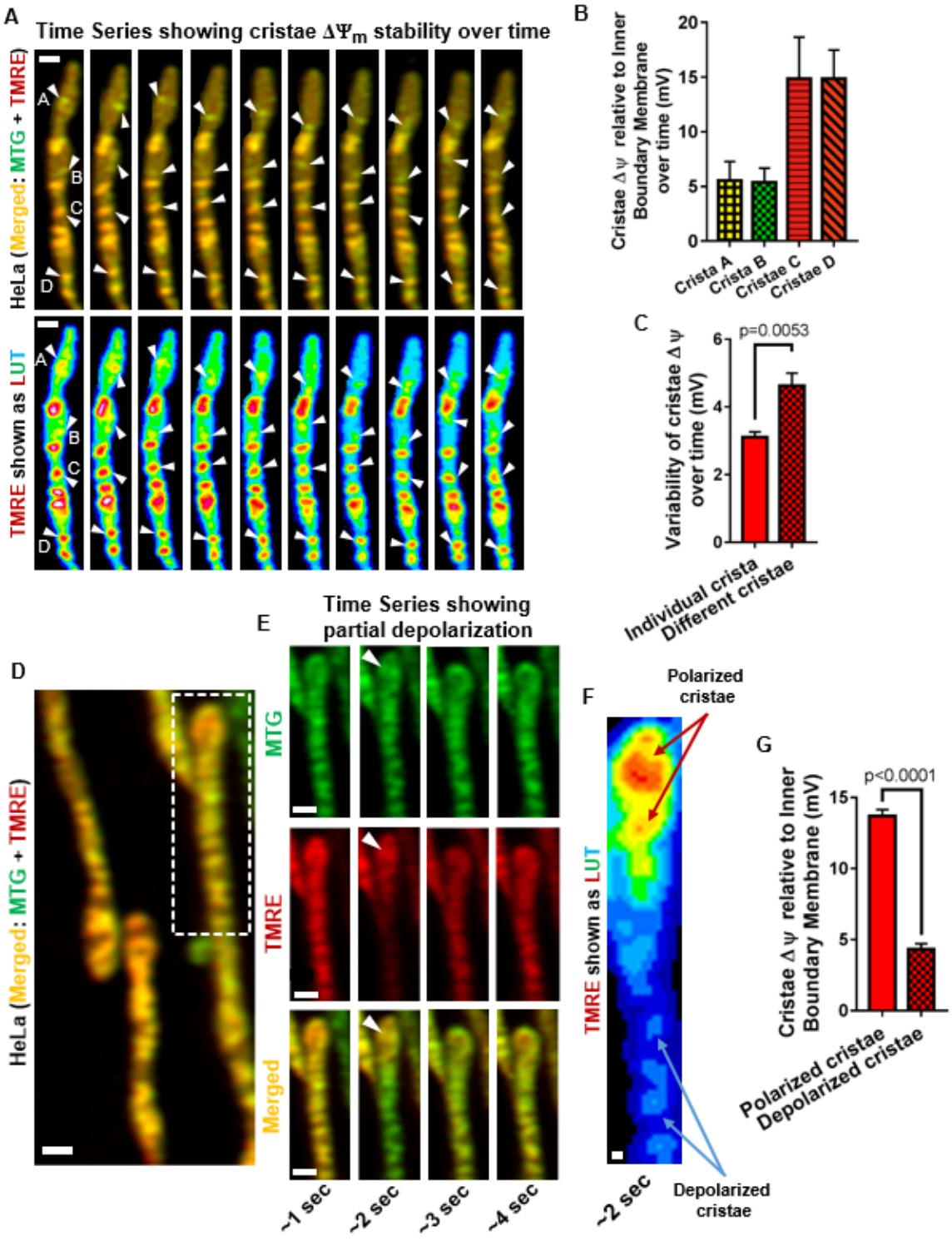


**Figure 2.10. Cristae are unique electrochemical domains, thus constituting independent bioenergetic units.**

We calculated the $\Delta\Psi_{Cr\text{-}IBM}$ between neighboring cristae over time as a surrogate measure of cristae individuality and functional independence, using live-cell Airyscan imaging.

A. Stability of cristae $\Delta\Psi_{Cr\text{-}IBM}$ over time. Representative images from time series of HeLa cells co-stained with MTG and TMRE. Top sequence shows merged green (MTG) and red (TMRE) channels. Bottom sequence shows color-coded LUT of TMRE signal of the same sequence shown above. White arrowheads in the image point to specific cristae that were measured over time. Scale bar = 500 nm. N = 5 independent experiments.

B. Quantification of A, showing average $\Delta\Psi_{Cr\text{-}IBM}$ of Cristae "A-D" over time. Note that Cristae C and D maintain more than double the $\Delta\Psi_{Cr\text{-}IBM}$ of Cristae A and B. Error bars indicate STDEV.

C. Quantification of A, showing standard deviation in $\Delta\Psi_{Cr\text{-}IBM}$ (mV) of individual cristae over time compared to the standard deviation in $\Delta\Psi_{Cr\text{-}IBM}$ (mV) among different cristae along a single mitochondrion. N = 5 independent experiments. Note that there is less variability in $\Delta\Psi_{Cr\text{-}IBM}$ of a single crista over time within the same mitochondrion compared to the variability of $\Delta\Psi_{Cr\text{-}IBM}$ among cristae over time, indicating cristae possess unique bioenergetic properties.

D-G. Airyscan time series of TMRE flickering in HeLa cells co-stained with MTG and TMRE, showing that depolarization is uncoordinated along the IMM with some cristae depolarizing while neighboring cristae remain polarized.

D. Representative live-cell Airyscan image from time series showing merged green (MTG) and red (TMRE) channels. Area marked by dashed box is shown in the time series in E. Scale bar = 500 nm.

E. Time series of cropped region from D, showing tip of mitochondrion (arrowhead) maintaining $\Delta\Psi_m$ while neighboring region of same mitochondrion depolarizes. The capacity of some cristae to maintain polarity, while adjacent cristae transiently depolarize, indicates cristae can exhibit a significant amount of electrochemical autonomy. N = 3 independent experiments. (See Movies EV 3, 4 for time series.)

F. Zoomed-in LUT of mitochondrion from E (~2 sec), showing some cristae remaining polarized (red) while adjacent cristae depolarize (blue). (See Movie EV 5 for time series.)

G. Quantification of D-F, showing that during a flickering event some cristae maintain their membrane potentials while other cristae depolarize, resulting in large differences in $\Delta\Psi_{Cr\text{-}IBM}$ along the individual mitochondrion. N = 3 independent experiments.

Data information: D'Agostino-Pearson omnibus and/or Shapiro-Wilk normality tests were used to assess whether data was normally distributed. Data were analyzed with 2-tailed Student's *t*-tests, and p values < 0.5 were considered statistically significant. Specific p values are indicated in the figure. Error bars indicate SEM, except in panel B, which show STDEV.

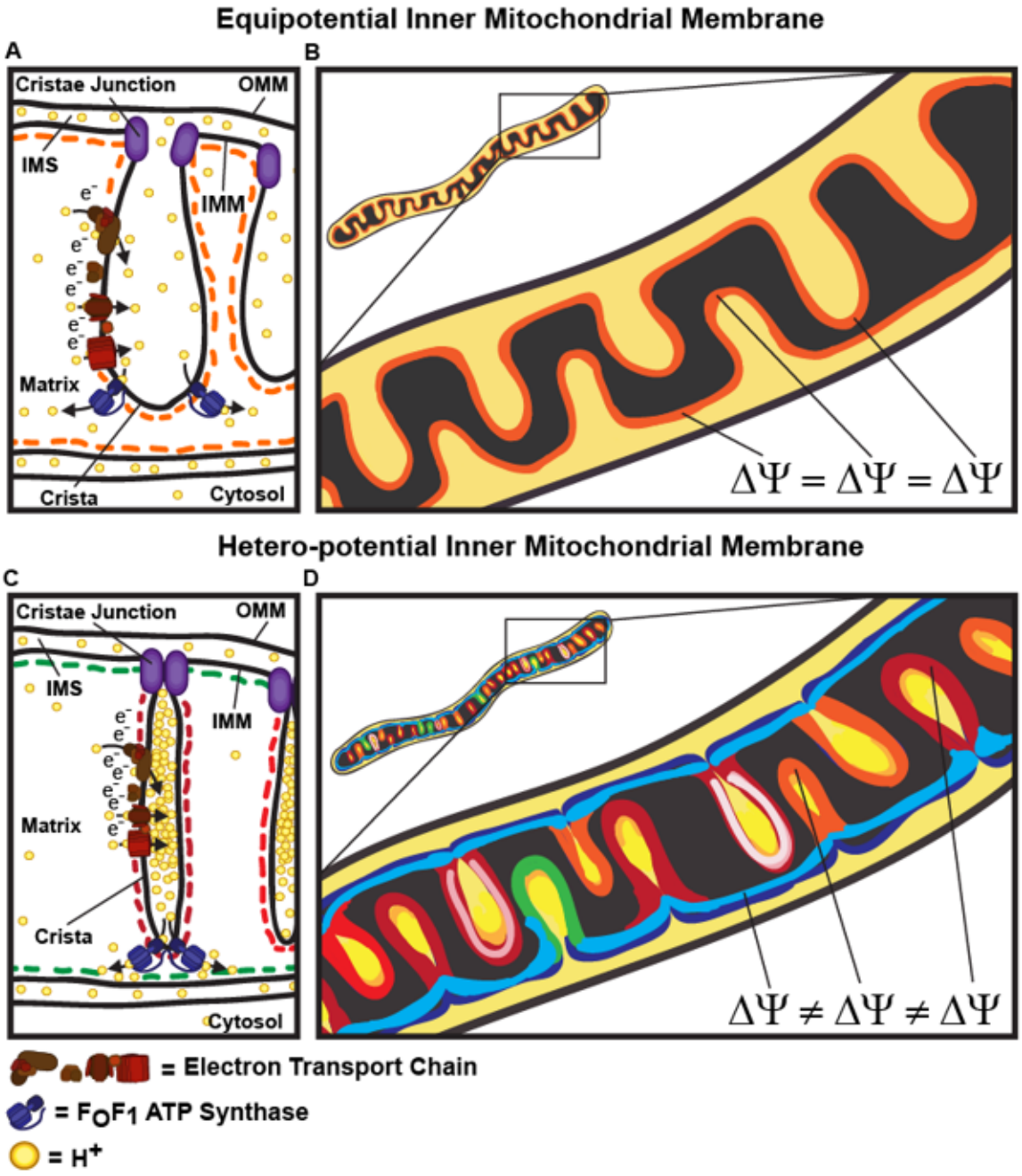


**Figure 2.11. Model of cristae as individual bioenergetic units**

A. An equipotential representation of the IMM. In this model the IMM functions as a continuous electrical cable where cristae and IBM have similar $\Delta\Psi_m$ and where all cristae respond simultaneously to any change in $\Delta\Psi_m$ occurring in the mitochondrion where they

reside. Transition from a hetero-potential to an equipotential, via cleavage of Opa1, for example, could play a role in normal mitochondrial physiology where conditions favor high conductance and low ATP synthesis, such as thermogenesis or adaptation to excess nutrient.

B. Cartoon showing IMM as equipotential.

C. Model of mitochondrial hetero-potential, showing cristae as individual bioenergetic units. Electrochemical autonomy of cristae protects the mitochondrion confronting a bioenergetic crisis, where dysfunction of one or more cristae would not inevitably cause the entire organelle to fail. In this model, cristae and IBM can have different membrane potentials. Closed CJs generate significant differences in charge between the cristae membranes and IBM, which could be related to the concentration of ETC subunits in the lateral side of the cristae and $F_1F_o$ ATP Synthase on the cristae rims.

D. Cartoon showing IMM as hetero-potential.

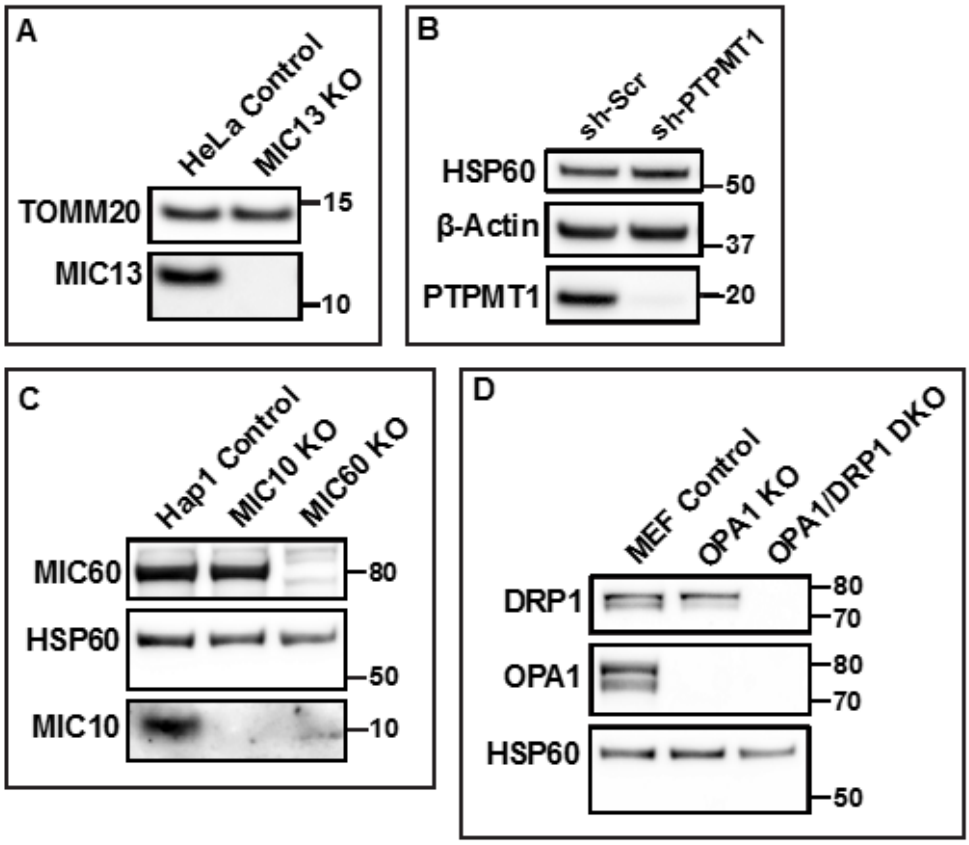


**Figure Expanded View 2.1.**

A. Representative image of Western blot, showing deletion of MIC13 in HeLa cells. N = 3 independent experiments.

B. Representative image of Western blot, showing deletion of PTPMT1 in H1975 cells. N = 3 independent experiments.

C. Representative image of Western blot, showing deletion of MIC60 and MIC10 in Hap1 cells. N = 3 independent experiments.

D. Representative image of Western blot, showing Opa1 KO and Opa1&Drp1 DKO in MEFs. N = 3 independent experiments.

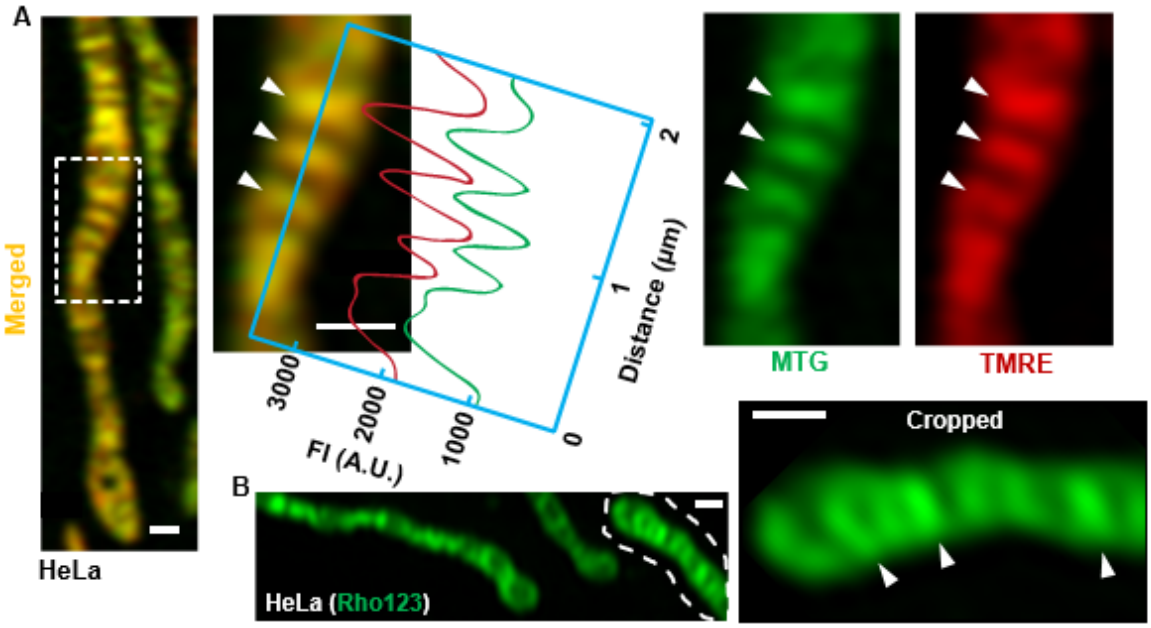


**Figure Expanded View 2.2.**

A. Mitochondria in HeLa cells co-stained with MTG and TMRE. Zoomed-in region from dashed white box highlights colocalization of dyes, showing that signal intensities vary together across the long axis (green and red lines); arrowheads indicate cristae membranes.

B. Mitochondria in HeLa cell stained with $\Delta\Psi_m$-dependent dye, Rho123; zoomed-in mitochondrion cropped from dashed line highlights more intense signal at cristae. N = 3 independent experiments.

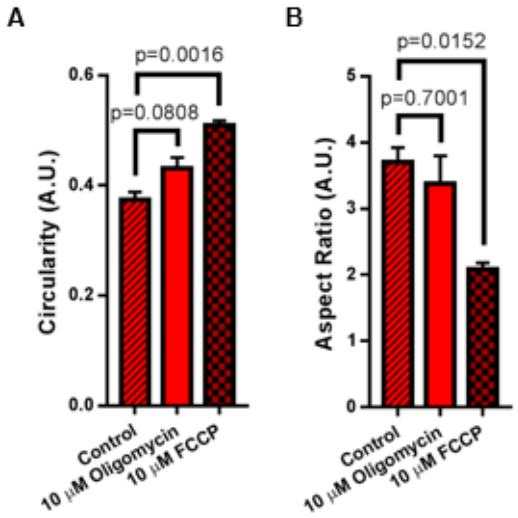


**Figure Expanded View 2.3.**

A. Quantification of mitochondrial circularity, where mitochondria with circularity closer to 1 resemble a circular object and mitochondria with circularity closer to 0 resemble a branched object. Note: FCCP results in significant increase in mitochondrial circularity, consistent with numerous studies indicating FCCP induces fragmentation. N = 3 independent experiments.

B. Quantification of mitochondrial aspect ratio (a ratio of the long axis of the mitochondrion to the short axis), where mitochondria with an aspect ratio closer to 1 are rounder, whereas mitochondria higher and higher than 1 are increasingly elongated. Note: FCCP also leads to a significant decrease in aspect ratio, indicating loss of membrane potential results in fragmentation. N = 3 independent experiments.

Data information: D'Agostino-Pearson omnibus and/or Shapiro-Wilk normality tests were used to assess whether data was normally distributed. Data were analyzed with 2-

tailed Student's *t*-tests, and p values < 0.5 were considered statistically significant. Specific p values are indicated in the figure. Error bars indicate SEM.

**Movie Expanded View 2.1.**

Hyperpolarized vesicles moving haphazardly within the matrix of Opa1&Drp1-DKO mitochondria.

**Movie Expanded View 2.2.**

Laser-induced depolarization of mitochondrion from L6 myoblast stained with Rho123, showing wavelike depolarization.

**Movie Expanded View 2.3.**

Mitochondrion from HeLa cell stained with MTG and TMRE, showing partial depolarization during random flickering event.

**Movie Expanded View 2.4.**

Mitochondrion from HeLa cell stained with MTG and TMRE, showing partial depolarization during random flickering event. Note: this movie shows the red (TMRE) channel only.

**Movie Expanded View 2.5.**

Mitochondrion from HeLa cell stained with MTG and TMRE, showing partial

depolarization during random flickering event. Note: this movie shows the (TMRE) channel as an LUT to highlight the asymmetrical distribution of the $\Delta\Psi_m$-dependent dye in the polarized (red) vs. depolarized (blue) regions.

# CHAPTER THREE

## Quantification of cristae architecture reveals time-dependent characteristics of individual mitochondria

Mayuko Segawa[1,*], Dane M. Wolf[1,2,*], Nan W. Hultgren[3], David S. Williams[3], Alexander M. van der Bliek[4,5], David B. Shackelford[6], Marc Liesa[1,7,#], Orian S. Shirihai[1,7,#]

1. Department of Medicine, and Department of Molecular and Medical Pharmacology, David Geffen School of Medicine, University of California Los Angeles, CA 90095, USA.

2. Graduate Program in Nutrition and Metabolism, Graduate Medical Sciences, Boston University School of Medicine, Boston, MA 02118, USA.

3. Departments of Ophthalmology and Neurobiology, Stein Eye Institute, David Geffen School of Medicine, University of California, Los Angeles, CA, USA.

4. Molecular Biology Institute at UCLA, Los Angeles, CA 90095, USA.

5. Department of Biological Chemistry, David Geffen School of Medicine at UCLA, Los Angeles, CA 90095, USA.

6. Department of Pulmonary and Critical Care Medicine, David Geffen School of Medicine, University of California, Los Angeles, CA 90095, USA; Jonsson Comprehensive Cancer Center, David Geffen School of Medicine, University of California, Los Angeles, CA 90095, USA.

7. Department of Molecular and Medical Pharmacology, David Geffen School of Medicine, University of California, 650 Charles East Young Drive South, 27-200, Los Angeles, California 90095, USA.

# Corresponding authors: email: mliesa@mednet.ucla.edu, OShirihai@mednet.ucla.edu

* These first authors contributed equally to this study.

**Running title:** Live-cell cristae segmentation

**Keywords:** cristae, mitochondria, Trainable Weka Segmentation, machine learning, image analysis, Airyscan, SIM, superresolution

**Summary blurb**

A novel, machine-learning approach to quantify cristae density and architecture in live-cell superresolution imaging characterizes the ultrastructural parameters of individual mitochondria over time.

**Abstract**

Recent breakthroughs in live-cell imaging have enabled visualization of cristae, making it feasible to investigate the structure-function relationship of cristae in real time. However, quantifying live-cell images of cristae in an unbiased way remains challenging. Here, we present a novel, semi-automated approach to quantify cristae, using the machine-learning

Trainable Weka Segmentation (TWS) tool. Compared to standard techniques, our approach not only avoids the bias associated with manual thresholding but more efficiently segments cristae from Airyscan and structured illumination microscopy (SIM) images. Using a cardiolipin-deficient cell line, as well as FCCP, we show that our approach is sufficiently sensitive to detect perturbations in cristae density, size, and shape. This approach, moreover, reveals that cristae are not uniformly distributed within the mitochondrion, and sites of mitochondrial fission are localized to areas of decreased cristae density. Following a fusion event, individual cristae from the two mitochondria, at the site of fusion, merge into one object with distinct architectural values. Overall, our study shows that machine learning represents a compelling new strategy for quantifying cristae in living cells.

**Introduction**

Mitochondria are dynamic, double-membrane-bound organelles (Cogliati *et al*., 2016; Friedman and Nunnari, 2014). A relatively porous outer mitochondrial membrane (OMM) encapsulates a protein-dense inner mitochondrial membrane (IMM), which consists of numerous invaginations, called cristae (Palade, 1953). Over the last decade or so, different studies have demonstrated that the molecular machinery of oxidative phosphorylation is concentrated in cristae membranes (Davies *et al*., 2011; Dudkina *et al*., 2005; Strauss *et al*., 2008; Vogel *et al*., 2006; Wilkens *et al*., 2013). Nevertheless, directly probing the functional significance of cristae structure has been hindered by a longtime inability to visualize the IMM in living cells (Jakobs and Wurm, 2014). While

electron microscopy (EM) can resolve cristae effectively, it is necessary to freeze or fix samples prior to imaging, which precludes any direct functional readout. Conventional light microscopy, on the other hand, permits live-cell imaging, but the Abbe diffraction limit (approximately 200 nm) has prevented the simultaneous resolution of mitochondrial ultrastructure (Jakobs *et al*., 2020).

Recent advancements, however, in high- and superresolution technologies (*e.g.*, Airyscan, SIM, and STED) have enabled the visualization of cristae in living cells (Huang X *et al*., 2018; Jakobs *et al*., 2020; Kondadi *et al*., 2020; Stephan *et al*., 2019; Wang C *et al*., 2019; Wolf *et al*., 2019; Wolf *et al*., 2020). Remarkably, cristae appear to exhibit their own dynamic behaviors (Huang X *et al*., 2018; Kondadi *et al*., 2020; Stephan *et al*., 2019; Wang C *et al*., 2019) and display disparate membrane potentials ($\Delta\Psi_m$), indicating that they function as independent bioenergetic units (Wolf *et al*., 2019). Powerful new techniques for visualizing cristae in living cells necessitate proportionately robust methods for quantification. In this study, we present a novel approach using the open-source plugin, Trainable Weka Segmentation (TWS) (Arganda-Carreras *et al*., 2017; Hall, 2009), to measure cristae. This semi-automated method is beneficial because it avoids the bias and inefficiency associated with manual segmentation (Caffrey *et al*., 2019) and is able to detect significant differences in cristae density and architecture, resulting from pathological changes in IMM integrity. Our approach is also sufficiently sensitive to measure the remodeling of individual cristae within the same mitochondrion as well as shed light on the dynamic changes in the IMM during mitochondrial fusion and

fission.

Numerous studies have demonstrated a link between perturbed cristae structure and a variety of human diseases and medical complications – ranging from diabetes to liver steatosis, from ischemia reperfusion injury to even aging (Acehan *et al*., 2007; Amati-Bonneau *et al*., 2008; Birk *et al*., 2013; Daum *et al*., 2013; Mamikutty *et al*., 2015; Sivitz and Yorek, 2010; Vincent *et al*., 2016; Zick *et al*., 2009). Our TWS approach provides a novel platform for directly probing the role of IMM architecture in normal as well as dysfunctional mitochondria and represents a new tool for deciphering the complex relationship between mitochondrial membranes and organismal homeostasis.

**Methods**

**Cell culture.** sh-Scramble and sh-PTPMT1 H1975 cells were cultured in RPMI-1640 (31800-022), supplemented with sodium bicarbonate, Pen/Strep, sodium pyruvate, HEPES, and 10% FBS and grown in 5% $CO_2$ at 37°C. L6, HUH7, and HeLa cells were grown in DMEM (12100-046) and supplemented with sodium bicarbonate, Pen/Strep, sodium pyruvate, HEPES, and 10% FBS and cultured in 5% $CO_2$. KD of PTPMT1 was performed as we previously described (Wolf *et al*., 2019).

**Live-cell imaging.** Airyscan: CELLview 4-compartment glass-bottom tissue culture dishes (Greiner Bio-One, 627870), PS, 35/10 mm were used for imaging cells. 100 nM 10-*N*-nonyl acridine orange (NAO), 5 μM Rho123, or 200 nM MitoTracker Green

(MTG) (Invitrogen) were added to cell culture media and incubated 1-3 hr before live-cell imaging. The alpha Plan-Apochromat 100X/1.46 Oil DIC M27 objective on the Zeiss LSM 880 with Airyscan was used for imaging. Before image analysis, raw .czi files were automatically processed into deconvolved Airyscan images using the Zen software. Structured Illumination (SIM): The GE DeltaVision OMX SR system with a 60X oil-immersion lens was used to conduct structured illumination superresolution microscopy. Prior to live-cell imaging, the system was equilibrated to 37°C with 10% $CO_2$ in humidified chamber. Samples were imaged in regular growth media. Immersion oil with refractive index of 1.522 was used. MTG was excited with the 488-nm laser. For z-stacks, section thickness was set to the 0.125 μm (optimal). For time-lapse imaging, a single plane was imaged at approximately 2-s intervals.

**Image analysis.** Processed Airyscan as well as SIM images were analyzed with ImageJ (Fiji) software, NIH (Schneider et al., 2012). Before cell cropping and quantification, background was subtracted from images using a rolling ball filter = 50. After developing analysis procedures, we built macros for high-throughput image quantification. For representative images in figures, we adjusted pixel intensities to optimally show relevant changes in IMM structure.

**Statistical Analysis.** Statistical analysis was done on GraphPad Prism and Microsoft Excel. Independent experimental data sets were subjected to D'Agostino-Pearson omnibus and/or Shapiro-Wilk normality tests to assess whether data were normally

distributed. Data were subjected to parametric or nonparametric 2-tailed Student's *t*-tests or one-way ANOVA, depending on whether data were normally distributed or not. P values < 0.05 were considered statistically significant. Error bars represent SD of the mean. N = the number of independent experiments. An average of 15 cells were analyzed in each independent experiment. Statistical analysis was conducted on the averages from independent experiments.

**Step-by-step workflow of Trainable Weka Segmentation (TWS) protocol for segmenting mitochondrial cristae.** Generate 16-bit Airyscan images of mitochondria showing cristae (Fig 3.1A). Next, open an Airyscan image and perform a background subtraction with a rolling ball filter = 50. Note: the scales of the images do not need to be manually specified, as this information is contained in the metadata of the image. Then, open the Trainable Weka Segmentation plugin in the online Fiji software (Arganda-Carreras *et al*., 2017; Hall, 2009) by going to the (Fiji Is Just) ImageJ menubar and clicking "Plugins" → "Segmentation" → "Trainable Weka Segmentation". After loading an Airyscan image of mitochondria into the plugin window, proceed with the following steps to train the cristae classifier:

1. On the left-hand side of the window, click "Settings" to open the Segmentation settings dialog box, and select specific Training features (*e.g.*, "Sobel filter", an edge-detecting algorithm, "Membrane projections", a feature that enhances membranous structures, and "Gaussian blur", which reduces noise) to determine the manner in which

the machine-learning protocol segments objects within images.

2. In the Segmentation settings dialog box, create 2 classes of objects: Class 1 “Cristae”; Class 2 “Background”. Click OK.
3. Use the cursor to mark structures that you identify as cristae (Fig S3.1A) and click on the “Add to Cristae” box on the right-hand side of the TWS window. Next, use the cursor to mark regions that you identify as background (*i.e.*, not cristae) and click on the “Add to Background” box on the right-hand side of the TWS window.
4. Repeat this process numerous times on different regions identified by the user as cristae or as background within the same cell.
5. Click the “Train classifier” button on the left-hand side of the TWS window to initiate the training process. After the training is finished, an overlay image will appear, showing the two classes: “Cristae” as reddish brown and “Background” as green areas (Fig S3.1B). Note: this process can be repeated as much as necessary until the user is satisfied with the accuracy of the segmentation. Click “Toggle overlay” to assess the progress of the training, as needed.
6. After finishing with training the classifier, click the “Save data” button on the left-hand side of the TWS window. Saving the data associated with TWS training will generate a .arff file. Next, click the “Save classifier” button on the left-hand side of the TWS window. This will generate a separate .model file. Note: to train the TWS classifier on

additional images, it is necessary to load the previous .arff file into a new TWS window to build upon the data from previous training sessions.

7. Close the Trainable Weka Segmentation window.

After training the classifier to effectively segment cristae from Airyscan images, proceed with the following steps to analyze the cristae architecture:

8. Open an Airyscan image (with background subtracted, as indicated above).
9. Duplicate this image (Ctrl+Shift+D) for a later stage of analysis.
10. In the (Fiji Is Just) ImageJ menubar, click "Plugins" → "Segmentation" → "Trainable Weka Segmentation".
11. Click "Load classifier" on the left-hand side of the TWS window to load finished cristae classifier, created from training sessions in previous section (steps 1–7).
12. Click "Get probability" on the left-hand side of the TWS window, which generates a stack of images showing the probability that each pixel belongs to a particular class of objects (Fig 3.1B). Note that, in channel 1, the white pixels correspond to areas that the classifier determined to be probable cristae structures, whereas the black regions belong to background. The pixels in channel 2 (not shown) are the inverse of those in channel 1.

13. Next, from the (Fiji Is Just) ImageJ menubar, click “Image” → “Stacks” → “Stack to Images”. Note: Since the channel-2 image (*i.e.*, the probability map of the background) is not required for further analysis, close it.
14. Click on the image containing the cristae probability map, and then, from the (Fiji Is Just) ImageJ menubar, click “Image” → “Adjust” → “Threshold. . .”
15. From the Threshold window, adjust threshold until cristae are accurately distinguished from background (Fig 3.1C). Click apply.
16. In the Thresholder window, click “Convert to Mask”.
17. In new window, a binary mask will appear, showing cristae in black and background in white pixels (Fig 3.1D). In the (Fiji Is Just) ImageJ menubar, click “Analyze” → “Analyze Particles...”
18. In the Analyze Particles dialog box, exclude particles that would be below the theoretical area of cristae, *e.g.*, 0.017 $\mu m^2$, and click OK. Note: determining an appropriate theoretical limit of cristae area will depend on cell type and/or the resolution of the microscope used to measure the ultrastructure.
19. A new window showing Regions of Interest (ROIs) will appear, outlining cristae in yellow traces (Fig 3.1E).
20. Next, click on the copy of the original image, made in step 9. Then, in the ROI Manager window, unclick and click the “Show All” checkbox.

This will apply the ROIs generated from the binary mask to the cristae in the original image (Fig 3.1F).

21. Click “Measure” on the ROI Manager window.
22. A new Results window will appear, showing values corresponding to various parameters, such as Area, Mean, Perim. Circ., AR, *etc*. To change these readouts, go to “Set Measurements…” under the “Analyze” tab in the (Fiji Is Just) ImageJ menubar. Note: Area, Circ., and other readouts are typically provided by default in the Set Measurements window. To make sure these measurements are provided, check the “Shape descriptors” box in the Set Measurements window. Copy and paste the data into Microsoft Excel. To obtain cristae density measurements, also segment the mitochondrial network and divide the total number of cristae by the total mitochondrial area ($\mu m^2$) per cell. For each new image/cell, create a separate tab in Excel.

Open new images into the TWS window and apply the classifier to make additional measurements from different samples/assays. Overall, this workflow appeared to be effective at segmenting cristae from living cells. For analysis of SIM images of mitochondrial cristae, we followed this same basic TWS protocol. For technical assistance, including providing macros associated with this study, please contact primary authors.

## Results

### Trainable Weka Segmentation (TWS) is more effective at quantifying cristae in living cells compared to conventional thresholding techniques

To quantify cristae in a high-throughput, semi-automated way, we leveraged the open-source machine-learning TWS plugin, available in Fiji (for more details, see specific steps in Methods section). We first addressed whether our machine-learning protocol was more effective than traditional thresholding at quantifying cristae in living cells. Using the same images from multiple experiments, we compared our novel TWS method to conventional (*i.e.*, manual) thresholding or different thresholding algorithms, which rely on separating high-intensity pixels from low-intensity pixels as a way to distinguish ROIs from background. Compared to images analyzed with our TWS protocol (Fig 3.2D), we found that conventional thresholding was unable to differentiate between cristae less than approximately 200 nm apart from one another, leading to large ROIs appearing to contain multiple structures (Fig 3.2A). We also compared our TWS protocol to more restrictive thresholding algorithms (*e.g.*, MaxEntropy and Shanbhag), available in Fiji (Fig 3.2B–C), and we found that our machine-learning approach was more effective than even restrictive algorithms at segmenting cristae. Using our TWS method to first generate a probability map, we were able to detect significantly more cristae per mitochondrial area (Fig 3.3A, C, and E) as well as significantly smaller cristae (Fig 3.3B and D). We observed that Shanbhag thresholding had cristae areas similar to those measured by our TWS protocol (Fig 3.3F). Inspection of the images indicated that

this was due to the overly restrictive properties of the Shanbhag algorithm, which tended to underestimate the actual cristae areas.

**TWS protocol for segmenting cristae is applicable to multiple cell types and is compatible with different mitochondrial dyes**

After determining that our machine-learning method for quantifying cristae was more effective than conventional thresholding techniques, we addressed whether we could effectively segment the ultrastructure in a variety of cell types. Performing live-cell Airyscan imaging of mitochondrial ultrastructure in HeLa, L6, H1975, and HUH7 cells, we found that our TWS protocol appeared to be effective at segmenting cristae, regardless of the cell type (Fig 3.4A–D, respectively). Intriguingly, we observed that, while there appeared to be no differences in cristae density (Fig 3.4E), cristae in HeLa cells tended to have a smaller cross-sectional area (Fig 3.4F) as well as a larger aspect ratio (Fig 3.4G), compared to the cristae in the other cell types. Next, we determined that it was not only feasible to segment cristae from mitochondria stained with NAO but also with other mitochondrial dyes, such as Rho123 (Fig S3.2A) and MTG (Fig S3.2B).

**TWS protocol can quantify differences in cristae density, area, and shape in cell-culture model of IMM perturbation**

Next, we tested whether our TWS protocol could be utilized to discern defects in mitochondrial ultrastructure associated with pathological changes to mitochondrial membrane integrity. To examine this question, we used H1975 cells deficient in the

phosphatase PTPMT1, which converts phosphatidylglycerolphosphate (PGP) into phosphatidylglycerol (PG), a critical precursor of the signature mitochondrial phospholipid, cardiolipin (Zhang *et al*., 2011). Previous studies have shown by EM that loss of PTPMT1 leads to severe derangement of the IMM, where cristae appear swollen and disorganized (Zhang *et al*., 2011). Compared to control H1975 cells (Fig 3.5A and C), our live-cell imaging of PTPMT1-deficient H1975 cells showed mitochondria with defective ultrastructure (Fig 3.5B and D). Remarkably, our machine-learning method was able to quantify these perturbations, revealing a significant decrease in cristae density (Fig 3.5E), increased cristae area (Fig 3.5F), and decreased cristae aspect ratio (Fig 3.5G).

**TWS protocol is effective at segmenting cristae in live-cell SIM images, highlighting heterogeneity of mitochondrial ultrastructure within the same organelle**

Given the increasing availability of high- and superresolution imaging technologies, we wanted to test whether our TWS protocol could be advantageous for quantifying cristae using other imaging approaches than Airyscan. Staining HeLa cells with MTG, we performed live-cell SIM imaging (Fig 3.6A), and we observed mitochondrial ultrastructure in even finer detail than with Airyscan (Fig 3.6B). We then compared our TWS protocol with a conventional thresholding approach, and determined that, as with Airyscan imaging, machine learning provided significant advantages for quantifying cristae in living cells (Fig S3.3A–D). Interestingly, we observed that our TWS protocol could segment a variety of cristae structures. Remarkably, cristae within the same

mitochondrion often exhibited heterogeneous morphologies, ranging from classical, lamellar structures, to arches, and even to apparently interconnected jigsaw configurations (Videos 3.1–3.2). Moreover, a region of a mitochondrion, appearing to have recently undergone a fusion event, exhibited cristae spanning the interface between the previously separate organelles (Fig 3.6C).

Since mitochondria are dynamic, frequently changing their morphologies, we next sought to determine if our TWS protocol could segment cristae from organelles with markedly different shapes and sizes. Generally, we observed that our machine-learning approach could segment cristae regardless of the gross mitochondrial architecture: for example, we segmented cristae from thin or more distended organelles (Fig 3.7A); ouroboros mitochondria (*i.e.*, organelles exhibiting head-to-tail fusion) (Fig 3.7B); elongated mitochondria with a terminal ouroboros-like structure encompassing a punctate mitochondrion (Fig 3.7C); fragmented mitochondria (Fig 3.7D); and mitochondria of intermediate length (Fig 3.7E). Notably, within these diverse mitochondrial forms, we continued to observe heterogeneity in cristae structure within the same organelle. Having demonstrated our ability to effectively segment a range of cristae shapes from diverse mitochondrial morphologies, we next used our TWS protocol to estimate the average number of cristae in a typical HeLa cell. Analyzing z-stacks of SIM images, we determined that there were 187.2±91 mitochondria and 1,415.6±257 cristae per HeLa cell. The average number of cristae per mitochondrion, therefore, was 9.7±4. Given that the lateral resolution of SIM is approximately 100 nm, it should be noted that cristae

positioned less than 100 nm apart would not be resolved. Thus, these measurements likely underestimate the actual values of cristae per cell as well as cristae per mitochondrion. Using live-cell imaging technologies with higher resolution, in conjunction with our TWS protocol, would probably improve the accuracy of these measurements.

**TWS protocol can quantify acute changes in mitochondrial ultrastructure, resulting from FCCP treatment**

We next determined whether our machine-learning method could be used for measuring changes in mitochondrial ultrastructure, stemming from acute pharmacological perturbation. Treating HeLa cells with FCCP, we imaged them for approximately 1 hr. Consistent with previous studies, we observed time-dependent changes in both gross as well as fine structure (Fig 3.8A). FCCP treatment tended to significantly decrease cristae density (Fig 3.8B) and cristae area (Fig 3.8C), and significantly increased cristae circularity, resulting from an apparent rise in the number of circular cristae membranes (Fig 3.8D). Interestingly, we observed that FCCP treatment did not, on average, decrease the cristae aspect ratio (Fig S3.4B), despite the relatively larger number of circular cristae. This appeared to be due to the concomitant formation of cristae with unusually high aspect ratios, resulting from extreme mitochondrial swelling, associated with the collapse of the proton gradient (Fig S3.4A).

**TWS protocol can measure real-time changes in cristae density, size, and shape**

We next performed time-lapse SIM imaging of mitochondria in HeLa cells stained with MTG to determine whether we could track changes in mitochondrial ultrastructure at high temporal as well as spatial resolution. Imaging mitochondria at approximately 2-s intervals, we observed instances of parallel lamellar cristae fusing into arched structures (Fig 3.9A; Video 3.3), and we measured around 2-fold changes in aspect ratio. We also detected events where a series of lamellar cristae appeared to undergo fission and rapidly remodel into arching structures, running parallel to the long axis of the organelle (Fig 3.9B; Video 3.4). These alterations in shape typically reflected a 2 to 3-fold change in circularity. Ultrastructural remodeling frequently appeared to be associated with fusion and fission events, occurring within relatively short time intervals (*i.e.*, approximately every few seconds), as reflected by dynamic changes in cristae circularity (Fig 3.9C; Video 5).

Given the relatively rapid remodeling of mitochondrial ultrastructure that we observed, we wanted to estimate the dynamic ranges of these parameters in individual mitochondria over a brief period of time. We, therefore, used our TWS protocol to quantify the cristae density, area, circularity, aspect ratio, and total number per mitochondrion at approximately 2-s intervals for roughly 30 s (Fig 3.10A–E). Fig 3.10F shows the mitochondrion corresponding to the green curves in Fig 3.10A–E. In general, we observed that cristae density, size, and shape changed over time within relatively narrow ranges between different organelles within the same cell. We then expressed these time-

dependent alterations as standard deviations per min to summarize their dynamic ranges (Fig 3.10G).

**Real-time quantification of cristae remodeling during mitochondrial fusion and fission highlights the dynamic nature of mitochondrial membranes**

Finally, we examined whether our TWS protocol could quantify cristae during classical examples of mitochondrial dynamics. During mitochondrial fission events, we observed that the site of membrane constriction and fission appeared to consist of inner boundary membranes rather than cristae membranes (Figs 3.11A–C; Videos 3.6–3.8). Since our TWS protocol was trained to recognize cristae, rather than IBM, it is particularly apparent in the TWS cristae probability maps that cristae are not localized to the fission sites.

We next applied our TWS protocol to mitochondria engaging in fusion events. Intriguingly, immediately prior to membrane fusion of the two organelles, we observed finger-like protrusions from the ends of one of the mitochondria (Fig 3.12A and Fig S3.5A and B; Videos 3.9–3.10), which appeared to bridge the membranes of the two organelles. This observation supports recently published models of Mgm1/Opa1–mediating IMM fusion through the formation of highly curved membrane tips (Yan *et al*., 2020). Using live-cell SIM imaging, we observed the formation of such IMM protrusions on one, rather than both, of the fusing mitochondria. This mode of mitochondrial fusion is compatible with a kind of heterotypic membrane fusion, where

the minimum requirement is Opa1 on one side and cardiolipin on the other side of the fusing membranes (Ban *et al*., 2017). Seconds after the membranes from the two mitochondria fused, we observed fusion of previously separate cristae, originating from the different mitochondria (Fig 3.12B). Following cristae fusion, we measured a more than 2-fold decrease in cristae circularity, marking a transition to a more branching architecture.

Altogether, our data show that machine learning provides an effective way to quantify cristae density, size, and shape in living cells, representing a powerful new tool for investigating cristae structure and function in real time.

**Discussion**

Since the discovery of the mitochondrial cristae in the mid 20$^{th}$ century (Palade, 1953), imaging these structures in real time has remained a formidable challenge. Due to the necessity of freezing or fixing samples prior to imaging, EM is incompatible with probing cristae in living cells. Conversely, while conventional optical microscopy has permitted live-cell imaging of mitochondria, the Abbe diffraction limit has wholly obscured the intricacies of the IMM. Recent advancements in high- and superresolution imaging technologies, however, have enabled the visualization of cristae in living cells, leading to an appreciation that cristae are not static structures but appear to possess their own dynamics comparable to the fusion and fission that regulate the plasticity of the larger mitochondrial network (Giacomello *et al*., 2020; Huang X *et al*., 2018; Kondadi *et al*.,

2020; Stephan *et al*., 2019). Furthermore, we recently showed that cristae are functionally independent bioenergetic compartments, capable of preventing the spread of localized damage.

The emerging interest in imaging cristae in living cells calls for novel segmentation methods that will promote accurate and efficient quantification. To address this growing demand, we utilized the open-source machine-learning plugin, TWS, to develop a new approach to segment cristae. Here, we showed that this method is not only more effective than common thresholding techniques available in Fiji, but it is also sufficiently robust to pick out differences in cristae parameters in various cell lines. Furthermore, we demonstrated that, using our method, it is possible to quantify pathological changes in mitochondrial ultrastructure, resulting from genetic or pharmacological perturbations. Using various filtering algorithms, instead of pixel intensities alone, to segment cristae, results in significantly more accurate measurements; moreover, the semi-automation of our TWS protocol makes it feasible to efficiently analyze large numbers of cristae (*e.g.*, 1,000 or more per cell). We also showed that our TWS protocol can be particularly valuable for probing the dynamic nature of the IMM. Our quantifications of real-time changes in cristae density, size, and shape are consistent with recent observations of cristae remodeling in living cells (Huang X *et al*., 2018; Kondadi *et al*., 2020; Stephan *et al*., 2019; Wang C *et al*., 2019). Furthermore, the remarkable heterogeneity in cristae structures that we observed in this study provides further mechanistic insight into the heterogeneity in membrane potential amongst different cristae within the same

mitochondrion (Wolf *et al*., 2019).

It is important to note that, while state-of-the-art high- and superresolution live-cell imaging technologies are providing exciting new windows onto the complex biology of mitochondrial membranes, they remain, to date, unable to supersede EM as a way to map the spatial dimensions of the organelle. For example, the resolution of electron tomography (ET) systems typically ranges from 5 to 20 nm. Therefore, given average ET measurements of crista length and width to be 240 nm and 20 nm, respectively, the cross-sectional area of a crista is 4,800 $nm^2$ (or 0.0048 $\mu m^2$) (Mannella *et al*., 2013). The lateral resolution of SIM (including the GE DeltaVision OMX SR system used in this study) is approximately 100 nm. Our measurements of mean crista area taken from SIM micrographs were 0.0489 $\mu m^2$. This value is about one order of magnitude larger than estimates obtained from ET micrographs, a disparity consistent with an approximately 10-fold difference in the resolution of the two imaging technologies. Therefore, researchers should bear in mind that measurements of cristae area from live-cell, superresolution images are likely to be overestimated by roughly a factor of 10. Given that the mean crista-to-crista distance in HeLa cells, as measured by EM, is roughly 51 to 120 nm (Stephan *et al*., 2019; Wilkens *et al*., 2013), it is likely that our Airyscan and SIM images did not fully capture all of the cristae within a particular frame – especially in cases where cristae were positioned more closely together than could be resolved by the imaging systems employed in this study. Using diffraction-unlimited nanoscopy (*e.g.*, STED) to image cristae in living cells will likely decrease, if not entirely remove, such

disparities. Incidentally, the problem of fully segmenting cristae within a mitochondrion is comparable to the difficulty of completely segmenting mitochondria within a cell, which remains a significant challenge, despite the larger dimensions of the organelles.

Although our TWS protocol for quantifying cristae is necessarily constrained by the resolving power of the microscopes used to image the IMM, it remains particularly useful for obtaining relative measures of the effects of cristae perturbation, as we demonstrated in our genetic and pharmacological models. The actual dimensions of the cristae parameters may be over- or underestimated, according the specific measurement in question, but tracking relative changes can nevertheless yield valuable information about the effects of potential modulators of cristae density, size, and shape.

Overall, in this study, we present a novel approach to further illuminate the dynamic nature of mitochondrial membranes by quantifying changes in cristae density and architecture in real time. Future studies examining the relationship between cristae structure and function will likely benefit from leveraging a machine-learning segmentation protocol like the one we outlined here.

**Acknowledgements**

We thank Drs. Martin Picard, Barbara Corkey, David Nicholls, Gulcin Pekkurnaz, Gilad Twig, Ophry Pines, Victor Darley-Usmar, György Hajnóczky, Fernando Abdulkader, and Daniel Dagan for fruitful discussions. We also thank Drs. Mingqi Han and Sean T.

Bailey for help with reagents and cell lines. OSS is funded by NIH-NIDDK 5-RO1DK099618-02. ML is funded by UCLA Department of Medicine Chair commitment and UCSD/UCLA Diabetes Research Center grant, NIH P30 DK063491. DBS is funded by an NIH/NCI R01 CA208642-01. NWH and DSW are supported by R01 EY027442 and R01 EY013408 (to David S. Williams). DSW also receives funding from P30 EY000331 (to David S. Williams), and NWH is additionally supported by UCLA Postdocs Longitudinal Investment in Faculty Training (UPLIFT) K12GM106996 (to Michael F. Carey).

**Author contributions**

MS and DMW designed the study, made the figures, and wrote the manuscript. MS, DMW, and NWH performed the imaging. MS and DMW performed the data/image analysis. AMVDB, DSW, and DBS contributed to the study design and provided cell lines, instrumentation, and/or reagents. ML and OSS supervised the study.

**Conflict of interest**

The authors declare that they have no conflicts of interest.

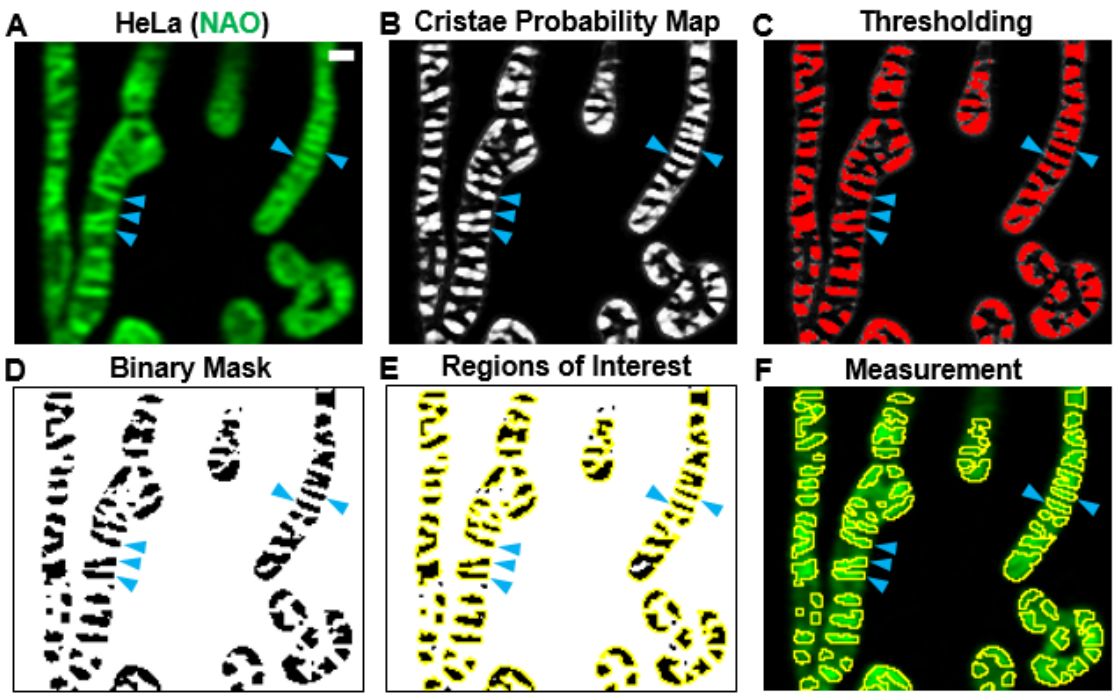


**Figure 3.1. Machine-learning approach using Trainable Weka Segmentation (TWS) can segment mitochondrial cristae in living cells.**

Approach for quantifying live-cell imaging of cristae using the LSM880 with Airyscan.

**A.** Image of cristae (blue arrowheads) in HeLa cell stained with 10-*N*-nonyl acridine orange (NAO). Scale bar = 500 nm.

**B.** Cristae probability map depicting areas likely to be cristae (white pixels) vs. background (black pixels). Blue arrowheads denote cristae.

**C.** Thresholding of the cristae probability map in **B**. Selected cristae are shown in red (denoted by blue arrowheads).

**D.** Binary mask resulting from application of thresholding step in **C**. Blue arrowheads denote cristae (black pixels).

**E.** Regions of interest (ROIs) marked by yellow borders around cristae (black pixels). Blue arrowheads denote cristae.

**F.** Superimposition of ROIs onto original image in **A**. Subsequent measurement yields data relating to various parameters, such as cristae density, area, and shape.

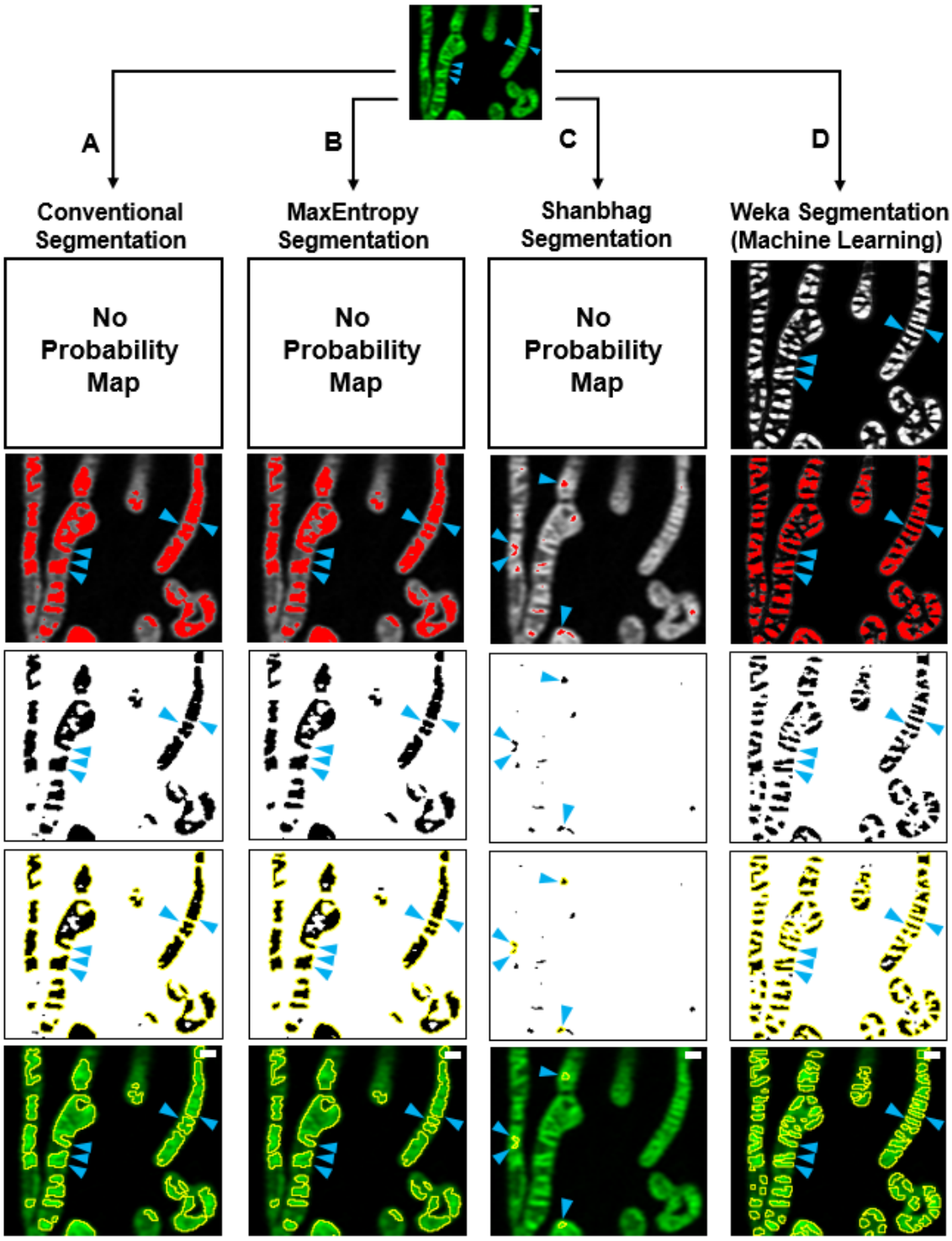


**Figure 3.2. TWS protocol more effectively segments mitochondrial cristae from living cells compared to various thresholding standards.**

**A-D.** Step-wise comparison of different segmentation workflows: Conventional (manual) **(A)**; MaxEntropy **(B)**; Shanbhag **(C)**; and TWS **(D)**. Note that without a probability map, Conventional, MaxEntropy, and Shanbhag thresholding, which depend exclusively on pixel intensities, cannot effectively segment cristae. Blue arrowheads denote successful segmentation of cristae (column **D**) vs. ineffective segmentation (columns **A-C**). Scale bars = 500 nm.

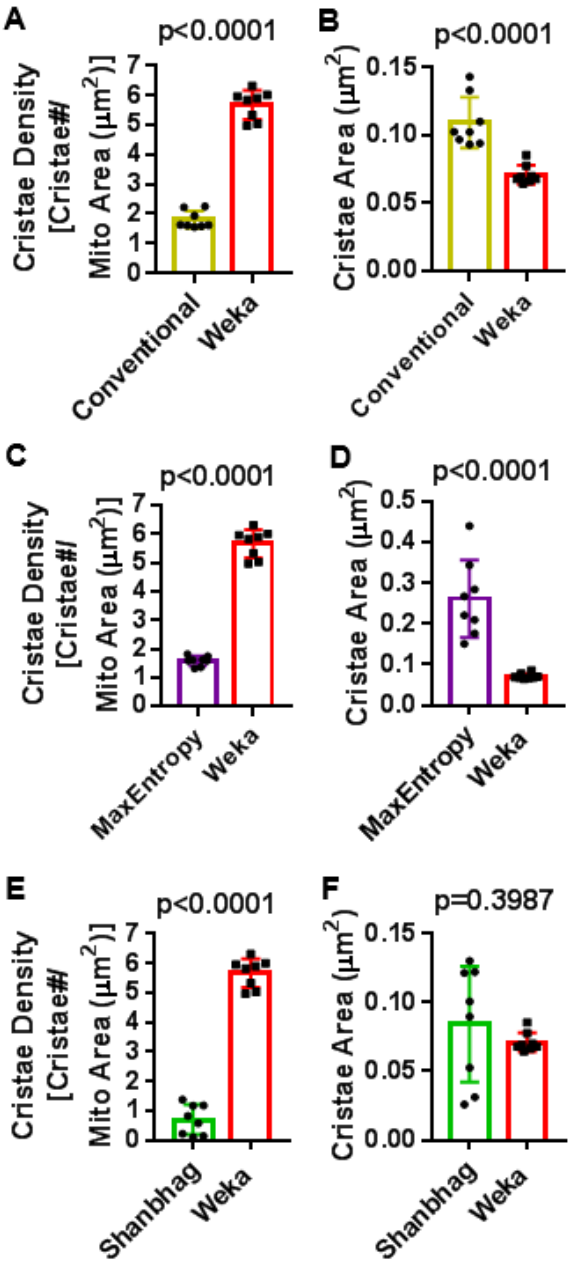


**Figure 3.3. TWS protocol offers significant advantages over standard thresholding techniques for the quantification of cristae in living cells.**

Quantification of cristae parameters using TWS protocol vs. standard thresholding.

**A, C, E.** Quantification of cristae density (cristae#/$\mu m^2$) in HeLa cells stained with NAO. Note: TWS is significantly more effective at measuring cristae density compared to Conventional, MaxEntropy, and Shanbhag segmentation methods, respectively. N = 8 independent experiments.

**B, D, F.** Quantification of cristae area ($\mu m^2$) in HeLa cells stained with NAO. Note: Conventional and MaxEntropy segmentation are unable to segment cristae effectively, resulting in significantly higher values in cross-sectional area, compared to Weka segmentation. Conversely, Shanbhag segmentation shows average cristae areas similar to those of Weka segmentation, but this results from Shanbhag being overly restrictive, subsequently underestimating or entirely missing a large proportion of cristae structures (see Fig. 3.2). N = 8 independent experiments.

Data information: Data are presented as mean ± SD. P values are shown in panels (Student's t-tests).

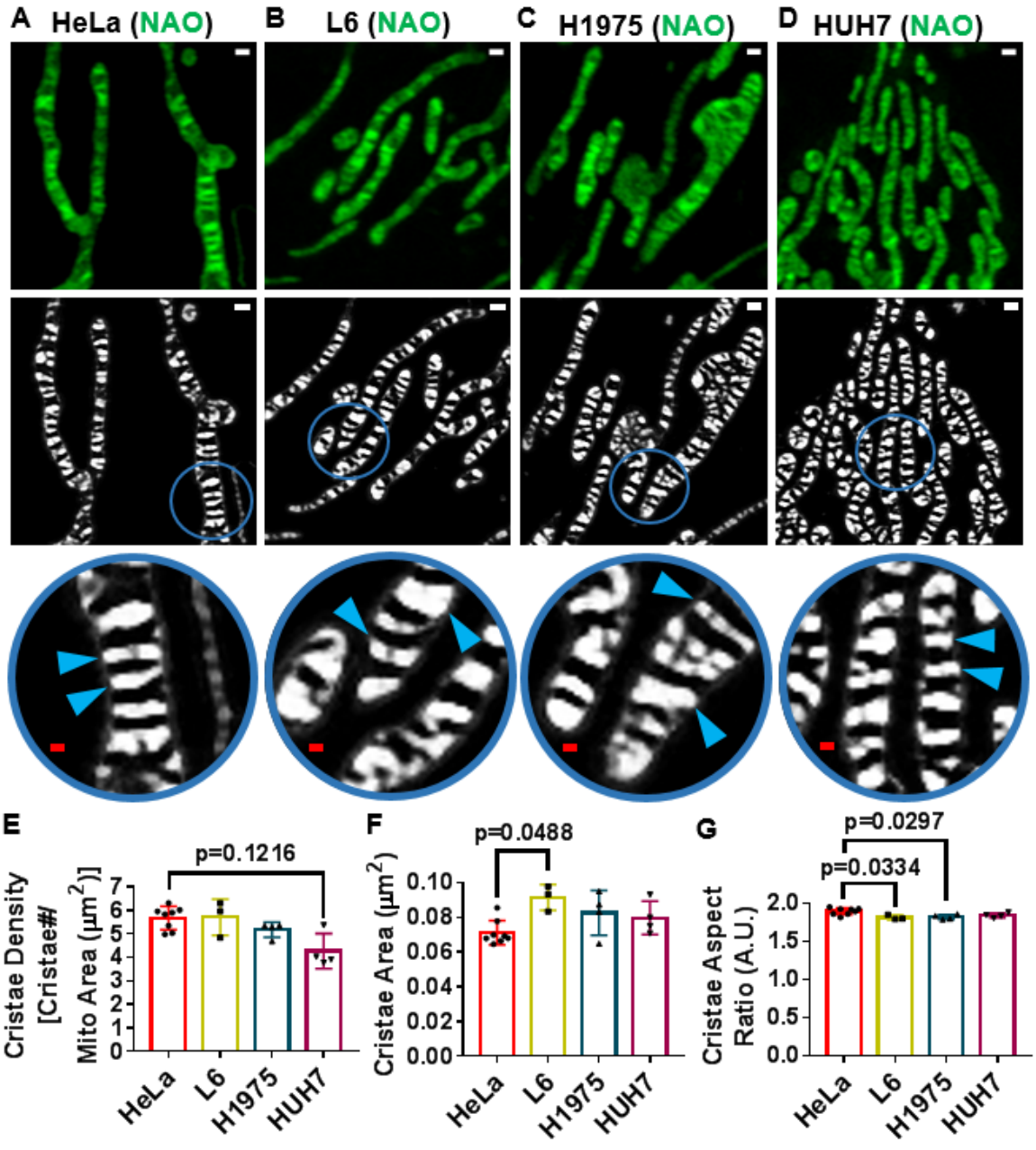


**Figure 3.4. TWS protocol enables segmentation of cristae in a variety of cell types.**

**A-D.** Live-cell Airyscan images of HeLa **(A)**, L6 **(B)**, H1975 **(C)**, and HUH7 **(D)** mitochondria, stained with NAO. Note that top row shows original images (scale bars = 500 nm). Bottom row, including circular, zoomed-in regions, show probability maps of

cristae in respective cell types (red scale bars = 200 nm). Blue arrowheads denote cristae. **E.** Quantification of cristae density between HeLa, L6, H1975, and HUH7 cells, stained with NAO. $N \geq 3$ independent experiments. **F.** Quantification of cristae area between HeLa, L6, H1975, and HUH7 cells, stained with NAO. $N \geq 3$ independent experiments. **G.** Quantification of cristae aspect ratio between HeLa, L6, H1975, and HUH7 cells, stained with NAO. $N \geq 3$ independent experiments. Note that HeLa cells tend to have lower cross-sectional area of cristae together with increased aspect ratio.

Data information: Data are presented as mean ± SD. P values are shown in panels (ANOVA).

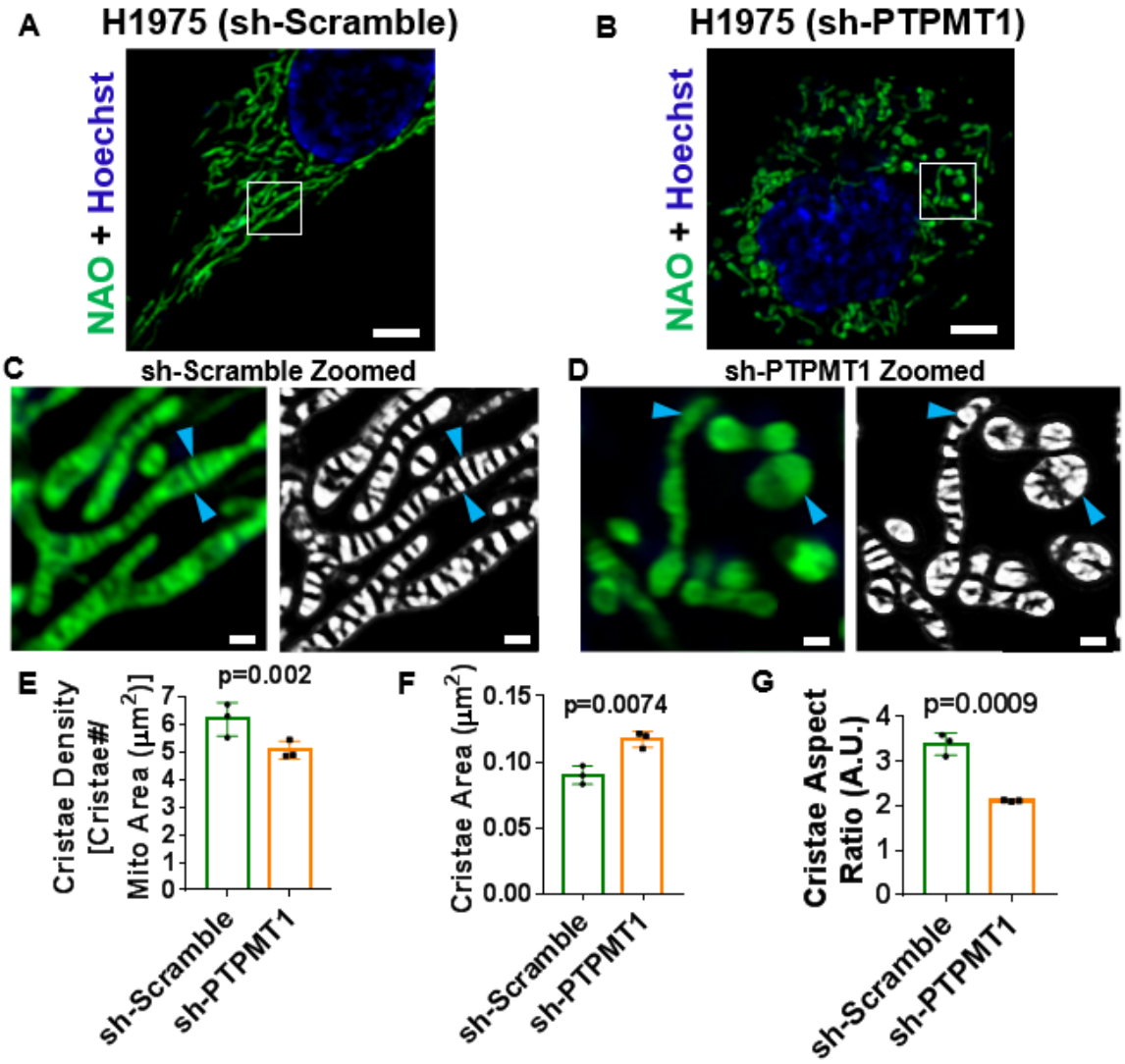


**Figure 3.5. TWS protocol is sufficiently sensitive to detect differences in cristae density, area, and shape in cardiolipin-deficient (sh-PTPMT1) H1975 cells, a model of IMM dysregulation.**

**A.** Image of sh-Scramble H1975 cell, stained with NAO and Hoechst. Scale bar = 5 µm.

**B.** Image of sh-PTPMT1 H1975 cell, stained with NAO and Hoechst. Scale bar = 5 µm.

**C.** Zoomed-in region of **A**, showing normal lamellar cristae (blue arrowheads) in original image (left) compared to cristae probability map (right). Scale bars = 500 nm.

**D.** Zoomed-in region of **B**, showing deranged cristae (blue arrowheads) in original image (left) compared to cristae probability map (right). Scale bars = 500 nm. Note that these images appear to corroborate previously published EM data, showing loss of PTPMT1 results in swelling and disruption of cristae structure.

**E.** Quantification of cristae density between sh-Scramble and sh-PTPMT1 in H1975 cells, stained with NAO. N = 3 independent experiments.

**F.** Quantification of cristae area between sh-Scramble and sh-PTPMT1 in H1975 cells, stained with NAO. N = 3 independent experiments.

**G.** Quantification of cristae aspect ratio between sh-Scramble and sh-PTPMT1 in H1975 cells, stained with NAO. N = 3 independent experiments.

Data information: Data are presented as mean ± SD. P values are shown in panels (Student's t-tests).

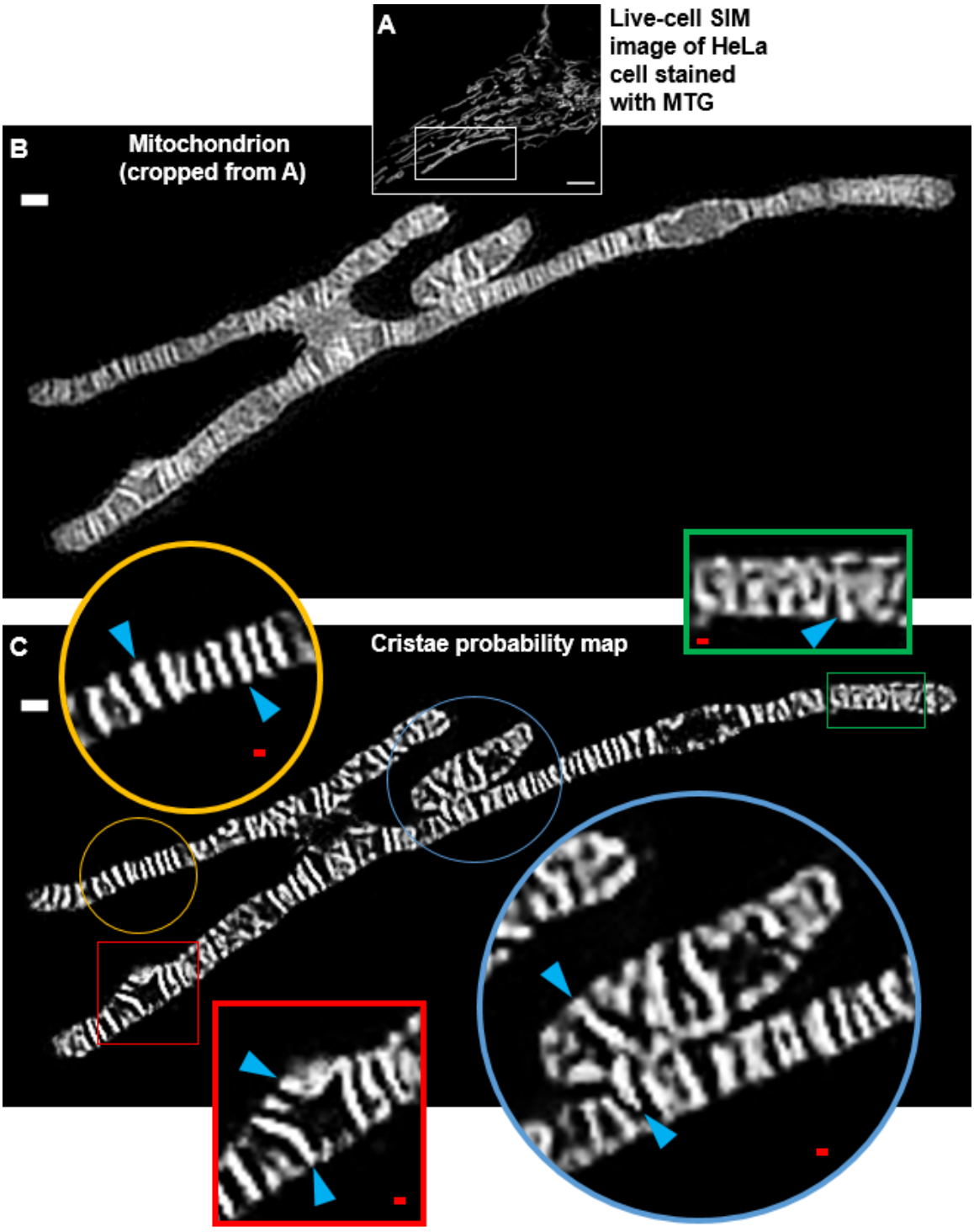


**Figure 3.6. TWS is effective at segmenting cristae in live-cell images obtained with structured illumination microscopy (SIM), highlighting ultrastructural**

**heterogeneity within the same mitochondrion.**

**A.** Live-cell SIM image of HeLa cell stained with MTG. Scale bar = 5 μm.

**B.** Mitochondrion cropped from **A**, showing fine structure of mitochondrion. Scale bar = 500 nm. Note that the different mitochondrial regions appear to encompass a single fused structure.

**C.** Cristae probability map of cropped SIM image from **B**. White scale bar = 500 nm. Note that the zoomed-in regions show heterogeneous cristae architecture (blue arrowheads) within the same organelle: the gold circle highlights a region of lamellar cristae; the red square shows a variety of arched cristae, running either parallel or perpendicular to the long axis of the organelle; the green rectangle shows a jigsaw configuration; and the blue circle shows cristae spanning adjacent mitochondrial structures. Red scale bars = 100 nm.

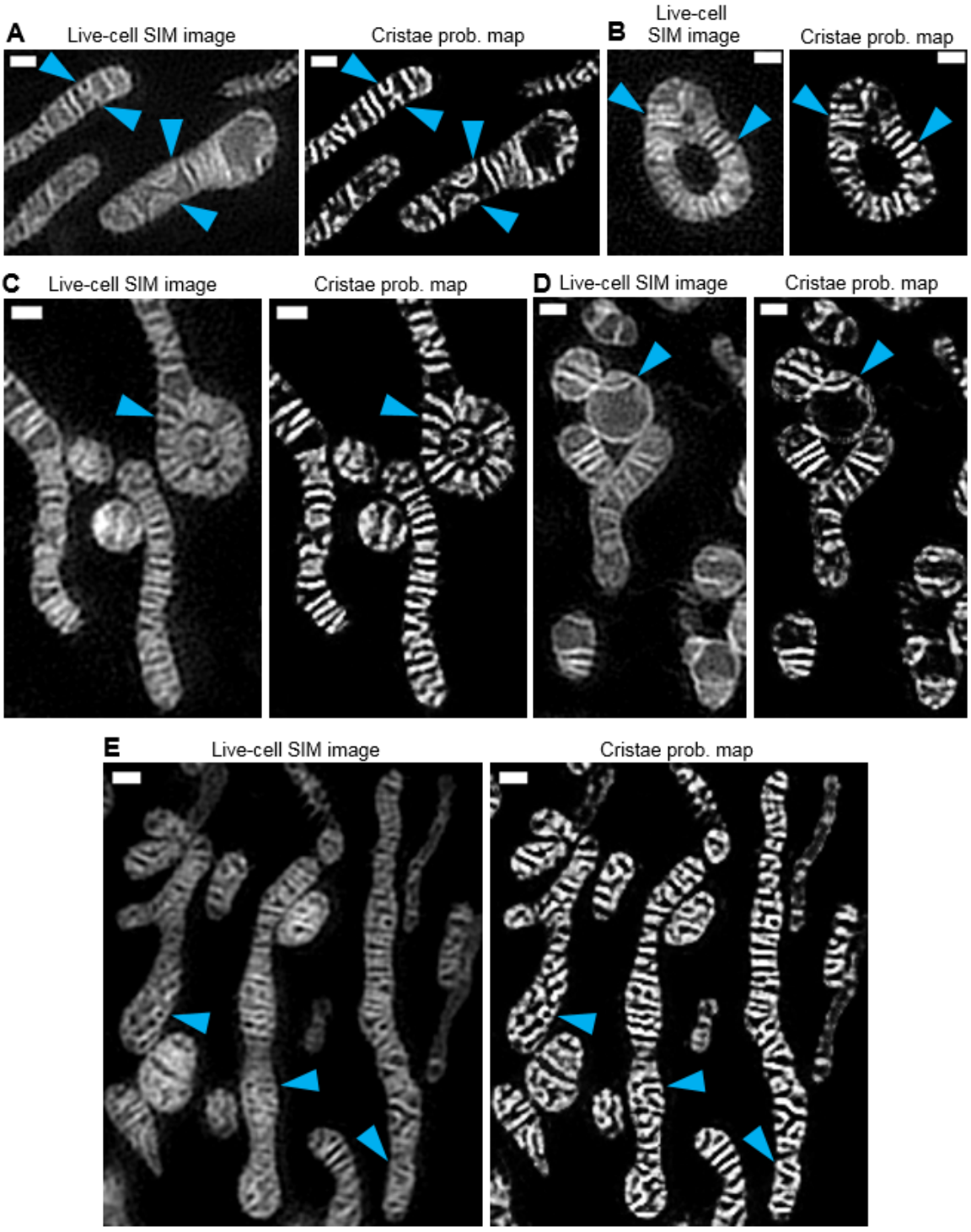


**Figure 3.7. TWS method can segment different cristae structures found in a range of mitochondrial morphologies.**

Live-cell SIM images of HeLa cells stained with MTG (left) and cristae probability maps (right) showing various mitochondria with differing cristae structures.

**A.** Thin and distended mitochondria, showing relatively small and large arched cristae, respectively (blue arrowheads). Scale bars = 500 nm. N = 3 independent experiments.

**B.** Ouroboros mitochondrion, showing cristae radiating from central gap (blue arrowheads). Scale bars = 500 nm. N = 3 independent experiments.

**C.** Elongated mitochondrion with ouroboros-like end, containing cristae radiating from center (blue arrowhead); note the spherical mitochondrion filling the gap within this ouroboros-like structure. Scale bars = 500 nm. N = 3 independent experiments.

**D.** Fragmented mitochondria, showing arched cristae structures (blue arrowhead). Scale bars = 500 nm. N = 3 independent experiments.

**E.** Mitochondria of intermediate length, containing various netlike and/or curving cristae (blue arrowheads). Scale bars = 500 nm. N = 3 independent experiments.

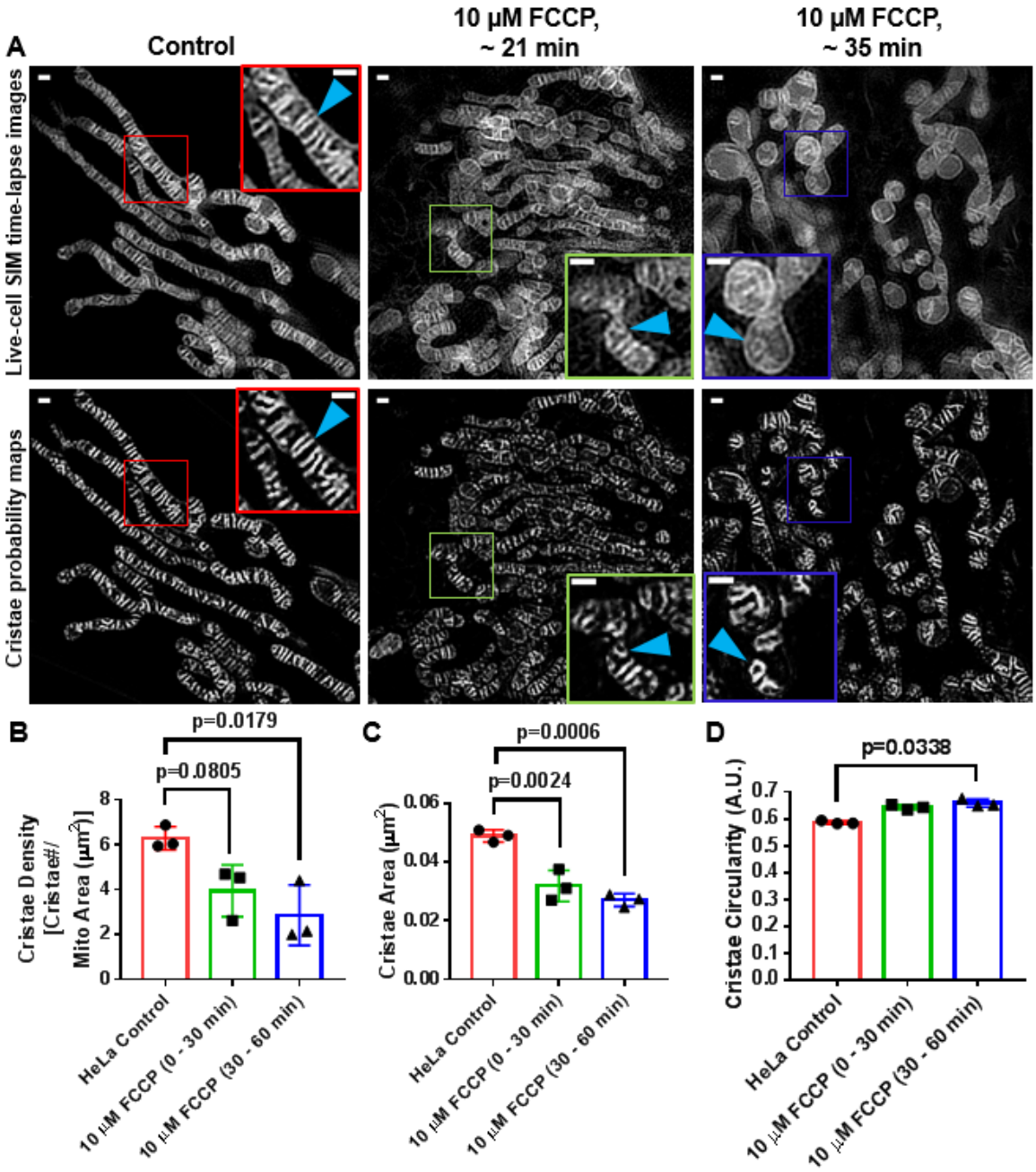


**Figure 3.8. TWS protocol can capture changes in cristae density, area, and shape following acute treatment with FCCP.**

**A.** Live-cell SIM images of HeLa cells stained with MTG (top row) together with cristae probability maps (bottom row). Note that the left-most column shows a representative

image of control, whereas the center and right-most columns show representative images of cells treated with 10 μM FCCP between 0-30 min and 30-60 min, respectively. Scale bars = 500 nm. N = 3 independent experiments.

**B-D.** Quantification of SIM images from **A**, showing a time-dependent decrease in cristae density **(B)** and cristae area **(C)**, as well as an increase in cristae circularity **(D)** as a result of FCCP treatment. N = 3 independent experiments.

Data information: Data are presented as mean ± SD. P values are shown in panels (ANOVA).

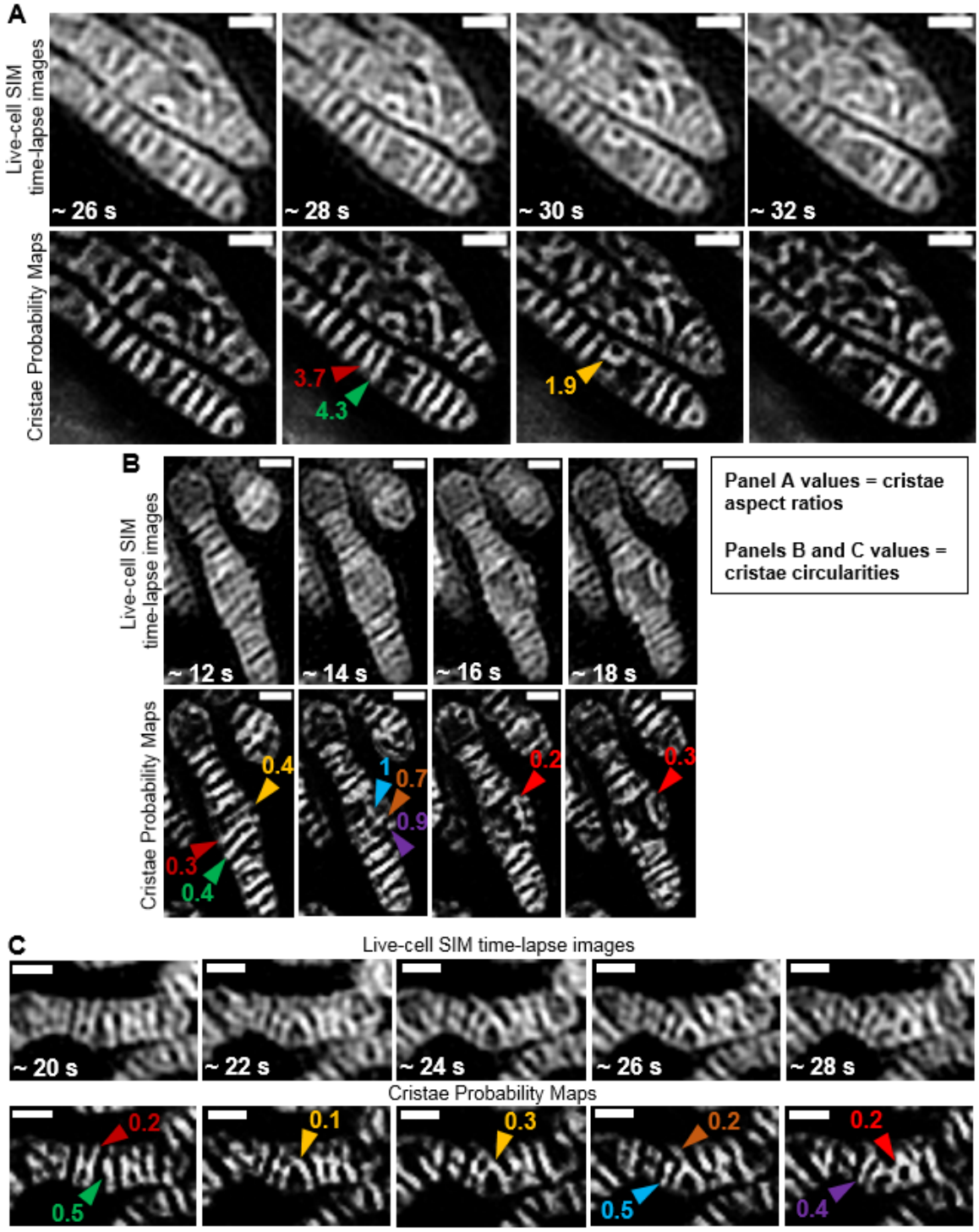


**Figure 3.9. TWS protocol can quantify real-time cristae remodeling within the same mitochondrion.**

Zoomed-in, time-lapse SIM images of HeLa cells stained with MTG (top rows) and cristae probability maps (bottom rows).

**A.** Example of quantification of shape changes before and after cristae fusion event. Note parallel cristae (red and green arrowheads) at ~ 28 s are separate structures with aspect ratios of 3.7 and 4.3, respectively; but, after fusing into an arched structure (gold arrowhead), the aspect ratio of the resulting crista is altered to 1.9. Scale bars = 500 nm.

**B.** Example of quantification of shape change before and after cristae fission events. Note 3 parallel cristae (gold, red, and green arrowheads) at ~ 12 s have a circularity of 0.4, 0.3, and 0.4, respectively. After fission of these cristae at ~ 14 s, however, membrane fragments (blue, brown, and purple arrowheads) have a circularity of 1, 0.7, and 0.9, respectively. At ~ 16 and 18 s, these fragments appear to fuse into a branched and arching structure (red arrowheads), respectively, with a circularity of 0.2 and 0.3. Scale bars = 500 nm.

**C.** Example of quantification of multiple, consecutive cristae remodeling events. Note that separate cristae (red and green arrowheads) at ~ 20 s have a circularity of 0.2 and 0.5, respectively. At ~ 22-24 s, these cristae appear to fuse (gold arrowheads), showing alterations in circularity to 0.1 and 0.3, at respective time-points. This structure, at ~26 s, then appears to divide into a smaller crista (blue arrowhead) with a circularity of 0.5 and a larger forked crista (brown arrowhead) with a circularity of 0.2. At ~ 28 s, the smaller crista appears to have fused with the upper region of the previously forked crista, resulting a new structure (purple arrowhead) with a circularity of 0.4; whereas the lower region of the previously forked crista appears to have fused with the crista to the right,

generating a more complex network (red arrowhead) with a circularity of 0.2. Scale bars = 500 nm.

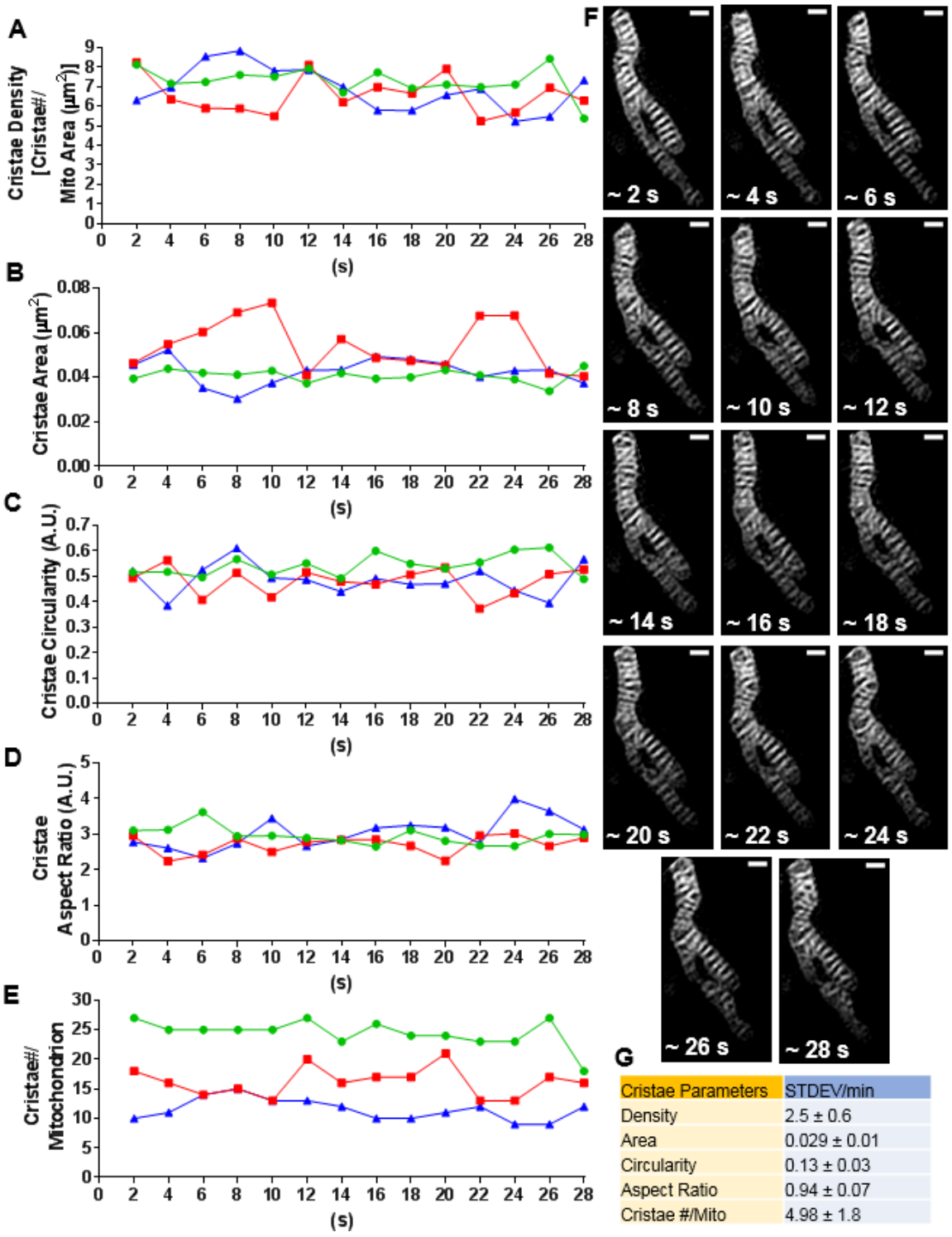


**Figure 3.10. Quantification of dynamic ranges of cristae parameters within individual mitochondria inside the same HeLa cell.**

**A-E.** Measurement of time-dependent changes in cristae density **(A)**, cristae area **(B)**, cristae circularity **(C)**, cristae aspect ratio **(D)**, and cristae number per mitochondrion **(E)**. Note that each colored line (red, green, and blue) represents time-dependent changes in cristae parameters within a whole and separate mitochondrion inside the same cell. **F.** Representative mitochondrion from **A-E**. Scale bars = 500 nm. Note that the different values associated with this mitochondrion are displayed by the green curves. **G.** Table showing standard deviations in cristae density, area, circularity, aspect ratio, and cristae number per mitochondrion per min. Note that the standard deviations in these cristae parameters reflect typical, time-dependent changes in cristae density and architecture. N = 3 independent experiments. Values are shown with associated SDs.

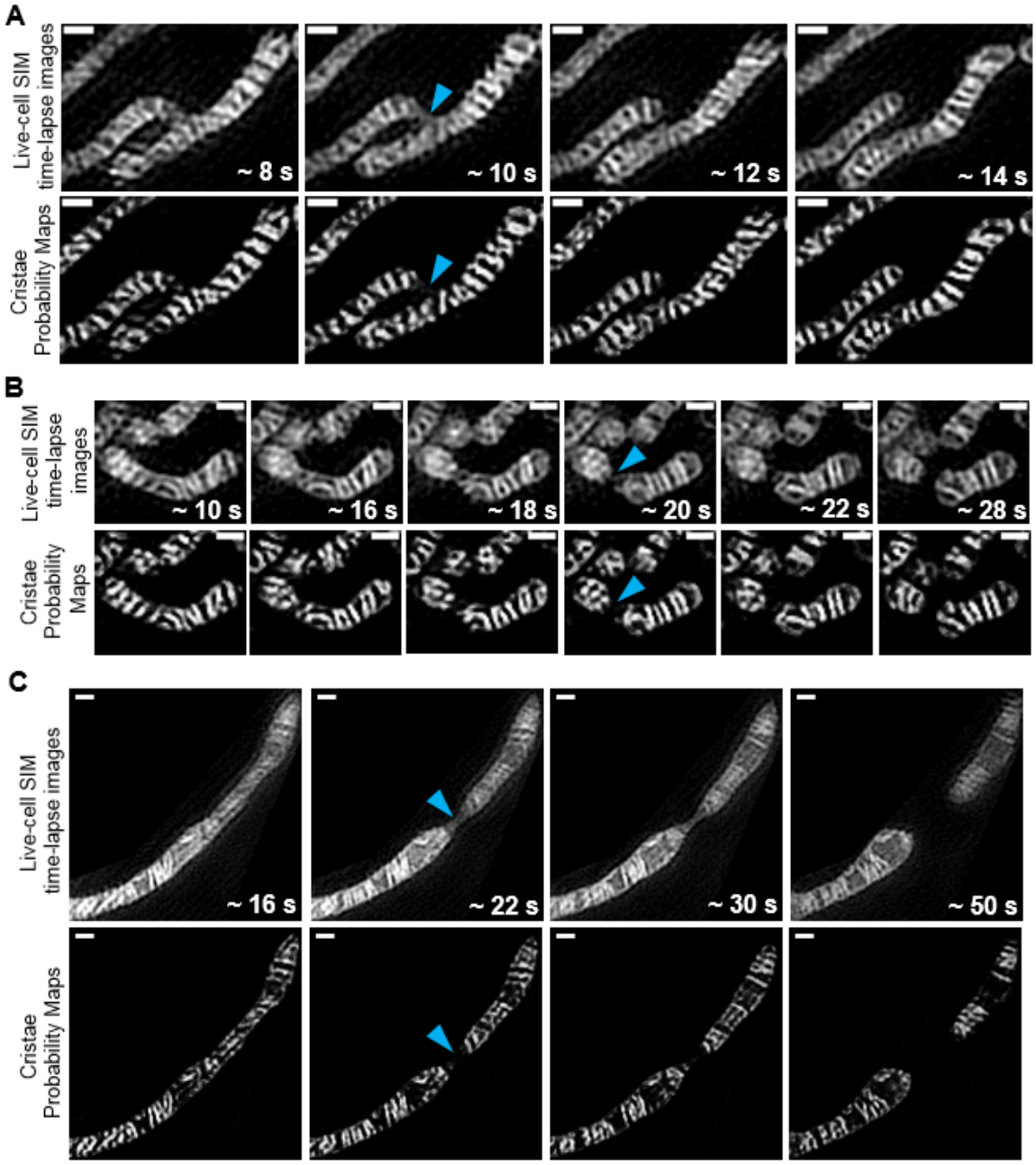


**Figure 3.11. TWS protocol shows fission sites containing decreased cristae density.**

**A-C.** Representative time-lapse SIM images of HeLa cells stained with MTG (top rows) with cristae probability maps (bottom rows), showing effective segmentation of cristae during mitochondrial fission events. Note the narrowing of the inner boundary

membranes (blue arrowheads) prior to mitochondrial fission into two daughter mitochondria. Also note the decreased cristae density at fission sites. Scale bars = 500 nm. N = 3 independent experiments.

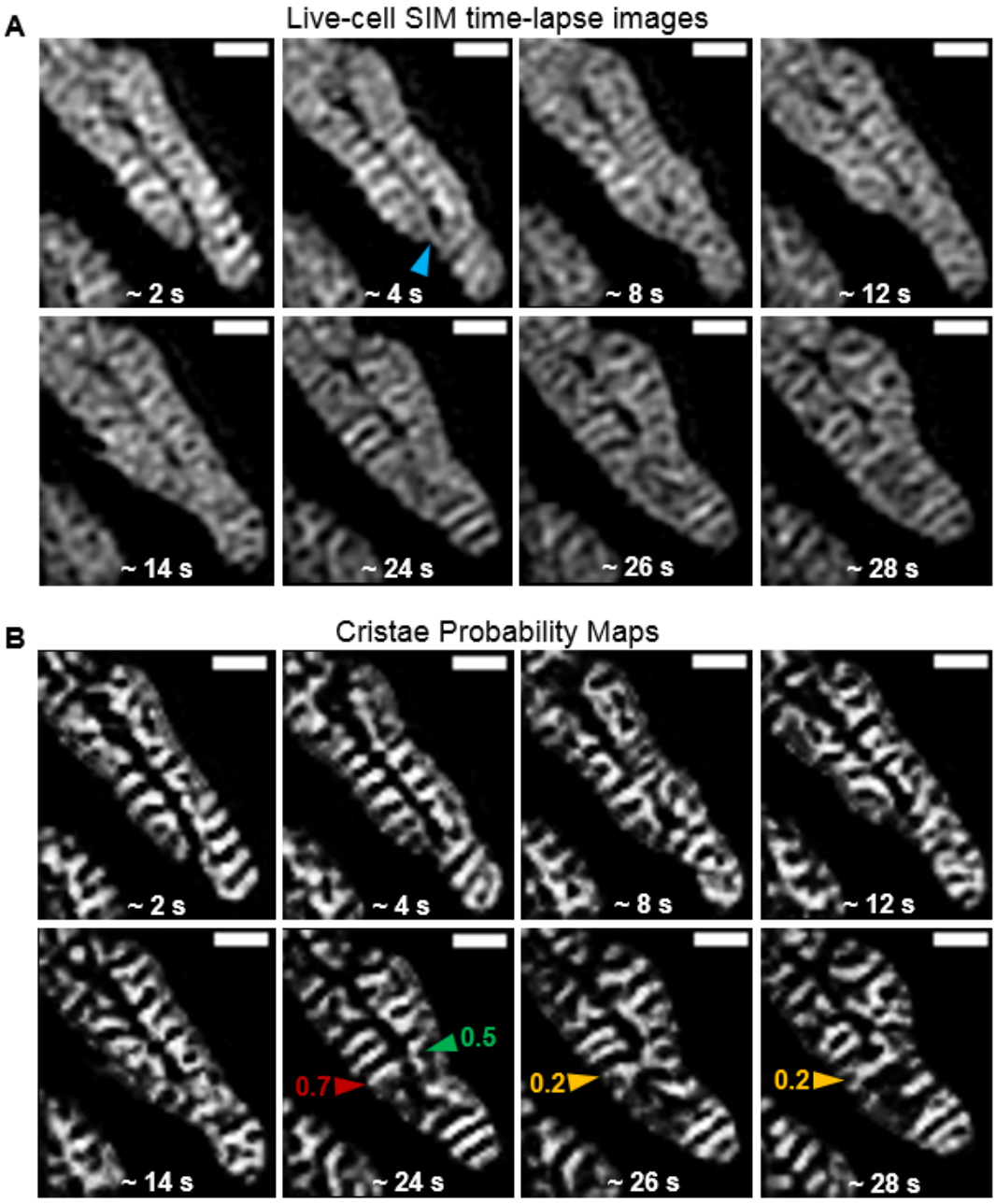


**Figure 3.12. TWS protocol can quantify cristae remodeling during mitochondrial fusion events.**

**A.** Representative time-lapse SIM images of HeLa cell stained with MTG. Scale bars = 500 nm. Note at ~ 4 s, a finger-like region of IMM extends from the tip of the

mitochondrion on the left (blue arrowhead), prior to fusion with mitochondrion on the right in the following frame.

**B.** Cristae probability maps of time-lapse images from **A**. Scale bars = 500 nm. Note at ~ 24 s, the separate cristae (red and green arrowheads) of the adjoining mitochondria have circularities of 0.7 and 0.5, respectively; however, after fusion in the following frame, the crista shows a circularity of 0.2, marking a transition from a less to more branching structure.

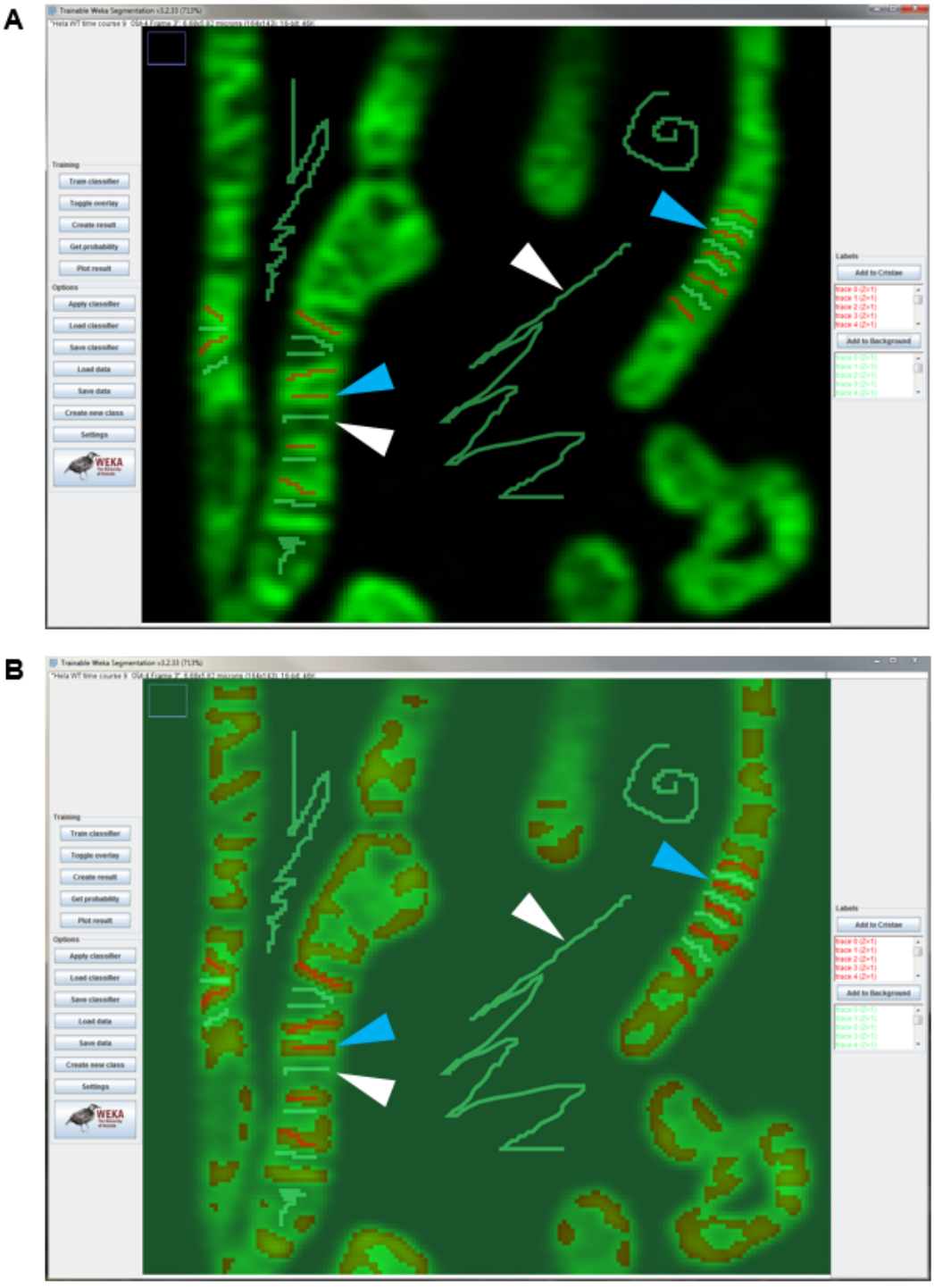


**Supplementary Figure 3.1. Images of Trainable Weka Segmentation (TWS) window during training of classifier.**

**A.** TWS window showing training of classifier on two classes of objects, “Cristae” and “Background”. Note that the traces marking cristae are red lines (denoted by blue arrowheads); and the traces marking background are green lines (denoted by white arrowheads).

**B.** Overlay of trained classifier, showing early step in training process, where cristae are marked as reddish brown areas (blue arrowheads) and background is marked as greenish areas (white arrowheads).

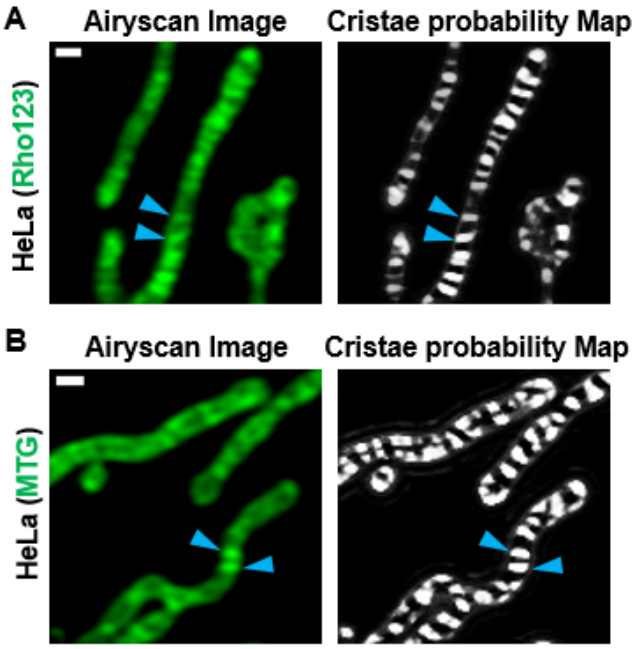


**Supplementary Figure 3.2. Live-cell images and probability maps of cristae using different mitochondrial dyes.**

**A.** Top row: Live-cell Airyscan image of HeLa cell stained with Rho123, showing original image (left) and cristae probability map (right). Blue arrowheads denote cristae. Scale bar = 500 nm.

**B.** Bottom row: Live-cell Airyscan image of HeLa cell stained with MTG, showing original image (left) and cristae probability map (right). Blue arrowheads denote cristae. Scale bar = 500 nm.

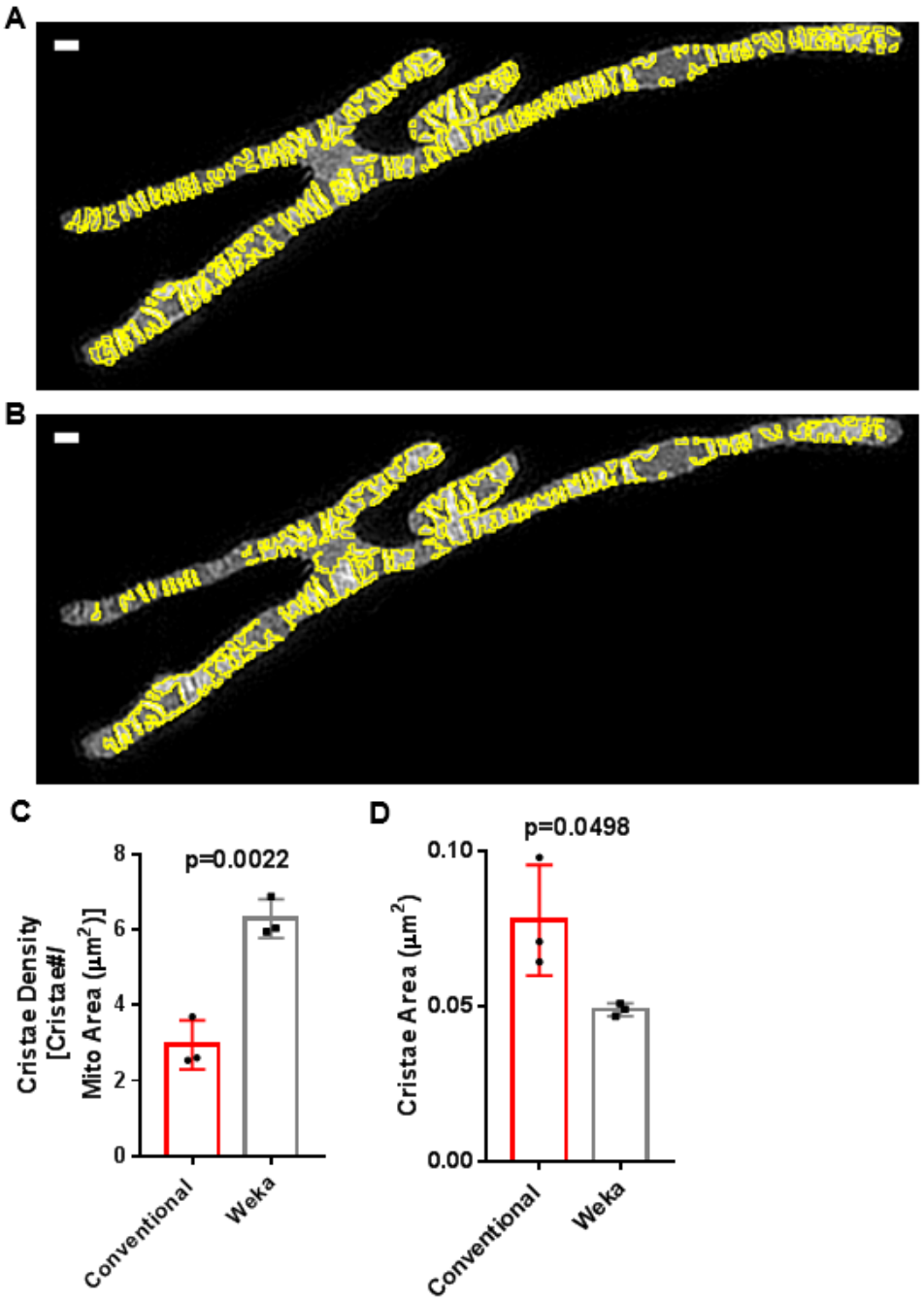


**Supplementary Figure 3.3. TWS protocol is more effective than conventional thresholding at segmenting cristae from SIM images.**

**A.** SIM image of mitochondrion cropped from HeLa cell stained with MTG. Yellow outlines show segmented cristae ROIs using TWS protocol. Scale bar = 500 nm.

**B.** SIM image of mitochondrion cropped from HeLa cell stained with MTG. Yellow outlines show segmented cristae ROIs using conventional thresholding. Scale bar = 500 nm. Note that ROIs produced from conventional thresholding are less effective at segmenting cristae, having more merged structures, which overestimate the area and underestimate the density of cristae.

**C.** Quantification of cristae density from live-cell SIM images in **A** and **B**, showing more effective segmentation via TWS protocol. N = 3 independent experiments.

**D.** Quantification of cristae area from live-cell SIM images in **A** and **B**, showing more effective segmentation via TWS protocol. N = 3 independent experiments.

Data information: Data are presented as mean ± SD. P values are shown in panels (Student's t-tests).

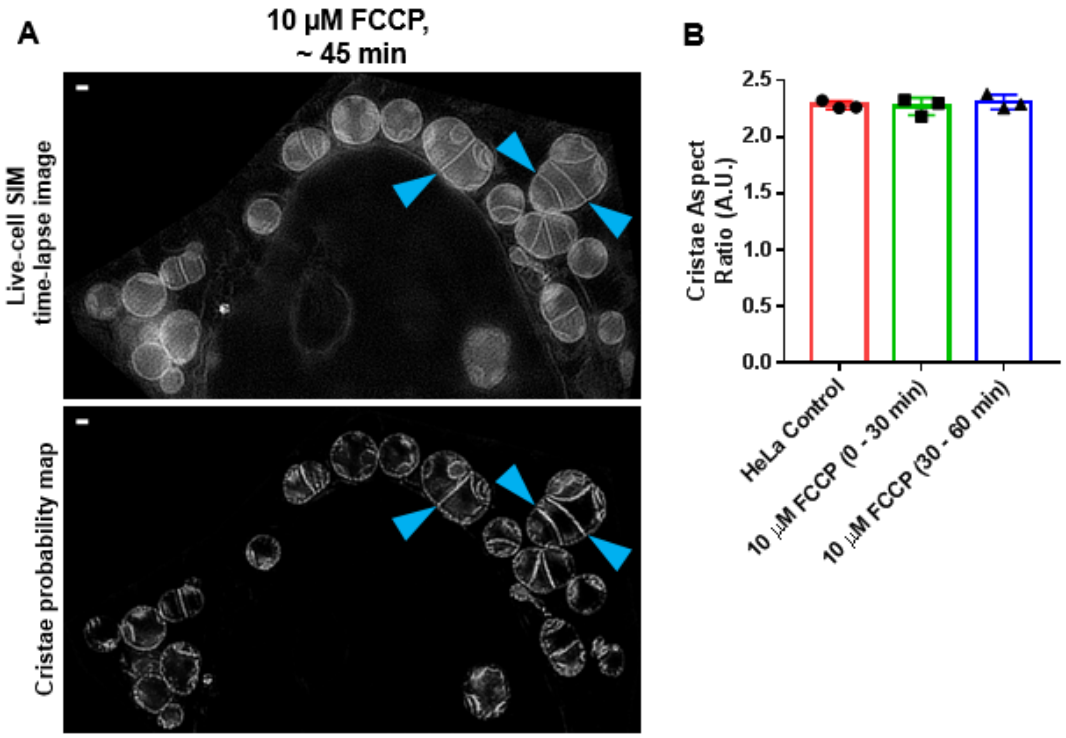


**Supplementary Figure 3.4. FCCP treatment can result in formation of markedly elongated cristae structures.**

**A.** Live-cell SIM image (upper panel) of HeLa cell treated with 10 µM FCCP can result in mitochondrial swelling, accompanied by elongation of cristae (blue arrowheads). Lower panel shows cristae probability map. Scale bar = 500 nm.

**B.** Quantification of cristae aspect ratio, showing no difference between control and FCCP-treated conditions. Note that elongated cristae structures in FCCP-treated cells were accompanied by smaller, circular cristae structures, in other cells; on average, these divergent morphologies resulted in similar values as control. N = 3 independent experiments.

Data information: Data are presented as mean ± SD. There were no significant differences between conditions (ANOVA).

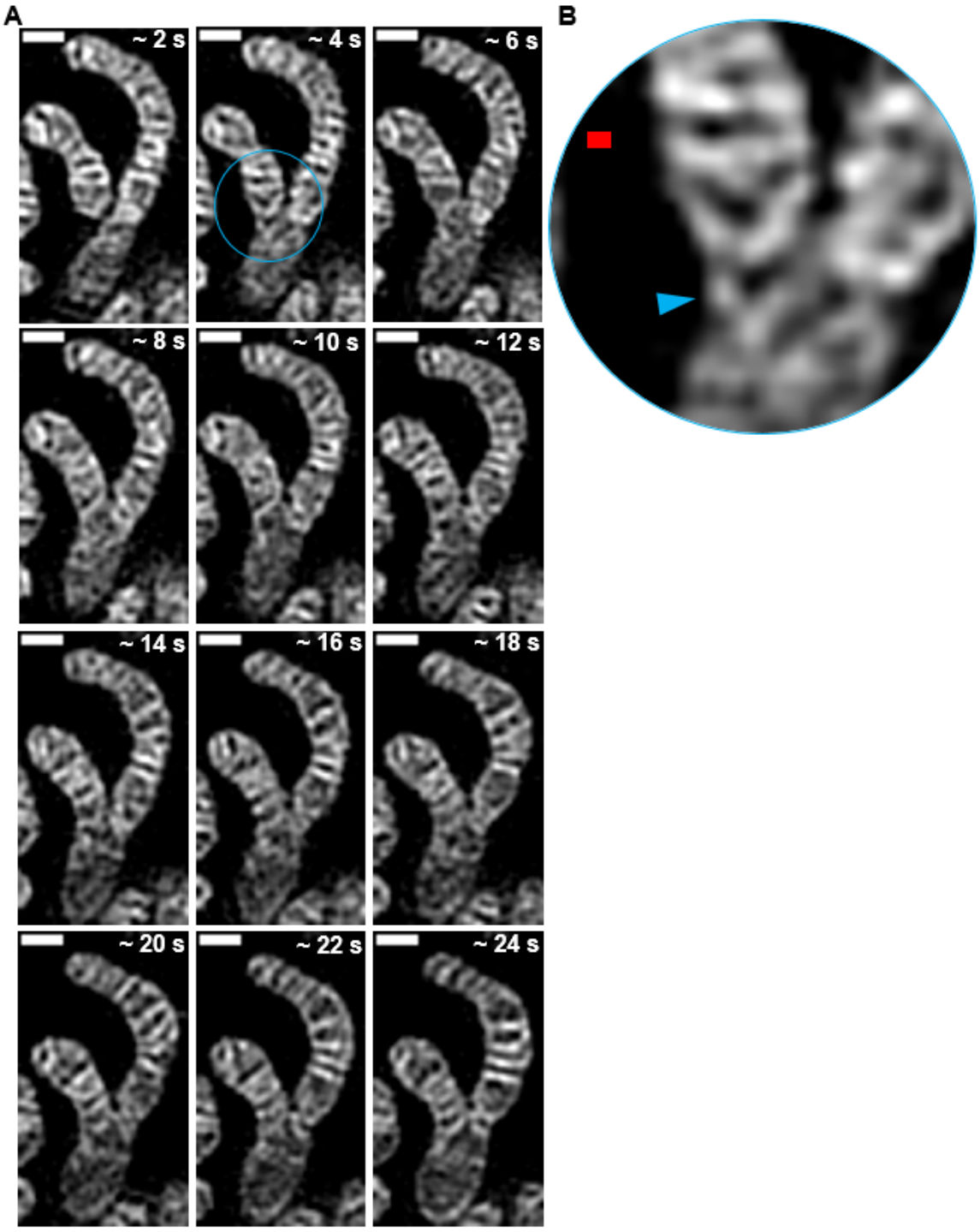


**Supplementary Figure 3.5. Prior to mitochondrial fusion, finger-like extension of IMM appears to bridge membranes of separate organelles.**

**A.** Time-lapse SIM images of mitochondria from HeLa cell stained with MTG. Note that, at ~ 4 s, the smaller mitochondrion on the left, appears to extend a finger-like projection toward the mitochondrion on the right (blue circle). At subsequent time points, the membranes of the two mitochondria merge into a single network. Scale bars = 500 nm.

**B.** Zoomed-in region of finger-like extension (blue arrowhead) from **A**. Red scale bar = 100 nm.

**Legends for Videos:**

**Video3.1**. SIM z-stack of mitochondrion cropped from HeLa cell stained with MTG. Note heterogeneity of cristae density and architecture throughout the fused mitochondrial structure.

**Video3.2**. Cristae probability map of SIM z-stack of mitochondrion from Video1.

**Video3.3.** SIM time-lapse video showing fusion of two parallel lamellar cristae forming an arched structure.

**Video3.4.** SIM time-lapse video showing fission and subsequent fusion of three lamellar cristae within a single mitochondrion.

**Video3.5.** SIM time-lapse video of multiple cristae remodeling events within a single mitochondrion.

**Video3.6.** SIM time-lapse video showing lower cristae density at site of mitochondrial fission.

**Video3.7.** SIM time-lapse video showing lower cristae density at site of mitochondrial fission.

**Video3.8.** SIM time-lapse video showing lower cristae density at site of mitochondrial fission. Note that inner boundary membranes, rather than cristae membranes, are localized at fission site immediately prior to mitochondrial fission.

**Video3.9.** SIM time-lapse video showing mitochondrial fusion event, where cristae from previously separate mitochondria merge into a single crista, exhibiting different architectural characteristics. Note that prior to fusion, mitochondrion on the left forms a finger-like protrusion, appearing to bridge the membranes of the two mitochondria.

**Video3.10.** SIM time-lapse video showing cristae dynamics during mitochondrial fusion event. Note finger-like protrusion from the end of mitochondrion on the left, appearing to bridge the membranes of the two mitochondria prior to organelle fusion.

# CHAPTER FOUR

## Milton1 regulates mitochondrial morphology by controlling Drp1 activity

**Running Title:** Role of Milton1 in mitochondrial dynamics

Dane M. Wolf[1,2], Kyle M. Trudeau[1], Evan P. Taddeo[2], Seungyoon B. Yu[3], Shili Xu[2], Mayuko Segawa[2], Marc Liesa[2], Yair Anikster[4-6], Alexander M. van der Bliek[7,8], Thomas L. Schwarz[9], Gulcin Pekkurnaz[3,9], and Orian S. Shirihai[2,10]

**Author information**

1. Department of Medicine, Obesity and Nutrition Section, Evans Biomedical Research Center, Boston University School of Medicine, 650 Albany Street, Boston, MA 02118, USA.

2. Department of Medicine, and Department of Molecular and Medical Pharmacology, David Geffen School of Medicine, University of California Los Angeles, CA 90095, USA.

3. Neurobiology Section, Division of Biological Sciences, University of California San Diego, La Jolla, CA 92093, USA.

4. Metabolic Disease Unit, Edmond and Lily Safra Children's Hospital, Sheba Medical Center, Tel-Hashomer, Israel.

5. The Wohl Institute for Translational Medicine, Sheba Medical Center, Tel-Hashomer, Israel.

6. Sackler Faculty of Medicine, Tel-Aviv University, Tel-Aviv, Israel.

7. Molecular Biology Institute at UCLA, Los Angeles, CA, USA.

8. Department of Biological Chemistry, David Geffen School of Medicine at UCLA, Los Angeles, CA, USA.

9. The F.M. Kirby Neurobiology Center, Boston Children's Hospital and Department of Neurobiology, Harvard Medical School, Boston, MA 02115, USA.

10. Department of Medicine/Division of Endocrinology, University of California, Los Angeles, CA, USA.

**Corresponding author:**

Orian S. Shirihai, Department of Molecular and Medical Pharmacology, David Geffen School of Medicine, University of California, 650 Charles East Young Drive South, Room 27-200, Los Angeles, California 90095, USA. Tel: +1-617-230-8570; Fax: +1-617-638-7124; Email: OShirihai@mednet.ucla.edu.

**Keywords:** Milton1, OIP106, TRAK1, Drp1, mitochondrial motility, dynamics, mtDNA, nucleoids, mitobulbs

**Abstract**

Mitochondria dynamically remodel their morphology through fusion, fission, and movement of their membranes. The mechanisms by which mitochondria change their shapes, however, has focused mainly on the roles of the Dynamin-related proteins

(DRPs), MFN1/2, OPA1, and DRP1. While mitochondrial movement represents a fundamental aspect of mitochondrial dynamics, the role of mitochondrial motor-complex proteins in determining the shape of mitochondria remains obscure. To explore the relationship between mitochondrial motility and morphology, we examined the role of the motor-adaptor protein, Milton1 (also called TRAK1), in regulating the architecture of the organelle. We found that patient-derived fibroblasts containing a null-mutation for Milton1 had fragmented mitochondria, and exogenous reintroduction of Milton1 was sufficient to restore the filamentous mitochondrial morphology. Remarkably, Milton1-KO in INS1 cells resulted in mitochondrial fragmentation without affecting mitochondrial motility. Conversely, overexpression of Milton1 induced mitochondrial hyper-tubulation, clustering of mtDNA, and a marked increase in phosphorylation of $Ser^{637}$ of DRP1. Altogether, our study highlights a novel role of the mitochondrial motility protein, Milton1, in the regulation of mitochondrial architecture.

**Introduction**

Mitochondria are highly dynamic, double-membraned organelles, which continuously undergo fusion and fission to maintain cellular and organismal homeostasis. The principal mediators of mitochondrial dynamics are the Dynamin-related proteins (DRPs), Mitofusins 1 and 2 (MFN1/2) (Hales and Fuller, 1997; Santel and Fuller, 2000), Optic Atrophy 1 (OPA1) (Olichon *et al*., 2003), and Dynamin-related Protein 1 (DRP1) (Otsuga *et al*., 1998; Smirnova *et al*., 2001). Fusion of the outer and inner mitochondrial membranes (OMM and IMM) require MFN1/2 and OPA1, respectively. Mitochondrial

fission depends on DRP1. While the merging and division of membranes entails movement, the role of mitochondrial motility proteins in shaping mitochondrial morphology remains unclear.

Mitochondrial movement requires attachment of the organelle to the cytoskeleton. The classical model of the mitochondrial motor complex depicts Milton1 functioning as a key motor-adaptor, linking the OMM-embedded Mitochondrial Rho GTPase (Miro) to the molecular motors Kinesin and Dynein, which, in turn associate with microtubules, driving anterograde and retrograde movement, respectively (Macaskill *et al*., 2009; Saotome *et al*., 2008; Wang and Schwarz, 2009). Given the integral position of Milton1 as a motor-adaptor protein, connecting mitochondria to the cytoskeleton, it appeared to also be a viable candidate for linking the motor complex to the molecular machinery of fusion and fission. The majority of studies investigating the function of Milton1, however, have focused on its role as a mediator of mitochondrial trafficking. Intriguingly, ectopic expression of Milton1 has been shown to induce mitochondrial elongation and the formation of bulbous structures containing aggregates of mtDNA (Koutsopoulos *et al*., 2010). It is unclear, however, whether deletion of Milton1 also results in altered mitochondrial morphology, whether such an alteration may be due to altered fusion and/or fission, and whether Milton1 may affect the expression or activities of the DRPs that exert the most direct influence over the maintenance of mitochondrial architecture.

Here, we explored the role of Milton1 in regulating mitochondrial morphology, using a combination of patient-derived and cell-culture KO models. We find that the loss of Milton1 results in mitochondrial fragmentation, which can be rescued by reintroduction of the wild-type (WT) protein at endogenous levels. Furthermore, we observe that the deletion of Milton1 in INS1 cells results in fragmentation without affecting mitochondrial motility, suggesting that the manner in which Milton1 induces mitochondrial fragmentation is not merely due to its role in promoting mitochondrial movement. Remarkably, we find that the hyper-tubulation and mtDNA clustering associated with Milton1 overexpression is associated inhibition of Drp1 in INS1 cells. Conversely, we determined that INS1 cells lacking Milton1 exhibit increased DRP1 activation. Our data indicate, therefore, that Milton1 not only regulates mitochondrial architecture but does so by influencing the ability of DRP1 to execute fission.

## Methods

### Cell culture

Human fibroblasts were cultured in DMEM (12100-046), supplemented with sodium bicarbonate, Pen/Strep, sodium pyruvate, HEPES, 10% FBS, and incubated 5% $CO_2$. INS1 cells were cultured in RPMI-1640 (31800022), supplemented with sodium bicarbonate, Pen/Strep, sodium pyruvate, HEPES, 10% FBS, and incubated 5% $CO_2$.

### KO and overexpression models

Human fibroblasts were obtained from patients, as previously described (Barel *et al*.,

2017). Crispr/Cas9-mediated Milton1-KO cells were generated with the following gRNA: GTTCTATGTGCCGAAAGAGT. Briefly, adenoviral transduction with respective constructs was performed 48 hr prior to imaging or Western blot analysis.

**Live-cell imaging**

Imaging was performed with the Zeiss LSM 880 with Airyscan. Cells were plated in CELLview 4-compartment glass-bottom tissue culture dishes (Greiner Bio-One, 627870), PS, 35/10 mm 48 hrs prior to imaging. Tetramethylrhodamine, ethyl ester (TMRE) and PicoGreen were added to cells as we previously described (Waters *et al*., 2018; Wolf *et al*., 2019).

**Image analysis**

ImageJ (Schneider et al., 2012) was used to analyze processed Airyscan images. Background was subtracted from images using a rolling ball filter = 50. Subsequently, images were cropped and quantified using macros. If comparing fluorescence intensity, we used the Window/Level function for representative images. If comparing morphology, we adjusted pixel intensities to optimally show relevant differences in mitochondrial architecture.

**Immunoblotting**

SDS–PAGE assays were performed by separating 20–30 μg of protein on precast polyacrylamide NuPAGE gels (Thermo Fisher Scientific, NP0321BOX). Transfer to

nitrocellulose membranes (LC2001) was conducted using transfer buffer (NP0006-1) containing 10% methanol. Membranes were blocked for 1 hr in 5% milk, prior to washing 3X for 5 min in PBST. The following primary and secondary antibodies were used: Drp1/DLP1 1:1,000 (BD Biosciences, 611112); Phospho-DRP1 (Ser637) 1:1,000 (Cell Signaling Technology, 4867S); β-actin 1:10,000 (Cell Signaling Technology, BH10D10); TOMM20 1:2,000 (Abcam, ab78547); TRAK1 1:1,000 (Sigma, HPA005853); anti-mouse IgG, HRP-linked antibody (Cell Signaling Technology, 7076S); and anti-rabbit IgG, HRP-linked antibody (Cell Signaling Technology, 7074S). Proteins were detected and imaged using SuperSignal West Femto Maximum Sensitivity Substrate (Thermo Fisher, 34095) and ChemiDoc MP Imaging System (Bio-Rad), respectively. Densitometry was conducted using ImageJ (Fiji) (Schneider et al., 2012).

**Statistical Analysis**

Microsoft Excel and GraphPad Prism were used to perform statistical analysis. Data were subjected to D'Agostino–Pearson omnibus and/or Shapiro–Wilk normality tests to determine if data followed normal distributions. Data were then subjected to 2-tailed Student's *t*-tests or one-way ANOVA. P values $< 0.05$ were considered statistically significant. Error bars represent standard deviation, unless otherwise indicated. N = the number of independent experiments, and statistical analysis was performed on the averages from independent experiments.

## Results

### Loss of Milton1 results in mitochondrial fragmentation

To explore the potential role the motor-adaptor protein, Milton1 (Fig. 4.1A), in maintaining mitochondrial morphology, we began by examining fibroblasts, derived from 2 patients with null mutations in the Milton1 gene (Fig. 4.1B–C). Using live-cell Airyscan imaging, we observed that human fibroblasts lacking Milton1 tended to have fragmented mitochondria (Fig. 4.1D). To quantify this apparent alteration in mitochondrial architecture, we used the common shape descriptors, aspect ratio and circularity. Both Milton1-null patient-derived fibroblasts exhibited significantly decreased mitochondrial aspect ratio (Fig. 4.1E and 4.1G) and significantly increased mitochondrial circularity (Fig. 4.1F and 4.1H), corresponding to mitochondrial fragmentation.

### Milton1 reintroduction into Milton1-null cells rescues fragmented mitochondria

We next determined whether reintroducing Milton1 into the patient-derived Milton1-null fibroblasts could restore their mitochondrial architecture. Using the cells from Patient #1, we reintroduced the wild-type (WT) Milton1 protein by performing transient adenoviral transductions (~48 hrs), resulting in different levels of Milton1 protein expression (Fig. 4.2A–B). Live-cell Airyscan imaging indicated that reintroduction of Milton1 not only restored mitochondrial motility (Fig. 4.2D) but also promoted mitochondrial elongation and branching, corresponding to the levels of exogenous Milton1 expression.

**Milton1-KO and overexpression in INS1 cells induce mitochondrial fragmentation and hyper-elongation, respectively, suggesting interaction with DRP1**

To examine whether Milton1 plays a role in maintaining mitochondrial architecture in other cell types, we generated Crispr/Cas9-mediated Milton1-KO INS1 cells (Fig. 4.3A–B). Similar to the Milton1-null human fibroblasts, loss of Milton1 expression in INS1 cells appeared to result in mitochondrial fragmentation. Remarkably, deletion of Milton1 from INS1 cells did not decrease mitochondrial motility (Fig. 4.3D) but still resulted in significantly decreased mitochondrial aspect ratio (Fig. 4.3E) and increased circularity (Fig. 4.3F), suggesting that the role of Milton1 in modifying mitochondrial architecture is not merely dependent on its well-established role in promoting mitochondrial motility. To further probe the role of Milton1 as a regulator of mitochondrial morphology, we explored the effects of Milton1 overexpression. After confirming the overexpression of adeno-Milton1-WT protein with a range of concentrations (Fig. 4.4A–B), we used a MOI of 100 to subsequently examine the possible influence of Milton1 overexpression on mitochondrial shape. Of note, we observed that supra-physiological levels of Milton1 in INS1 cells not only resulted in mitochondrial hyper-elongation (Fig. 4.4C–E) but also exhibited clustering of mtDNA into “mitobulbs”, previously documented in cells deficient in the mitochondrial fission protein, Drp1. Indeed, inhibition of Drp1 in INS1 cells through adenoviral overexpression of the Dominant-Negative Drp1 mutant resulted in an analogous phenotype to the Milton1-overexpressing INS1 cells (Fig. 4.4C,F,G).

**pSer$^{637}$ of DRP1 is increased and decreased in the context of Milton1 overexpression and KO, respectively**

The similarity of the phenotypes in the Milton1- vs. Drp1-DN-overexpressing INS1 cells prompted us to examine whether the activity of Drp1 might be altered according to levels of Milton1. Drp1 activity is regulated by a variety of post-translational modifications. Phosphorylation of Ser$^{637}$ has been shown to be associated with decreased mitochondrial fission. To test whether the hyper-elongation that we observed in Milton1-overexpressing cells could be associated with decreased mitochondrial fission, we overexpressed Milton1 at different levels and looked at Ser$^{637}$ phosphorylation status. Intriguingly, we found that, as Milton1 protein levels increase, so, too, do levels of phosphorylation at Ser$^{637}$ (Fig. 4.5A–B). Conversely, examination of Milton1-KO INS1 cells showed significantly lower levels of Ser$^{637}$ phosphorylation (Fig. 4.5C–D). Overall, our data point to a novel role of the mitochondrial motor-adaptor protein, Milton1, in regulating mitochondrial architecture.

**Discussion**

The tendency of mitochondria to dynamically change their shapes was observed as early as the late 19$^{th}$ century by microscopists, such as Carl Benda (Benda, 1898). The molecular mechanisms by which these shape changes occur, however, remained enigmatic for around a century – till the discovery of the DRPs that directly mediate fusion and fission of the two mitochondrial membranes. In the last two decades, numerous studies have demonstrated, in increasingly granular detail, how MFN1/2,

OPA1, and DRP1 control mitochondrial architecture. More recently, studies of mitochondrial dynamics have begun to extend beyond the DRPs, identifying roles for a range of other proteins (Gandre-Babbe and van der Bliek, 2008), vesicles (Nagashima *et al*., 2020), and even whole organelles (Lewis *et al*., 2016), in effectuating the complex processes of mitochondrial fusion and fission.

While organelle movement is fundamentally implicated in processes involving the merging and division of their membranes, the role of motility proteins in mitochondrial dynamics has not been studied in great depth. Given its central role in connecting mitochondria to the cytoskeleton, we focused on Milton1 as an attractive candidate for linking the machinery of mitochondrial motility to that of fusion and/or fission. Here, we showed that the loss of Milton1 in patient-derived fibroblasts does not merely result in decreased motility but also leads to mitochondrial fragmentation, indicating that Milton1 indeed plays a role in regulating mitochondrial morphology. This conclusion was strengthened by our finding that adenoviral reintroduction of Milton1 at endogenous levels was sufficient to elongate the mitochondria to levels in control fibroblasts. Interestingly, Milton1 KO in INS1 cells also resulted in mitochondrial fragmentation, but we did not detect any alteration in mitochondrial motility. This indicates that Milton1 is not essential for mitochondrial movement in INS1 cells but nevertheless influences mitochondrial dynamics, suggesting that the reason mitochondria are fragmented in the absence of Milton1 is due to a more direct effect on fusion and/or fission.

The hyper-tubulation and mtDNA clustering resulting from Milton1 overexpression suggested to us that Milton1 might be influencing the activity of DRP1, since inhibition of DRP1 also results in extensive mitochondrial elongation and mitobulb formation (Ban-Ishihara *et al*., 2013). To further probe this possibility, we examined the phosphorylation status of $Ser^{637}$ of DRP1, because increased or decreased phospho-$Ser^{637}$ has been shown to be associated with inhibition or activation of DRP1, respectively (Cereghetti *et al*., 2008; Chang and Blackstone, 2007; Cribbs and Strack, 2007). Notably, Milton1 overexpression in INS1 cells resulted in significantly increased phospho-$Ser^{637}$, whereas Milton1-KO INS1 cells had significantly decreased phospho-$Ser^{637}$. Together, our data indicate that Milton1 regulates mitochondrial morphology, at least in part, by influencing the activity of DRP1, the key protein controlling mitochondrial fission.

While our study indicates that Milton1 affects mitochondrial dynamics through its association with DRP1, determining exactly how these proteins interact requires further study. Protein Kinase A phosphorylates and Calcineurin dephosphorylates $Ser^{637}$, therefore, it is plausible that Milton1 could affect the kinase or phosphatase activities of these enzymes, respectively. It has also been shown that DRP1 is O-GlcNAcylated and that this post-translational modification increases its activity (Gawlowski *et al*., 2012). It remains unknown, however, whether DRP1 is O-GlcNAcylated at $Ser^{637}$, specifically. Since Milton1 has been shown to strongly associate with *O*-GlcNAc Transferase (OGT), it is feasible that alterations in Milton1 expression could affect that ability of OGT to target DRP1, thereby altering its ability to execute fission.

In conclusion, we identify a novel role of the motor-adaptor protein, Milton1, in regulating mitochondrial architecture by influencing the activity of DRP1, highlighting the basic interconnection of mitochondrial motility with fusion and fission. Given that perturbations in mitochondrial movement and morphology are associated with a variety of severe pathologies, such as Parkinson's disease, further elucidating the relationship between mitochondrial motor proteins and fusion/fission factors will likely yield important clues as to why the disruption of mitochondrial dynamics so frequently results in cellular dysfunction.

**Acknowledgements**

We would like to extend our gratitude to the referees and editor, who carefully examined our manuscript and whose insights and feedback greatly helped us to improve its quality. We thank Drs. György Hajnóczky, Barbara Corkey, Martin Picard, Gilad Twig, and Daniel Dagan for helpful discussions. OSS is funded by NIH-NIDDK 5-RO1DK099618-02. ML and MS are funded by UCLA Department of Medicine Chair commitment and UCSD/UCLA Diabetes Research Center grant, NIH P30 DK063491.

**Author contributions**

DMW and OSS conceived the study. DMW made the figures and wrote the article. DMW performed the Airyscan imaging, Western blotting, and data analysis. KMT, EPT, SBY, and MS assisted with experimentation and data analysis. SX generated the Crispr/Cas9 Milton1-KO INS1 cells. YA provided Milton1-null fibroblasts. ML,

AMVDB, TLS, and GP assisted with study design and helped to edit the manuscript. OSS supervised the study and assisted with editing the manuscript.

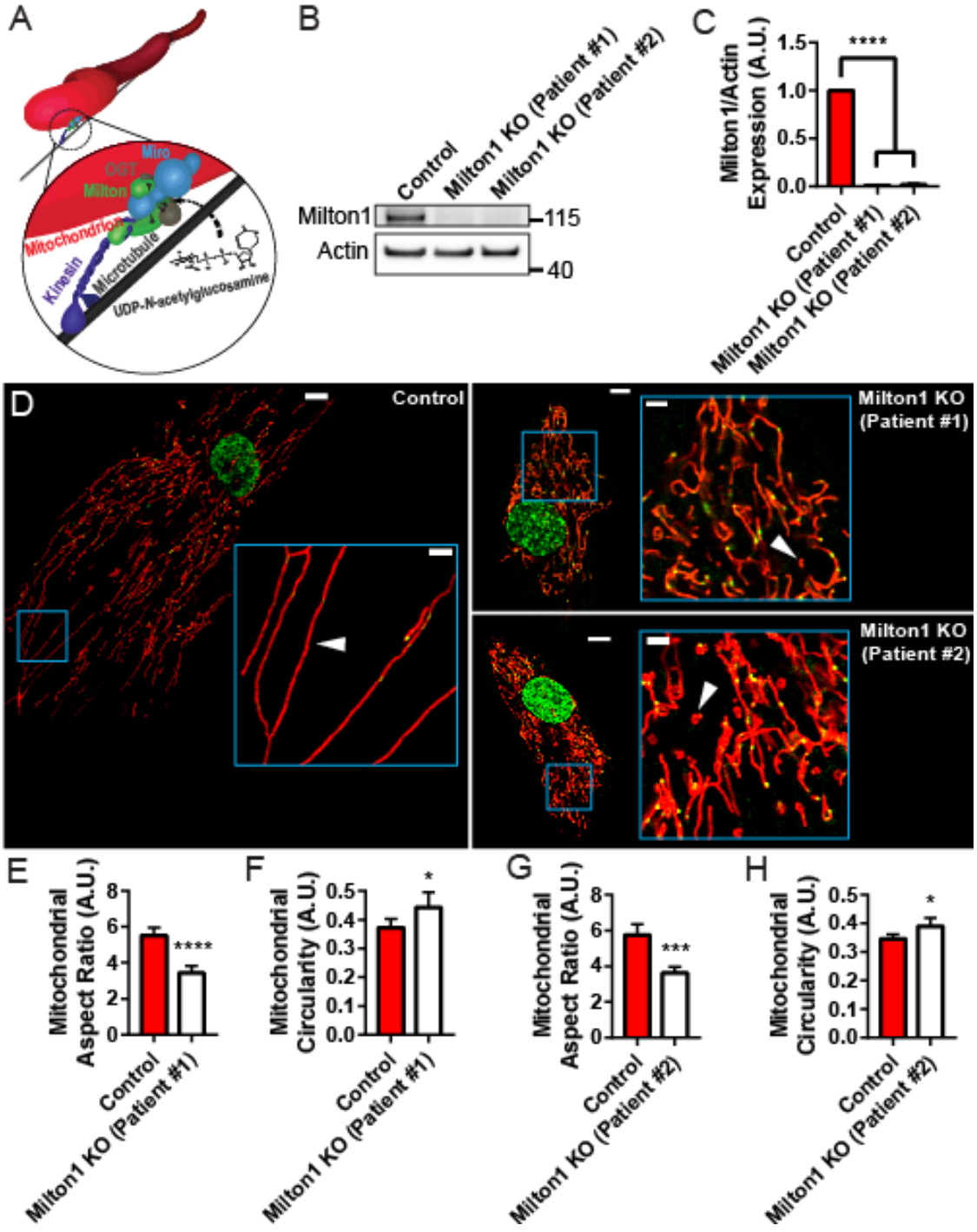


**Figure 4.1. Milton1-null patient-derived fibroblasts have fragmented mitochondria.**

A. Illustration of Milton as a motor-adaptor protein within the mitochondrial motor complex. Note that Milton connects the mitochondrion to the microtubule through its

association with Miro and Kinesin (or Dynein). Milton also strongly associates with OGT, which *O*-GlnNAcylates Milton and decreases mitochondrial movement.

B. Western blot analysis of Milton1 from human fibroblasts, showing loss of Milton1 expression from 2 patients with null mutations in Milton1 compared to a normal control. N = 4 independent experiments.

C. Quantification of B. N = 4 independent experiments.

D. Live-cell, Airyscan images of control human fibroblast (left) and Milton1-KO fibroblasts (right), stained with TMRE and PicoGreen. Arrowheads indicate elongated vs. shortened mitochondria in control and Milton1-KO cells, respectively. Scale bars of zoomed-out images = 5 μm and zoomed-in regions = 2 μm.

E. Quantification of mitochondrial aspect ratio ($Mito_{long\ axis}/Mito_{short\ axis}$) of control vs. Milton1-KO (Patient #1). N = 3 independent experiments.

F. Quantification of mitochondrial circularity ($4\pi Area/perimeter^2$) of control vs. Milton1-KO (Patient #1). N = 3 independent experiments.

G. Quantification of mitochondrial aspect ratio ($Mito_{long\ axis}/Mito_{short\ axis}$) of control vs. Milton1-KO (Patient #2). N = 3 independent experiments.

H. Quantification of mitochondrial circularity ($4\pi Area/perimeter^2$) of control vs. Milton1-KO (Patient #2). N = 3 independent experiments.

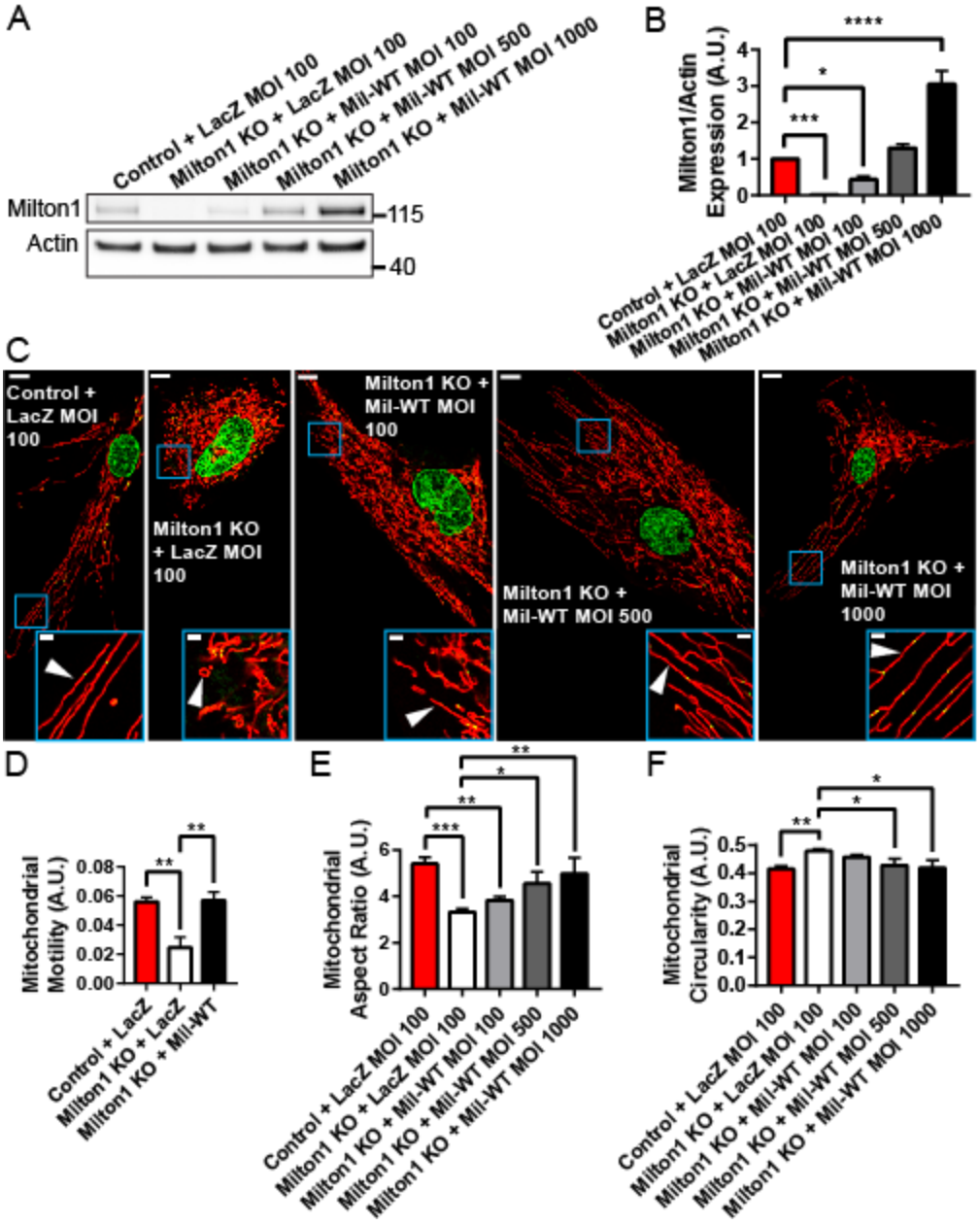


**Figure 4.2. Reintroduction of Milton1 in KO fibroblasts restores mitochondrial motility and morphology.**

A. Western blot analysis of Milton1 in which wild-type (WT) Milton1 is reintroduced into Milton1-null fibroblasts from Patient #1 via increasing concentrations of adenovirus. N = 3 independent experiments.

B. Quantification of B. N = 3 independent experiments.

C. Live-cell Airyscan images of control fibroblasts, transduced with adeno-LacZ, compared to Milton1 KO, transduced with adeno-LacZ or increasing concentrations of adeno-Milton1 (left to right, respectively) and stained with TMRE and PicoGreen. Arrowheads indicate mitochondria. Note that reintroduction of Milton1 into Milton1-null fibroblasts restores mitochondrial architecture in a concentration-dependent manner. Scale bars of zoomed-out images = 10 μm and zoomed-in regions = 2 μm. N = 3 independent experiments.

D. Quantification of mitochondrial motility from Airyscan time-lapse images. Note that Milton1-null fibroblasts have significantly decreased mitochondrial movement. Reintroducing Milton1 (MOI = 1000) restores mitochondrial motility to control levels. N = 3.

E. Quantification of live-cell Airyscan images from C, showing that reintroduction of Milton1 into Milton1-null fibroblasts tends to increase mitochondrial aspect ratio, promoting mitochondrial elongation. N = 3 independent experiments.

F. Quantification of live-cell Airyscan images from C, showing that reintroduction of Milton1 into Milton1-null fibroblasts tends to decrease mitochondrial circularity, promoting mitochondrial branching. N = 3 independent experiments.

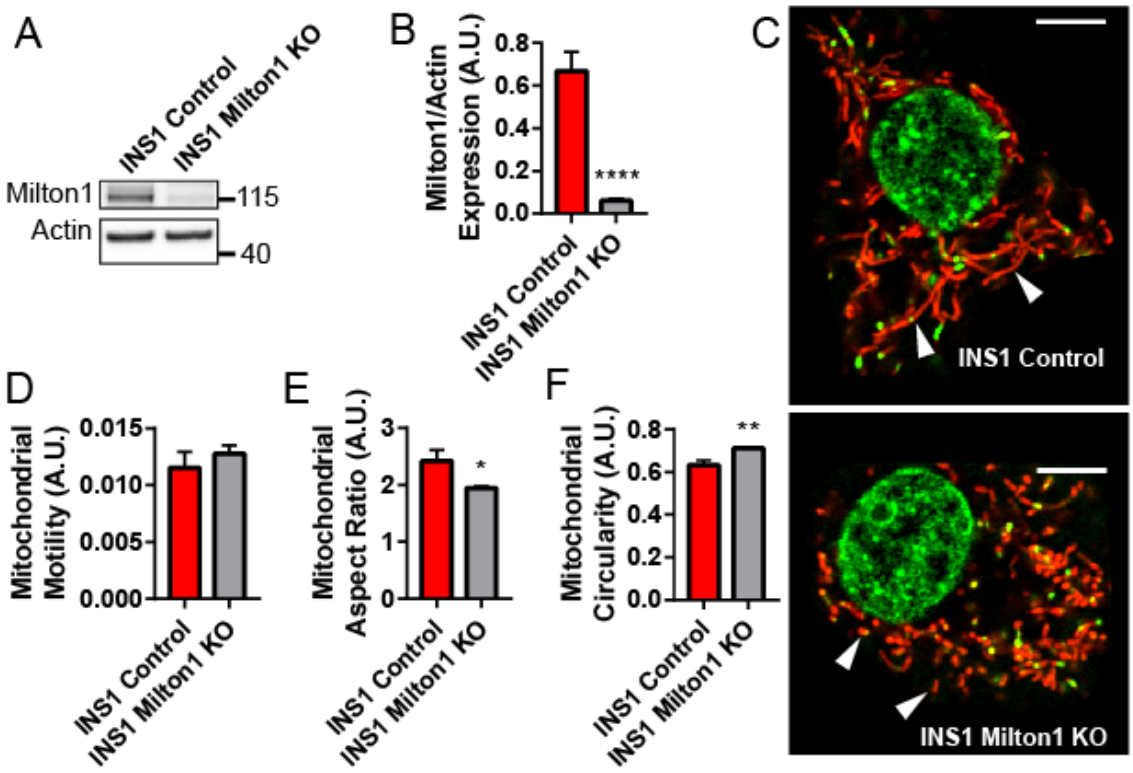


**Figure 4.3. Milton1 KO in INS1 cells results in mitochondrial fragmentation, without affecting mitochondrial motility.**

A. Western blot analysis showing Crispr/Cas9-mediated KO of Milton1 in INS1 cells. N = 4 independent experiments.

B. Quantification of A, showing significant decrease in Milton1 expression. N = 4 independent experiments.

C. Live-cell Airyscan images of INS1 control (top) vs. INS1 Milton1 KO cells, stained with TMRE and PicoGreen. Scale bars = 5 μm. N ≥ 3 independent experiments. Arrowheads indicate mitochondria. Note the loss of Milton1 tends to result in a larger proportion of punctate mitochondria.

D. Quantification of mitochondrial motility from time-lapse images in C. $N \geq 3$ independent experiments. Note that mitochondrial motility is unaltered in Milton1 KO cells, indicating that alternative motors can mediate mitochondrial movement in INS1 cells.

E. Quantification of mitochondrial aspect ratio from C. $N \geq 3$ independent experiments. Note that Milton1-KO INS1 cells tend to exhibit mitochondrial fragmentation, while maintaining mitochondrial motility, suggesting a novel role of Milton1 in mitochondrial shape determination, independent of its well-documented role in mitochondrial movement.

F. Quantification of mitochondrial circularity from C, showing the tendency of Milton1-KO INS1 cells to have an increased number of circular mitochondria. $N \geq 3$ independent experiments.

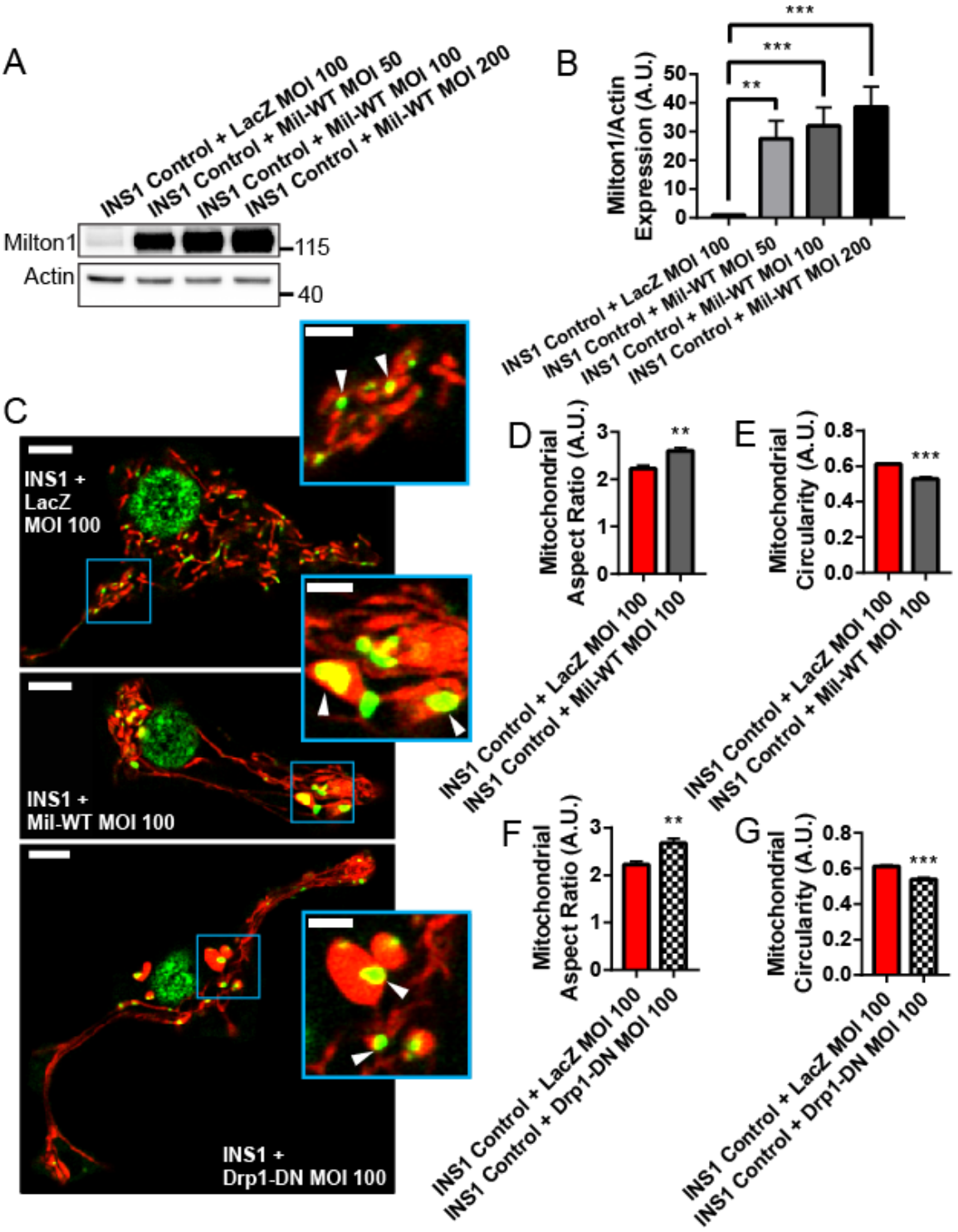
A
INS1 Control + LacZ MOI 100
INS1 Control + Mil-WT MOI 50
INS1 Control + Mil-WT MOI 100
INS1 Control + Mil-WT MOI 200
Milton1
Actin
115
40
B
Milton1/Actin Expression (A.U.)
50
40
30
20
10
0
**
***
***
INS1 Control + LacZ MOI 100
INS1 Control + Mil-WT MOI 50
INS1 Control + Mil-WT MOI 100
INS1 Control + Mil-WT MOI 200
C
INS1 + LacZ MOI 100
INS1 + Mil-WT MOI 100
INS1 + Drp1-DN MOI 100
D
Mitochondrial Aspect Ratio (A.U.)
3
2
1
0
**
INS1 Control + LacZ MOI 100
INS1 Control + Mil-WT MOI 100
E
Mitochondrial Circularity (A.U.)
0.8
0.6
0.4
0.2
0.0
***
INS1 Control + LacZ MOI 100
INS1 Control + Mil-WT MOI 100
F
Mitochondrial Aspect Ratio (A.U.)
3
2
1
0
**
INS1 Control + LacZ MOI 100
INS1 Control + Drp1-DN MOI 100
G
Mitochondrial Circularity (A.U.)
0.8
0.6
0.4
0.2
0.0
***
INS1 Control + LacZ MOI 100
INS1 Control + Drp1-DN MOI 100

**Figure 4.4. Overexpression of Milton1 results in mitochondrial hyperfusion and mitobulb formation, resembling the phenotype of Dominant-Negative Drp1.**

A. Western blot analysis of INS1 cells with increasing levels of adeno-Milton1-WT overexpression. N = 3 independent experiments.

B. Quantification of A, showing significant overexpression of Milton1 with increasing levels of adenoviral transduction.

C. Live-cell Airyscan images of INS1 cells expressing adeno-LacZ (top), Mil-WT (middle), or Drp1-DN (bottom), stained with TMRE and PicoGreen. Scale bars of zoomed-out images = 5 μm and zoomed-in regions = 2 μm. N ≥ 3 independent experiments. Note the similarities between the effects of Milton1-WT and Drp1-DN overexpression, resulting in mitochondrial hyperfusion and aggregation of mtDNA into mitobulbs.

D. Quantification of mitochondrial aspect ratio from C, showing significantly increased mitochondrial elongation due to overexpression of Milton1. N ≥ 3 independent experiments.

E. Quantification of circularity from C, corresponding to significantly increased mitochondrial branching resulting from Milton1 overexpression. N ≥ 3 independent experiments.

F. Quantification of mitochondrial aspect ratio from C, showing significantly increased mitochondrial elongation due to overexpression of Drp1-DN. N ≥ 3 independent experiments.

G. Quantification of circularity from C, corresponding to significantly increased mitochondrial branching resulting from Drp1-DN overexpression. $N \geq 3$ independent experiments.

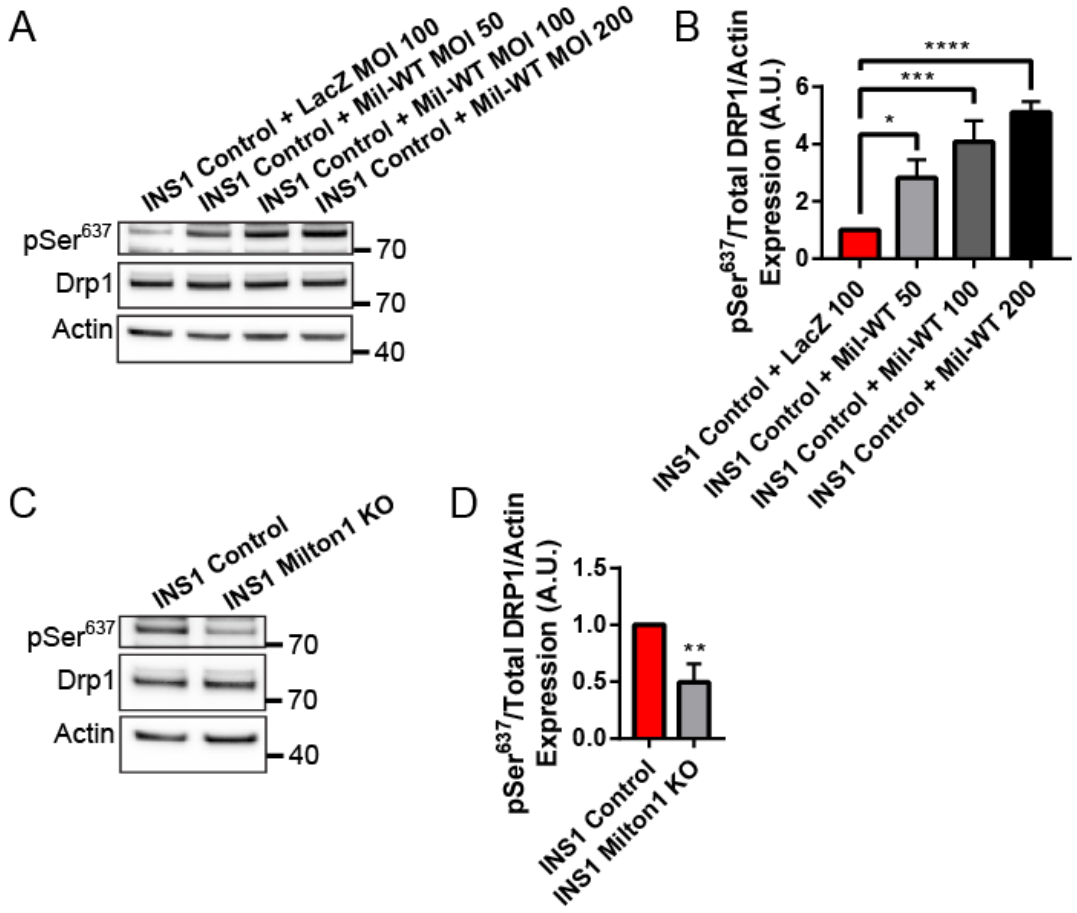


**Figure 4.5. Milton1 regulates Drp1 Ser$^{637}$-phosphorylation status in INS1 cells.**

A. Western blot analysis of phospho-Ser$^{637}$ of Drp1 in INS1 cells overexpressing Milton1. N = 3. Note that with increasing Milton1 expression, there is increasing p Ser$^{637}$.

B. Quantification of A, showing significantly increased pSer$^{637}$ with Milton1 expression. N = 4. Note that various studies indicate that phosphorylation of Ser$^{637}$ of Drp1 is associated with decreased mitochondrial fission.

C. Western blot analysis of phospho-Ser$^{637}$ of Drp1 in Milton1-KO INS1 cells. N = 3.

D. Quantification of C, showing significant decrease in pSer$^{637}$ in INS1 cells lacking Milton1. N = 4. Note that the decrease in pSer$^{637}$ is associated with increased activity of Drp1 and higher levels of mitochondrial fission.

# CHAPTER FIVE

## General Discussion

As Palade demonstrated in his EM studies in the early 1950s, the ability to visualize biological structures provides great insight into their function. Discovery of the internal complexities of the mitochondrion complemented the earlier biochemical revelations of Krebs, Lehninger, and others, that the mitochondria housed the enzymes of both the citric acid cycle as well as the OXPHOS machinery. Together, these insights provided a basis for Mitchell's chemiosmotic theory, around a decade later, postulating that ATP synthesis is ultimately driven by an electrochemical gradient of hydrogen ions established across the IMM. While these discoveries provided profound insights into the nature of energy production in aerobic organisms, they were nevertheless limited by a longtime inability to visualize both the structure and function of the IMM in real time. For this reason, key aspects as to character of the $\Delta p$ remained obscure for decades. Indeed, studies purporting that the $\Delta\Psi_m$ represented an equipotential appeared to overlook the fact that conventional confocal microscopes were unable to resolve individual cristae membranes and were therefore ill-suited for addressing the question as to whether the $\Delta\Psi_m$ were evenly distributed along the IMM or subject to compartmentalization.

Using Airyscan and STED, we effectively resolved cristae in living cells and demonstrated that $\Delta\Psi_m$-dependent dyes do not uniformly label the IMM, as would be expected if the distribution of ions were evenly distributed from one end of the mitochondrion to the other. Rather, we observed heterogeneous patterns, with the highest

FI associated with cristae membranes and relatively lower FI associated with IBMs. This disparity in the distribution of charges along the IMM indicates that there is some electrical insulation associated with cristae membranes, such that the charges associated with the cristae are not able to freely diffuse throughout the IMS. Since deletion of key components of the MICOS complex, as well as OPA1, resulted in decreased $\Delta\Psi_m$ heterogeneity, we reasoned that the framework around the CJs likely functions as an electrical insulator, effectively compartmentalizing the microdomains of individual cristae into bioenergetic units. This conclusion was strengthened by our observation that the most polarized membranes in our study were derived from mutants that promoted the formation of internal vesicles. In the double KO of DRP1 and OPA1, the IMM was unable to fuse, which tended to produce cristae fragments, completely unanchored from the IMM. Since these vesicles contained respiratory complexes but lacked CJs, their level of electrical insulation was enhanced, and, as a result, they possessed membrane potentials that were 2 to 3 times higher than in control cells. Lastly, we observed that both targeted and random laser-induced phototoxicity resulted in some cristae depolarizing while others maintained their polarities. Such a scenario is not compatible with the possibility that a single mitochondrion is similar to an electrical wire, because, in the case of a single, electrically connected structure, the loss of potential at one point would lead to a simultaneous loss of potential at all other points. Where there is some electrical insulation, on the other hand, it is explicable that depolarization in one region would not result in the total collapse of $\Delta\Psi_m$ within the whole organelle.

Our novel approach for imaging cristae in living cells yielded new insights into the nature of the electrochemical gradient, offering an alternative paradigm that the $\Delta p$ is compartmentalized in cristae. Compartmentalization would appear to offer some advantage to the mitochondrion. Clearly, if one crista is dysfunctional, it would be beneficial if its depolarization would not compromise the entire organelle. In many respects, this is similar to the rationale for using bulkheads in ships, so that a leak in one part of the hull will be sealed off and will not cause the entire vessel to sink. Another reason that compartmentalization of the electrochemical gradient could be beneficial is that the protons pumped by complexes I, III, and IV will remain near the sites of ATP Synthase, promoting their reentry back into the matrix, thereby increasing the efficiency of ATP synthesis. There might, as well, be some advantage of electrochemical compartmentalization for protein import from the cytosol. If the $\Delta\Psi_m$ were uniformly distributed around the IMM, positive charges in the IMS could repel the import of proteins containing a positively-charged mitochondria-targeting sequence. Conversely, if the $\Delta\Psi_m$ were lower near the IBM, protein import would encounter less resistance and therefore require less energy. With the arrival of many different forms of live-cell, super-resolution imaging technologies, it is now increasingly feasible to probe these questions in still greater depth.

Given the increasing availability of advanced, live-cell imaging systems, together with a burgeoning interest in mitochondrial biology, there is a sudden demand for methods to quantify mitochondrial cristae from super-resolution micrographs. To address this need,

we developed a novel image-analysis protocol using the machine-learning plugin, TWS.

Remarkably, despite the fact that our SIM micrographs had roughly ten times less resolution than EMs, our method detected a similar cristae density. This suggests that our analysis procedure will be particularly useful for tracking changes in cristae density, following different interventions. Our analysis of real-time changes in cristae architecture (Segawa *et al*., 2020) confirmed previous findings that cristae are not static structures but indeed undergo continuous remodeling (Kondadi *et al*., 2020), appearing to engage in their own cycles of fusion and fission, analogous to the sort of mitochondrial dynamics that govern the architectural changes in the broader organelle.

Complementing our quantification of cristae dynamics, we also found that cristae appear to migrate away from sites of mitochondrial fission. Insofar as it would not appear to be beneficial to cleave the mitochondrion through the middle of a crista, as this would likely compromise its bioenergetic insulation, it would be advantageous to move cristae away from the fission site. We also observed interesting IMM remodeling prior to mitochondrial fusion, where finger-like protrusions appeared to bridge the fusing mitochondria, consistent with modeling of how OPA1 oligomers might promote highly curved membranous tips (Yan *et al*., 2020). Notably, we only observed these finger-like protrusions from one of the two fusing mitochondria, suggesting a heterotypic form of mitochondrial fusion with OPA1 on one end and cardiolipin on the other (Ban *et al*., 2017).

In addition to our explorations of the IMM, we also probed novel factors that regulate the whole mitochondrial network. Although the DRPs that directly mediate fusion and fission play the most pivotal roles in determining mitochondrial architecture in the cell, there is a growing number of other factors that have been found to also influence whether mitochondria maintain an elongated or fragmented network. Given the important role of mitochondrial motility in fusion and fission, we decided to focus on Milton1 as a protein that might not merely play a role in mitochondrial displacement but also communicate with fusion/fission factors that more directly mediate changes in mitochondrial shape.

Our discovery that loss of Milton1 results in mitochondrial fragmentation, and appears to be associated with increased DRP1 activity, underscores the idea that motility proteins have an underappreciated role in determining the shape of the organelle. This notion could provide mechanistic insight into how the mitochondrial motor complex can coordinate with the fusion and fission machinery to effectively execute membrane remodeling events that are vital for not just the function of the mitochondria but for the cell, at large. This interplay between motility proteins and the fusion/fission machinery is likely to be of particular importance in highly polarized cells, such as neurons, where the need for long-distance movement must be balanced against the need for regular cycles of fusion and fission for purposes of quality control.

In the final analysis, our studies highlight the fundamental relationship between mitochondrial architecture and bioenergetics. Introducing a novel paradigm of the $\Delta p$,

we demonstrate that the compartmentalization of the electrochemical gradient is a basic property of ATP production. Adding to the list of factors that influence mitochondrial morphology, we show that the motor-adaptor protein, Milton1, plays a key role in the maintenance of both the shape of mitochondrial membranes as well as the distribution of the mtDNA, which is critical for the expression of subunits of the ETC. Altogether, these studies provide new insights into how mitochondrial architecture functions as a framework for the metabolic processes that sustain aerobic life.

## BIBLIOGRAPHY

Abrahams, J.P., A.G.W. Leslie, R. Lutter, and J.E. Walker. 1994. Structure at 2.8A resolution of F1-ATPase from bovine heart mitochondria. *Nature*. 370:621-628.

Acehan, D., Y. Xu, D.L. Stokes, and M. Schlame. 2007. Comparison of lymphoblast mitochondria from normal subjects and patients with Barth syndrome using electron microscopic tomography. *Laboratory Investigation*. 87:40-48.

Amati-Bonneau, P., M.L. Valentino, P. Reynier, M.E. Gallardo, B. Bornstein, A. Boissiere, Y. Campos, H. Rivera, J.G. de la Aleja, R. Carroccia, L. Iommarini, P. Labauge, D. Figarella-Branger, P. Marcorelles, A. Furby, K. Beauvais, F. Letournel, R. Liguori, C. La Morgia, P. Montagna, M. Liguori, C. Zanna, M. Rugolo, A. Cossarizza, B. Wissinger, C. Verny, R. Schwarzenbacher, M.A. Martin, J. Arenas, C. Ayuso, R. Garesse, G. Lenaers, D. Bonneau, and V. Carelli. 2008. OPA1 mutations induce mitochondrial DNA instability and optic atrophy 'plus' phenotypes. *Brain*. 131:338-351.

Amchenkova, A.A. 1988. Coupling membranes as energy-transmitting cables. I. Filamentous mitochondria in fibroblasts and mitochondrial clusters in cardiomyocytes. *The Journal of Cell Biology*. 107:481-495.

Anand, R., V. Strecker, J. Urbach, I. Wittig, and A.S. Reichert. 2016. Mic13 Is Essential for Formation of Crista Junctions in Mammalian Cells. *PLoS One*. 11:e0160258.

Arganda-Carreras, I., V. Kaynig, C. Rueden, K.W. Eliceiri, J. Schindelin, A. Cardona, and H. Sebastian Seung. 2017. Trainable Weka Segmentation: a machine learning tool for microscopy pixel classification. *Bioinformatics*. 33:2424-2426.

Ban-Ishihara, R., T. Ishihara, N. Sasaki, K. Mihara, and N. Ishihara. 2013. Dynamics of nucleoid structure regulated by mitochondrial fission contributes to cristae reformation and release of cytochrome c. *Proceedings of the National Academy of Sciences of the United States of America*. 110:11863-11868.

Ban, T., T. Ishihara, H. Kohno, S. Saita, A. Ichimura, K. Maenaka, T. Oka, K. Mihara, and N. Ishihara. 2017. Molecular basis of selective mitochondrial fusion by heterotypic action between OPA1 and cardiolipin. *Nature Cell Biology*. 19:856-863.

Barbot, M., D.C. Jans, C. Schulz, N. Denkert, B. Kroppen, M. Hoppert, S. Jakobs, and M. Meinecke. 2015. Mic10 oligomerizes to bend mitochondrial inner membranes at cristae junctions. *Cell Metabolism*. 21:756-763.

Barel, O., M.C.V. Malicdan, B. Ben-Zeev, J. Kandel, H. Pri-Chen, J. Stephen, I.G. Castro, J. Metz, O. Atawa, S. Moshkovitz, E. Ganelin, I. Barshack, S. Polak-

Charcon, D. Nass, D. Marek-Yagel, N. Amariglio, N. Shalva, T. Vilboux, C. Ferreira, B. Pode-Shakked, G. Heimer, C. Hoffmann, T. Yardeni, A. Nissenkorn, C. Avivi, E. Eyal, N. Kol, E. Glick Saar, D.C. Wallace, W.A. Gahl, G. Rechavi, M. Schrader, D.M. Eckmann, and Y. Anikster. 2017. Deleterious variants in TRAK1 disrupt mitochondrial movement and cause fatal encephalopathy. *Brain*. 140:568-581.

Barrera, M., S. Koob, D. Dikov, F. Vogel, and A.S. Reichert. 2016. OPA1 functionally interacts with MIC60 but is dispensable for crista junction formation. *FEBS Letters*. 590:3309-3322.

Benda, C. 1898. Ueber die spermatogenese der vertebraten und höherer evertebraten, II. Theil: Die histiogenese der spermien. *Archiv für Anatomie, Physiologie*. 73:393–398.

Birk, A.V., S. Liu, Y. Soong, W. Mills, P. Singh, J.D. Warren, S.V. Seshan, J.D. Pardee, and H.H. Szeto. 2013. The mitochondrial-targeted compound SS-31 re-energizes ischemic mitochondria by interacting with cardiolipin. *Journal of the American Society of Nephrology*. 24:1250-1261.

Busch, K.B., G. Deckers-Hebestreit, G.T. Hanke, and A.Y. Mulkidjanian. 2013. Dynamics of bioenergetic microcompartments. *Biological Chemistry*. 394:163-188.

Caffrey, B.J., A.V. Maltsev, M. Gonzalez-Freire, L.M. Hartnell, L. Ferrucci, and S. Subramaniam. 2019. Semi-automated 3D segmentation of human skeletal muscle using Focused Ion Beam-Scanning Electron Microscopic images. *Journal of Structural Biology*. 207:1-11.

Cereghetti, G., A. Stangherlin, O. Martins de Brito, C. Chang, C. Blackstone, P. Bernardi, and L. Scorrano. 2008. Dephosphorylation by calcineurin regulates translocation of Drp1 to mitochondria. *Proceedings of the National Academy of Sciences of the United States of America*. 105:15803-15808.

Cerqueira, F.M., B. Chausse, B.M. Baranovski, M. Liesa, E.C. Lewis, O.S. Shirihai, and A.J. Kowaltowski. 2016. Diluted serum from calorie-restricted animals promotes mitochondrial beta-cell adaptations and protect against glucolipotoxicity. *FEBS Journal*. 283:822-833.

Chang, C.R., and C. Blackstone. 2007. Cyclic AMP-dependent protein kinase phosphorylation of Drp1 regulates its GTPase activity and mitochondrial morphology. *Journal of Biological Chemistry*. 282:21583-21587.

Cogliati, S., J.A. Enriquez, and L. Scorrano. 2016. Mitochondrial Cristae: Where Beauty Meets Functionality. *Trends in Biochemical Sciences*. 41:261-273.

Cribbs, J.T., and S. Strack. 2007. Reversible phosphorylation of Drp1 by cyclic AMP-dependent protein kinase and calcineurin regulates mitochondrial fission and cell death. *EMBO Reports*. 8:939-944.

Daum, B., A. Walter, A. Horst, H.D. Osiewacz, and W. Kuhlbrandt. 2013. Age-dependent dissociation of ATP synthase dimers and loss of inner-membrane cristae in mitochondria. *Proceedings of the National Academy of Sciences of the United States of America*. 110:15301-15306.

Davies, K.M., M. Strauss, B. Daum, J.H. Kief, H.D. Osiewacz, A. Rycovska, V. Zickermann, and W. Kuhlbrandt. 2011. Macromolecular organization of ATP synthase and complex I in whole mitochondria. *Proceedings of the National Academy of Sciences of the United States of America*. 108:14121-14126.

Duchen, M.R. 2004. Mitochondria in health and disease: perspectives on a new mitochondrial biology. *Molecular Aspects of Medicine*. 25:365-451.

Duchen, M.R., A. Leyssens, and M. Crompton. 1998. Transient mitochondrial depolarizations reflect focal sarcoplasmic reticular calcium release in single rat cardiomyocytes. *Journal of Cell Biology*. 142:975-988.

Dudkina, N.V., J. Heinemeyer, W. Keegstra, E.J. Boekema, and H.P. Braun. 2005. Structure of dimeric ATP synthase from mitochondria: an angular association of monomers induces the strong curvature of the inner membrane. *FEBS Letters*. 579:5769-5772.

Duvezin-Caubet, S., R. Jagasia, J. Wagener, S. Hofmann, A. Trifunovic, A. Hansson, A. Chomyn, M.F. Bauer, G. Attardi, N.G. Larsson, W. Neupert, and A.S. Reichert. 2006. Proteolytic processing of OPA1 links mitochondrial dysfunction to alterations in mitochondrial morphology. *Journal of Biological Chemistry*. 281:37972-37979.

Ehrenberg, B., V. Montana, M. Wei, J.P. Wuskell, and L.M. Loew. 1988. Membrane potential can be determined in individual cells from the Nernstian distribution of cationic dyes. *Biophysical Journal.* 53:785-794.

Farkas, D.L., M. Wei, P. Febbroriello, J.H. Carson, and L.M. Loew. 1989. Simultaneous imaging of cell and mitochondrial membrane potentials. *Biophysical Journal*. 56:1053-1069.

Frezza, C., S. Cipolat, O. Martins de Brito, M. Micaroni, G.V. Beznoussenko, T. Rudka, D. Bartoli, R.S. Polishuck, N.N. Danial, B. De Strooper, and L. Scorrano. 2006. OPA1 controls apoptotic cristae remodeling independently from mitochondrial fusion. *Cell*. 126:177-189.

Friedman, J.R., A. Mourier, J. Yamada, J.M. McCaffery, and J. Nunnari. 2015. MICOS coordinates with respiratory complexes and lipids to establish mitochondrial inner membrane architecture. *Elife*. 4.

Friedman, J.R., and J. Nunnari. 2014. Mitochondrial form and function. *Nature*. 505:335-343.

Gandre-Babbe, S., and A.M. van der Bliek. 2008. The novel tail-anchored membrane protein Mff controls mitochondrial and peroxisomal fission in mammalian cells. *Molecular Biology of the Cell*. 19:2402-2412.

Gawlowski, T., J. Suarez, B. Scott, M. Torres-Gonzalez, H. Wang, R. Schwappacher, X. Han, J.R. Yates, 3rd, M. Hoshijima, and W. Dillmann. 2012. Modulation of dynamin-related protein 1 (DRP1) function by increased O-linked-beta-N-acetylglucosamine modification (O-GlcNAc) in cardiac myocytes. *Journal of Biological Chemistry*. 287:30024-30034.

Giacomello, M., A. Pyakurel, C. Glytsou, and L. Scorrano. 2020. The cell biology of mitochondrial membrane dynamics. *Nature Reviews. Molecular Cell Biology*. 21:204-224.

Glancy, B., L.M. Hartnell, D. Malide, Z.X. Yu, C.A. Combs, P.S. Connelly, S. Subramaniam, and R.S. Balaban. 2015. Mitochondrial reticulum for cellular energy distribution in muscle. *Nature*. 523:617-620.

Glytsou, C., E. Calvo, S. Cogliati, A. Mehrotra, I. Anastasia, G. Rigoni, A. Raimondi, N. Shintani, M. Loureiro, J. Vazquez, L. Pellegrini, J.A. Enriquez, L. Scorrano, and M.E. Soriano. 2016. Optic Atrophy 1 Is Epistatic to the Core MICOS Component MIC60 in Mitochondrial Cristae Shape Control. *Cell Reports*. 17:3024-3034.

Gomes, L.C., G. Di Benedetto, and L. Scorrano. 2011. During autophagy mitochondria elongate, are spared from degradation and sustain cell viability. *Nature Cell Biology*. 13:589-598.

Griparic, L., T. Kanazawa, and A.M. van der Bliek. 2007. Regulation of the mitochondrial dynamin-like protein Opa1 by proteolytic cleavage. *Journal of Cell Biology*. 178:757-764.

Guarani, V., E.M. McNeill, J.A. Paulo, E.L. Huttlin, F. Frohlich, S.P. Gygi, D. Van Vactor, and J.W. Harper. 2015. QIL1 is a novel mitochondrial protein required for MICOS complex stability and cristae morphology. *Elife*. 4.

Gustafsson, M. 2000. Surpassing the lateral resolution limit by a factor of two using structured illumination microscopy. *Journal of Microscopy*. 198:82-87.

Hales, K., and M. Fuller. 1997. Developmentally Regulated Mitochondrial Fusion Mediated by a Conserved, Novel, Predicted GTPase. *Cell*. 90:121-129.

Hall, M. 2009. The WEKA Data Mining Software: An Update. *SIGKDD Explorations*. 11:10-18.

Harner, M., C. Korner, D. Walther, D. Mokranjac, J. Kaesmacher, U. Welsch, J. Griffith, M. Mann, F. Reggiori, and W. Neupert. 2011. The mitochondrial contact site complex, a determinant of mitochondrial architecture. *EMBO Journal*. 30:4356-4370.

Hessenberger, M., R.M. Zerbes, H. Rampelt, S. Kunz, A.H. Xavier, B. Purfurst, H. Lilie, N. Pfanner, M. van der Laan, and O. Daumke. 2017. Regulated membrane remodeling by Mic60 controls formation of mitochondrial crista junctions. *Nature Communications*. 8:15258.

Hoppins, S., S.R. Collins, A. Cassidy-Stone, E. Hummel, R.M. Devay, L.L. Lackner, B. Westermann, M. Schuldiner, J.S. Weissman, and J. Nunnari. 2011. A mitochondrial-focused genetic interaction map reveals a scaffold-like complex required for inner membrane organization in mitochondria. *Journal of Cell Biology*. 195:323-340.

Huang X, Fan J, Li L, Liu H, Wu R, Wu Y, Wei L, Mao H, Lal A, Xi P, Tang L, Zhang Y, Liu Y, Tan S, and C. L. 2018. Fast, long-term, super-resolution imaging with Hessian structured illumination microscopy. *Nature Biotechnology*. 36:451–459.

Huff, J. 2015. The Airyscan detector from ZEISS: confocal imaging with improved signal-to-noise ratio and super-resolution. *Nature Methods*. 12:i-ii.

Imachi, H., M.K. Nobu, N. Nakahara, Y. Morono, M. Ogawara, Y. Takaki, Y. Takano, K. Uematsu, T. Ikuta, M. Ito, Y. Matsui, M. Miyazaki, K. Murata, Y. Saito, S. Sakai, C. Song, E. Tasumi, Y. Yamanaka, T. Yamaguchi, Y. Kamagata, H. Tamaki, and K. Takai. 2020. Isolation of an archaeon at the prokaryote-eukaryote interface. *Nature*. 577:519-525.

Ishihara, N., Y. Fujita, T. Oka, and K. Mihara. 2006. Regulation of mitochondrial morphology through proteolytic cleavage of OPA1. *EMBO Journal*. 25:2966-2977.

Jakobs, S., T. Stephan, P. Ilgen, and C. Bruser. 2020. Light Microscopy of Mitochondria at the Nanoscale. *Annual Review of Biophysics.* 49:289–308.

Jakobs, S., and C.A. Wurm. 2014. Super-resolution microscopy of mitochondria. *Current Opinion in Chemical Biology*. 20:9-15.

John, G.B., Y. Shang, L. Li, C. Renken, C.A. Mannella, J.M. Selker, L. Rangell, M.J. Bennett, and J. Zha. 2005. The mitochondrial inner membrane protein mitofilin controls cristae morphology. *Molecular Biology of the Cell*. 16:1543-1554.

Klar, T., S. Jakobs, M. Dyba, A. Egner, and S. Hell. 2000. Fluorescence microscopy with diffraction resolution barrier broken by stimulated emission. *Proceedings of the National Academy of Sciences of the United States of America*. 97:8206-8210.

Kondadi, A.K., R. Anand, S. Hansch, J. Urbach, T. Zobel, D.M. Wolf, M. Segawa, M. Liesa, O.S. Shirihai, S. Weidtkamp-Peters, and A.S. Reichert. 2019. Cristae undergo cycles of fusion and fission in MICOS-dependent manner. *BioRxiv*.

Kondadi, A.K., R. Anand, S. Hansch, J. Urbach, T. Zobel, D.M. Wolf, M. Segawa, M. Liesa, O.S. Shirihai, S. Weidtkamp-Peters, and A.S. Reichert. 2020. Cristae undergo continuous cycles of membrane remodelling in a MICOS-dependent manner. *EMBO Reports*. 21:e49776.

Koutsopoulos, O.S., D. Laine, L. Osellame, D.M. Chudakov, R.G. Parton, A.E. Frazier, and M.T. Ryan. 2010. Human Miltons associate with mitochondria and induce microtubule-dependent remodeling of mitochondrial networks. *Biochimica et Biophysica Acta*. 1803:564-574.

Leung, C.W., Y. Hong, J. Hanske, E. Zhao, S. Chen, E.V. Pletneva, and B.Z. Tang. 2014. Superior fluorescent probe for detection of cardiolipin. *Analytical Chemistry*. 86:1263-1268.

Lewis, S.C., L.F. Uchiyama, and J. Nunnari. 2016. ER-mitochondria contacts couple mtDNA synthesis with mitochondrial division in human cells. *Science*. 353:aaf5549.

Loew, L.M., R.A. Tuft, W. Carrington, and F.S. Fay. 1993. Imaging in Five Dimensions: Time-Dependent Membrane Potentials in Individual Mitochondria. *Biophysical Journal*. 65:2396-2407.

Macaskill, A.F., J.E. Rinholm, A.E. Twelvetrees, I.L. Arancibia-Carcamo, J. Muir, A. Fransson, P. Aspenstrom, D. Attwell, and J.T. Kittler. 2009. Miro1 is a calcium sensor for glutamate receptor-dependent localization of mitochondria at synapses. *Neuron*. 61:541-555.

Mamikutty, N., Z.C. Thent, and F. Haji Suhaimi. 2015. Fructose-Drinking Water Induced Nonalcoholic Fatty Liver Disease and Ultrastructural Alteration of Hepatocyte Mitochondria in Male Wistar Rat. *Biomedical Research International*. 2015:895961.

Mannella, C.A., W.J. Lederer, and M.S. Jafri. 2013. The connection between inner membrane topology and mitochondrial function. *Journal of Molecular and Cellular Cardiology*. 62:51-57.

Melese, T., and P.D. Boyer. 1985. Derivatization of the Catalytic Subunits of the Chloroplast ATPase by 2-Azido-ATP and Dicyclohexylcarbodiimide. *Journal of Biological Chemistry*. 260:15398-15401.

Mitchell, P. 1961. Coupling of phosphorylation to electron and hydrogen transfer by a chemi-osmotic type of mechanism. *Nature*. 191:144-148.

Mitchell P, and M. J. 1969. Estimation of membrane potential and pH difference across the cristae membrane of rat liver mitochondria. *European Journal of Biochemistry*. 7:471–484.

Mitchell, P., and J. Moyle. 1969. Estimation of Membrane Potential and pH Difference across the Cristae Membrane of Rat Liver Mitochondria. *European Journal of Biochemistry.* 7:471-484.

Molina, A.J., J.D. Wikstrom, L. Stiles, G. Las, H. Mohamed, A. Elorza, G. Walzer, G. Twig, S. Katz, B.E. Corkey, and O.S. Shirihai. 2009. Mitochondrial networking protects beta-cells from nutrient-induced apoptosis. *Diabetes*. 58:2303-2315.

Nagashima, S., L. Tábara, L. Tilokani, V. Paupe, H. Anand, J. Pogson, R. Zunino, H. McBride, and J. Prudent. 2020. Golgi-derived PI(4)P-containing vesicles drive late steps of mitochondrial division. *Science*. 367:1366–1371.

Noji, H., R. Yasuda, M. Yoshida, and K. Kinosita Jr. 1997. Direct observation of the rotation of F1-ATPase. *Nature*. 386:299-302.

Olichon, A., L. Baricault, N. Gas, E. Guillou, A. Valette, P. Belenguer, and G. Lenaers. 2003. Loss of OPA1 perturbates the mitochondrial inner membrane structure and integrity, leading to cytochrome c release and apoptosis. *Journal of Biological Chemistry*. 278:7743-7746.

Otsuga, D., B. Keegan, E. Brisch, J. Thatcher, G. Hermann, W. Bleazard, and J. Shaw. 1998. The Dynamin-related GTPase, Dnm1p, Controls Mitochondrial Morphology in Yeast *Journal of Cell Biology*. 143:333-349.

Palade, G.E. 1953. An electron microscope study of the mitochondrial structure. *The Anatomical Record. 114: 427-452, 1952*.

Pham, T.D., P.Q. Pham, J. Li, A.G. Letai, D.C. Wallace, and P.J. Burke. 2016. Cristae remodeling causes acidification detected by integrated graphene sensor during mitochondrial outer membrane permeabilization. *Scientific Reports*. 6:35907.

Presley, A.D., K.M. Fuller, and E.A. Arriaga. 2003. MitoTracker Green labeling of mitochondrial proteins and their subsequent analysis by capillary electrophoresis with laser-induced fluorescence detection. *Journal of Chromatography B*. 793:141-150.

Rabl, R., V. Soubannier, R. Scholz, F. Vogel, N. Mendl, A. Vasiljev-Neumeyer, C. Korner, R. Jagasia, T. Keil, W. Baumeister, M. Cyrklaff, W. Neupert, and A.S. Reichert. 2009. Formation of cristae and crista junctions in mitochondria depends on antagonism between Fcj1 and Su e/g. *Journal of Cell Biology*. 185:1047-1063.

Rampelt, H., R.M. Zerbes, M. van der Laan, and N. Pfanner. 2017. Role of the mitochondrial contact site and cristae organizing system in membrane architecture and dynamics. *Biochimica et Biophysca Acta Molecular Cell Research*. 1864:737-746.

Rieger, B., W. Junge, and K.B. Busch. 2014. Lateral pH gradient between OXPHOS complex IV and F(0)F(1) ATP-synthase in folded mitochondrial membranes. *Nature Communications*. 5:3103.

Santel, A., and M. Fuller. 2000. Control of mitochondrial morphology by a human mitofusin. *Journal of Cell Science*. 114:867-874.

Saotome, M., D. Safiulina, G. Szabadkai, S. Das, A. Fransson, P. Aspenstrom, R. Rizzuto, and G. Hajnoczky. 2008. Bidirectional Ca2+-dependent control of mitochondrial dynamics by the Miro GTPase. *Proceedings of the National Academy of Sciences of the United States of America*. 105:20728-20733.

Schneider, C., W. Rasband, and K. Eliceiri. 2012. NIH Image to ImageJ: 25 years of Image Analysis. *Nature Methods*. 9:671-675.

Segawa, M., D.M. Wolf, N.W. Hultgren, D.S. Williams, A.M. van der Bliek, D.B. Shackelford, M. Liesa, and O.S. Shirihai. 2020. Quantification of cristae architecture reveals time-dependent characteristics of individual mitochondria. *Life Science Alliance*. 3.

Sivitz, W.I., and M.A. Yorek. 2010. Mitochondrial Dysfunction in Diabetes: From Molecular Mechanisms to Functional Significance and Therapeutic Opportunities. *Antioxidants & Redox Signaling*. 12.

Skulachev, V.P. 2001. Mitochondrial filaments and clusters as intracellular power-transmitting cables. *Trends in Biochemical Sciences*. 26.

Smirnova, E., L. Griparic, D. Shurland, and A.M. van der Bliek. 2001. Dynamin-related Protein Drp1 Is Required for Mitochondrial Division in Mammalian Cells. *Molecular Biology of the Cell*. 12:2245-2256.

Stephan, T., A. Roesch, D. Riedel, and S. Jakobs. 2019. Live-cell STED nanoscopy of mitochondrial cristae. *Scientific Reports*. 9:12419.

Strauss, M., G. Hofhaus, R.R. Schroder, and W. Kuhlbrandt. 2008. Dimer ribbons of ATP synthase shape the inner mitochondrial membrane. *EMBO Journal*. 27:1154-1160.

Twig, G., A. Elorza, A.J. Molina, H. Mohamed, J.D. Wikstrom, G. Walzer, L. Stiles, S.E. Haigh, S. Katz, G. Las, J. Alroy, M. Wu, B.F. Py, J. Yuan, J.T. Deeney, B.E. Corkey, and O.S. Shirihai. 2008. Fission and selective fusion govern mitochondrial segregation and elimination by autophagy. *EMBO Journal*. 27:433-446.

Vincent, A.E., Y.S. Ng, K. White, T. Davey, C. Mannella, G. Falkous, C. Feeney, A.M. Schaefer, R. McFarland, G.S. Gorman, R.W. Taylor, D.M. Turnbull, and M. Picard. 2016. The Spectrum of Mitochondrial Ultrastructural Defects in Mitochondrial Myopathy. *Scientific Reports*. 6:30610.

Vogel, F., C. Bornhovd, W. Neupert, and A.S. Reichert. 2006. Dynamic subcompartmentalization of the mitochondrial inner membrane. *Journal of Cell Biology*. 175:237-247.

von der Malsburg, K., J.M. Muller, M. Bohnert, S. Oeljeklaus, P. Kwiatkowska, T. Becker, A. Loniewska-Lwowska, S. Wiese, S. Rao, D. Milenkovic, D.P. Hutu, R.M. Zerbes, A. Schulze-Specking, H.E. Meyer, J.C. Martinou, S. Rospert, P. Rehling, C. Meisinger, M. Veenhuis, B. Warscheid, I.J. van der Klei, N. Pfanner, A. Chacinska, and M. van der Laan. 2011. Dual role of mitofilin in mitochondrial membrane organization and protein biogenesis. *Developmental Cell*. 21:694-707.

Wang C, Taki M, Sato Y, Tamura Y, Yaginuma H, Okada Y, and Y. S. 2019. A photostable fluorescent marker for the superresolution live imaging of the dynamic structure of the mitochondrial cristae. *Proceedings of the National Academy of Sciences of the United States of America*. 116:15817-15822.

Wang, X., and T.L. Schwarz. 2009. The mechanism of Ca2+ -dependent regulation of kinesin-mediated mitochondrial motility. *Cell*. 136:163-174.

Ward, M.W., A.C. Rego, B.G. Frenguelli, and D.G. Nicholls. 2000. Mitochondrial Membrane Potential and Glutamate Excitotoxicity in Cultured Cerebellar Granule Cells. *The Journal of Neuroscience*. 20:7206-7219.

Waters, L.R., F.M. Ahsan, D.M. Wolf, O. Shirihai, and M.A. Teitell. 2018. Initial B Cell Activation Induces Metabolic Reprogramming and Mitochondrial Remodeling. *iScience*. 5:99-109.

Wikstrom, J.D., S.M. Katzman, H. Mohamed, G. Twig, S.A. Graf, E. Heart, A.J. Molina, B.E. Corkey, L.M. de Vargas, N.N. Danial, S. Collins, and O.S. Shirihai. 2007. beta-Cell mitochondria exhibit membrane potential heterogeneity that can be altered by stimulatory or toxic fuel levels. *Diabetes*. 56:2569-2578.

Wilkens, V., W. Kohl, and K. Busch. 2013. Restricted diffusion of OXPHOS complexes in dynamic mitochondria delays their exchange between cristae and engenders a transitory mosaic distribution. *Journal of Cell Science*. 126:103-116.

Wolf, D.M., M. Segawa, A.K. Kondadi, R. Anand, S.T. Bailey, A.S. Reichert, A.M. van der Bliek, D.B. Shackelford, M. Liesa, and O.S. Shirihai. 2019. Individual cristae within the same mitochondrion display different membrane potentials and are functionally independent. *EMBO Journal*. 38:e101056.

Wolf, D.M., M. Segawa, S.O. Shirihai, and M. Liesa. 2020. Method for Live-Cell Super-Resolution Imaging of Mitochondrial Cristae and Quantification of Submitochondrial Membrane Potentials. *Methods in Cell Biology*. 155:545-555.

Wollweber, F., K. von der Malsburg, and M. van der Laan. 2017. Mitochondrial contact site and cristae organizing system: A central player in membrane shaping and crosstalk. *Biochimica et Biophysica Acta – Molecular Cell Research*. 1864:1481-1489.

Yan, L., Y. Qi, D. Ricketson, L. Li, K. Subramanian, J. Zhao, C. Yu, L. Wu, R. Sarsam, M. Wong, Z. Lou, Z. Rao, J. Nunnari, and J. Hu. 2020. Structural analysis of a trimeric assembly of the mitochondrial dynamin-like GTPase Mgm1. *Proceedings of the National Academy of Sciences of the United States of America*. 117:4061-4070.

Zanna, C., A. Ghelli, A.M. Porcelli, M. Karbowski, R.J. Youle, S. Schimpf, B. Wissinger, M. Pinti, A. Cossarizza, S. Vidoni, M.L. Valentino, M. Rugolo, and V. Carelli. 2008. OPA1 mutations associated with dominant optic atrophy impair oxidative phosphorylation and mitochondrial fusion. *Brain*. 131:352-367.

Zerbes, R.M., M. Bohnert, D.A. Stroud, K. von der Malsburg, A. Kram, S. Oeljeklaus, B. Warscheid, T. Becker, N. Wiedemann, M. Veenhuis, I.J. van der Klei, N. Pfanner, and M. van der Laan. 2012. Role of MINOS in mitochondrial membrane architecture: cristae morphology and outer membrane interactions differentially depend on mitofilin domains. *Journal of Molecular Biology*. 422:183-191.

Zhang, J., Z. Guan, A.N. Murphy, S.E. Wiley, G.A. Perkins, C.A. Worby, J.L. Engel, P. Heacock, O.K. Nguyen, J.H. Wang, C.R. Raetz, W. Dowhan, and J.E. Dixon. 2011. Mitochondrial phosphatase PTPMT1 is essential for cardiolipin biosynthesis. *Cell Metabolism*. 13:690-700.

Zick, M., R. Rabl, and A.S. Reichert. 2009. Cristae formation-linking ultrastructure and function of mitochondria. *Biochimica et Biophysica Acta*. 1793:5-19.

# CURRICULUM VITAE